Mixing of effluent surface jets in channel confluences

By

Ehsan Behzad

Thesis submitted to the University of Ottawa

in partial fulfillment of the requirements for the

Doctorate in Philosophy degree in Civil Engineering

Academic Advisors:

Professor Majid Mohammadian and Professor Colin D. Rennie

Department of Civil Engineering

Faculty of Engineering

University of Ottawa

Abstract

Urban development near rivers has led to the increased release of municipal and industrial wastewater into water bodies. When a less-dense discharge is introduced into a denser fluid, it gives rise to a positive buoyant jet. Further, a positive buoyant surface jet is formed when discharged near the free surface. This phenomenon is commonly observed in both natural and industrial settings, such as the release of heated cooling water and discharge of treated wastewater into water bodies. This method is the most traditional and economical method for releasing pollutants into rivers or coastal areas. Due to their limited dilution factor, usually ten or below, surface discharges tend to pose greater environmental risks compared to submerged alternatives. The hydrodynamics of a jet in crossflow is inherently complex, especially when the jet is released in areas of the river with complex structures, such as a confluence channel junction. Confluences are characterized by the convergence of two or more flows and distinguished by complex flow structure, hydraulic geometry, and sediment transport. Understanding the mixing phenomenon in such cases is crucial for accurately predicting environmental impacts. This study investigates the surface discharges of jets into confluence waterbodies through both numerical simulations and experimental methods.

Experimental studies on buoyant and non-buoyant surface discharges of jets into crossflow were carried out in this research. A new experimental setup was designed and constructed in the Civil Engineering Hydraulics Laboratory at the University of Ottawa to conduct these experiments. laser-induced fluorescence (LIF) experiments were conducted to investigate the combined effects of jet strength and nozzle location on the mixing of a positive or neutral jet issuing into a plane perpendicular to the crossflows. The trajectory and mixing within a channel junction of surface crossflow jets are investigated. The investigations revealed that a jet issued into the main channel mixes more effectively with wider dispersion compared with a jet issued in the tributary. This is due to the shear layer in the main channel, which restricts the jet in tributary to a narrower width, limiting its ability to mix effectively with ambient water.

Three-dimensional (3D) Computational Fluid Dynamics (CFD) models were developed to study mixing processes at confluences and the behavior of surface jets discharging into confluence bodies, utilizing various turbulence models. The numerical results for confluence flow were compared against experimental data from existing literature, and subsequent results for mixing of an effluent jet in a confluence flow were compared against experimental work conducted in this study.

Acknowledgements

I would like to express my deepest gratitude to my supervisors, Dr. Majid Mohammadian and Dr. Colin D. Rennie, whose guidance and support have been instrumental in the completion of this doctoral thesis. Their combined expertise and encouragement have inspired me to explore the complexities of my research with passion and determination.

To my wife, Maliheh, I owe immeasurable thanks. Her patience, understanding, and unwavering support during the challenges of pursuing a PhD have been my foundation. Her belief in my dreams and the sacrifices she made have been essential to my success.

I am profoundly thankful to my parents, Soheila and Ghafoor, for their boundless love, encouragement, and sacrifices throughout my academic journey. They consistently believed in my abilities, providing ongoing motivation and instilling values and resilience that have shaped my path.

Table of Contents

List of Figures

List of Tables

List of Abbreviations

3D	Three-Dimensional
AIZ	Allocated Impact Zone
CFD	Computational Fluid Dynamics
CCD	Charge-Coupled Device
DES	Detached Eddy Simulation
DNS	Direct Numerical Simulation
DPSS	Diode-Pumped Solid-State
EPA	Environmental Protection Agency
EVM	Eddy Viscosity Model
LES	Large Eddy Simulation
LIF	Laser-Induced Fluorescence
LRR	Launder, Reece, and Rodi
MAPE	Mean Absolute Percentage Error
OpenFOAM	Open Field Operation and Manipulation
PCG	Preconditioned Conjugate Gradient
RANS	Reynolds-Averaged Navier-Stokes
RNG	Re-Normalization Group
RSM	Reynolds Stress Model
SGGP	Single-Gene Genetic Programming
SGS	Subgrid-Scale
SST	Shear Stress Transport
VoF	Volume of fluid
NRMSE	Normalized root mean square error
RMSE	Root mean square error

List of Symbols

θ	Discharge Initial Angle [º]
$\emptyset(t)$	Instantaneous Variable [depends on the variable]
$\bar{\emptyset}$	Mean Component of An Instantaneous Variable [depends on the variable]
$\emptyset'(t)$	Fluctuating Component of An Instantaneous Variable [depends on the variable]
ϕij	Pressure-Strain Parameter []
α	Volume Fraction []
Δ	LES Filter Size []
ρ	Local Density [kg/m3]
ρ_0 or ρ_j	Effluent Density [kg/m3]
ρ_a or ρ_m	Ambient Density [kg/m3]
ε_{ij}	Turbulence Dissipation Rate Parameter [m2/s3]
ν_t	Turbulent Eddy Viscosity [m2/s]
μ	Dynamic Viscosity [N.s/m2]
μt	Turbulent Viscosity [N.s/m2]
τij	Stress Tensor []
Ωij	Transport Term by Rotation []
Πij	Transport Term by Turbulent Pressure-Strain Interactions []
δij	Kronecker Delta []
d	Nozzle Diameter [m]
s	Port Spacing [m]
uj	Jet Velocity [m/s]
um	Ambient Velocity [m/s]
Fr	Froude Number []

Fd or $F0$	Jet Densimetric Froude Number []
Q	Volume Flux [m/s]
M	Kinematic Momentum Flux [N/m2]
B	Buoyancy Flux [N/(m2.s)]
q_0	Volume Flux Per Unit Length [1/s]
m_0	Kinematic Momentum Flux Per Unit Length [N/m3]
b_0	Buoyancy Flux Per Unit Length [N/(m.s)]
g	Gravitational Acceleration [m/s2]
g_0'	Reduced Gravitational Acceleration [m/s2]
l_Q and l_M	Jet Length Scales [m]
C_0	Initial Concentration [mg/L]
C	Local Concentration [mg/L]
t	Time [s]
h	Fluid Column Height [m]
Dab	Molecular Diffusivity [m2/s]
SC	Turbulent Schmidt Number [m2/s]
$ui'uj'$	Reynolds Stress [m2/s2]
$DijT$	Turbulent Diffusion Parameter []
$Dijv$	Viscous Diffusion Parameter []
Pij	Production Rate Parameter []
Rij	Reynolds Stress [m2/s2]
$\overline{ui}$	Filtered Velocity Field [m/s]
$\overline{p}$	Filtered Pressure Field [kg/(m.s2)]
Q_0	Jet flow rate
M_0	Jet momentum flux

J_0	Jet buoyancy flux
U_r	Shear velocity
E	Roughness parameter
Y^+	Nondimensional wall distance
κ	Von Karman constant
u_i'	Fluctuating components
$\overline{u_i' u_j'}$	Time-averaged turbulent Reynolds shear stresses
S_{ij}	Local mean strain
Cs	Smagorinsky constant
σ	Standard deviation of the concentration values
C_{max}	Peak tracer concentration

1. Introduction and Objectives

1.1. Introduction

Urban expansion near river systems has led to increased discharge of municipal and industrial wastewater into aquatic environments. These effluents, which may be released as surface or submerged discharges, pose a significant risk to the environment. A comprehensive understanding of the mixing dynamics of these discharges within receiving water bodies is essential for mitigating their potentially deleterious effects on both ecosystems and human health. The interaction between the discharged effluents and ambient water is primarily governed by the density differential between the two fluids. This differential gives rise to three distinct mixing regimes: non-buoyant, negatively buoyant, and positively buoyant regimes. In scenarios where the effluent density is lower than that of the receiving water, the discharge is positively buoyant. Conversely, when the effluent density exceeds that of ambient water, it is classified as negatively buoyant. These density differences can be attributed to various factors, including temperature gradients, variations in salinity, and presence of suspended particulate matter.

In arid and semi-arid regions, desalination plants are vital for addressing the increasing demand for freshwater, driven by population growth and economic expansion. However, the desalination process also produces concentrated brine, a by-product with salinity levels approximately twice that of standard seawater [1]. The unregulated discharge of this brine into aquatic systems can significantly alter the physical, chemical, and biological parameters of receiving waters, potentially leading to environmental degradation [2].

Brine effluent disposal is often managed using extensive submarine pipelines that transport effluents to offshore locations, thereby effectively mitigating the environmental impact on coastal regions. At these distant offshore sites, brine is released as high-velocity turbulent jets through diffusers, which facilitates rapid mixing with the surrounding seawater and protects the marine ecosystem (Figure 1). These jets are typically discharged at an upward angle relative to the horizontal direction and exhibit negative buoyancy. Consequently, they are known as Inclined Negatively Buoyant Jets (INBJs) [3].

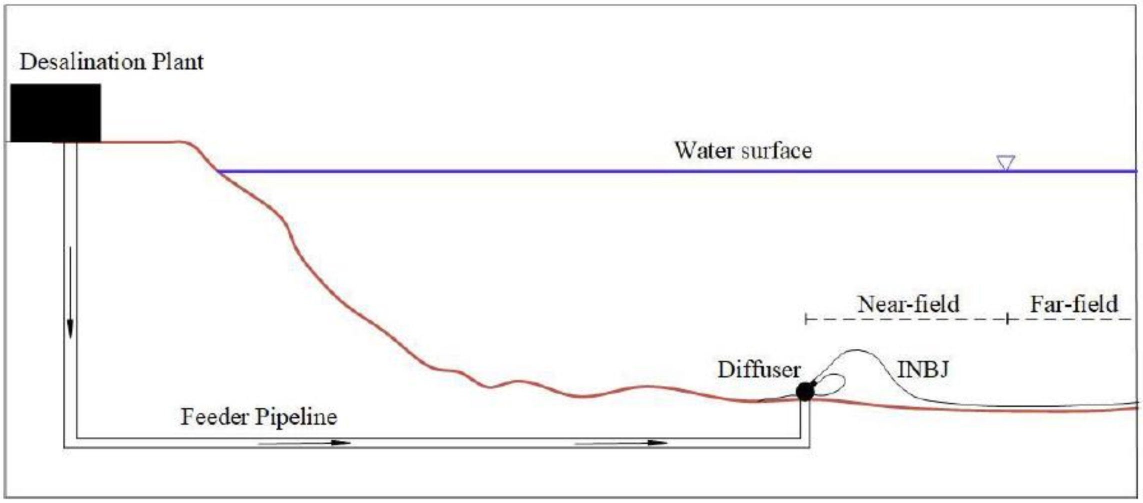

Figure 1. Typical configuration of a desalination plant outfall system [3].

INBJs, which are denser than ambient water, initially rise upon discharge, then curve downward, and ultimately descend to the seabed. This behavior is critical because the deposition of brine on the seafloor can have adverse effects on benthic ecosystems, including seagrass beds, due to the elevated salinity and potential chemical residues in the brine [4].

Another form of effluent discharge is thermal pollution, which can release substantial amounts of thermal energy into nearby water bodies, resulting in localized high-temperature zones. Such thermal discharges can have profound ecological impacts, including increased mortality rates and decreased reproductive success in certain fish species, shifts in local phytoplankton community structures, and even a reduction in biodiversity [5]. A typical example of a positively buoyant surface plume occurs when cooling water from power plant outfalls is discharged into a river or along the shoreline via an open channel (Figure 2).

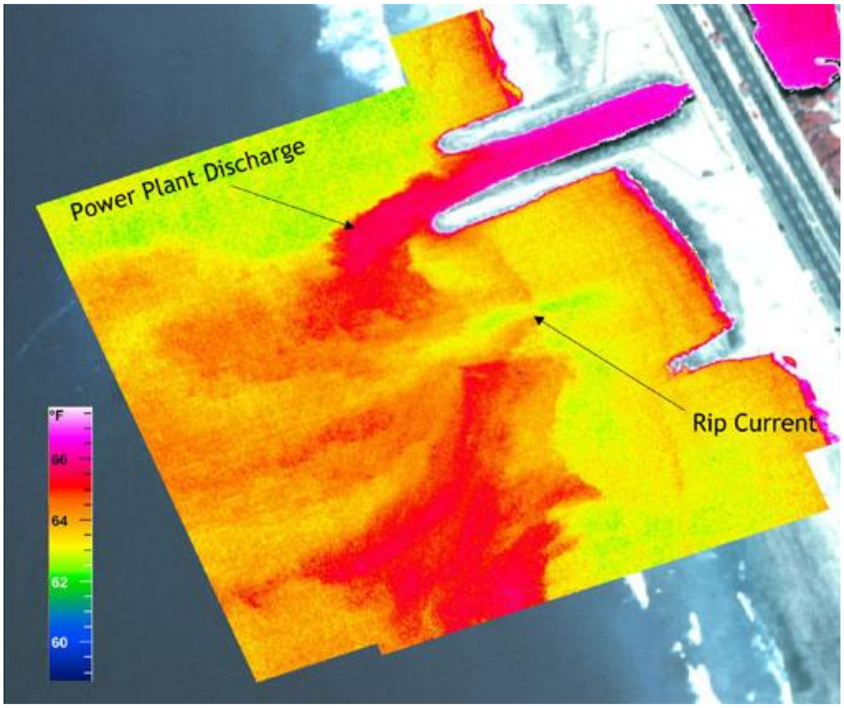

Figure 2. Warm effluent from a power plant, Encinas Power Plant, Carlsbad, CA [6].

Surface discharge represents one of the most traditional and cost-effective methods for disposing of treated industrial and domestic wastewater into rivers and coastal waters. However, the relatively low dilution rates associated with surface discharges, often less than ten [7], have led to increasing scrutiny under environmental regulations. For instance, in the United States, the National Pollutant Discharge Elimination System (NPDES) imposes stringent limitations on surface discharges, often requiring extensive pretreatment to minimize the environmental impact[8].

The hydrodynamics of a jet in crossflow are inherently complex, particularly when the jet is introduced into river regions with intricate structures, such as at a confluence channel junction. The presence of a confluence can significantly alters both the predicted and unpredicted behaviors of the jet, leading to deviations from the expected flow patterns and mixing processes. Studying jets in confluences is crucial due to the complexity of these regions, where effective mixing and dilution are essential to minimizing environmental impact. Moreover, this knowledge can guide future designs, allowing engineers to strategically position treatment plants or other facilities near these areas. By leveraging the enhanced mixing dynamics at confluences, such designs can improve discharge efficiency while mitigating ecological risks.

Open channel confluences are hydrological systems in which two or more channels converge, resulting in complex flow structures. These structures can be challenging to understand and model due to the complexity of the flow physics involved. Over the years, several researchers have attempted to gain a better understanding of the behavior of open-channel confluences using experimental [9–19], numerical methods [20–25] and field experiments [20,26–40].

Best (1987) [41] proposed a generalized model for river confluences that includes six different zones (Figure 3). These zones are characterized by different flow patterns and velocities. The first zone is the stagnation zone, where the water from the branch river meets the slower moving water of the main river, causing a build-up of water. The second zone is the deflection zone, where the flow from the branch river changes direction to align with that of the main river channel. The third zone is the separation zone, which is the area immediately after the junction close to the inner bank of the main river. The velocity in this zone is usually low and is considered to be a source of turbulence. The fourth zone was the maximum velocity zone, which occurs in the contraction or acceleration zone close to the outer bank of the main river. The fifth zone is the flow recovery zone, in which the flow begins to recover from the turbulence generated in the shear plane. The sixth and final zone is the shear plane, which occurs at the branch river entrance to the main river and is the primary source of turbulence generation due to the differences in their velocity fields.

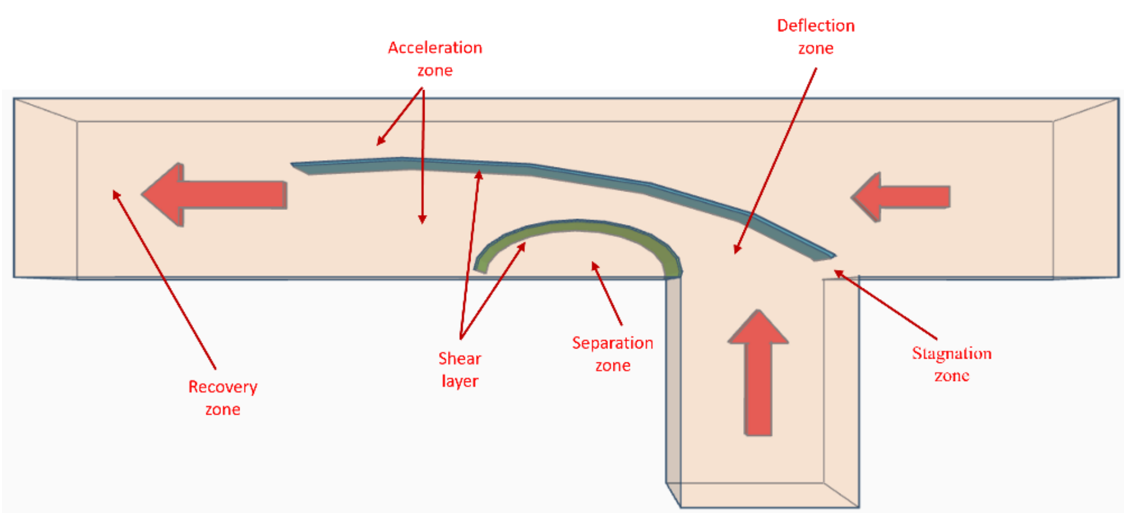

Figure 3. Flow characteristics in channel confluences (based on Best, 1987 [41])

1.2.Gaps in the Literature and Research Needs

While substantial research has been conducted on jet behavior in various crossflow conditions, several gaps remain, particularly concerning positive surface jets in confluences:

- Limited Studies on Surface Jets in Confluences: Existing studies primarily focus on submerged jets or neutral buoyancy jets in simpler crossflow scenarios. Research addressing the specific behavior of positive buoyancy surface jets in the complex flow dynamics of confluence regions remains scarce. These jets often exhibit unique trajectory and mixing characteristics that require further investigation.
- Influence of Confluence Geometry: Most studies in the literature examine flow structures in straight or mildly curved crossflows. The impact of confluence-specific geometries, such as confluence angles, junction configurations, and varying channel slopes, on jet dynamics is underexplored.
- Interaction with Tributary and Main Channel Flows: The interplay between tributary flows and the main channel in confluence areas adds another layer of complexity. Research detailing how these interactions affect jet dispersion, dilution, and trajectory, particularly for positively buoyant jets, is limited.
- High Buoyancy Effects in Realistic Flow Scenarios: While laboratory studies often simplify buoyancy conditions, real-world discharges frequently involve jets with higher buoyancy due to thermal or density differences. Investigating these effects under realistic conditions is essential to bridge the gap between laboratory findings and field applications.
- Numerical Model Validation: Numerical simulations have become an essential tool for studying jet behavior. However, there is a need for more extensive validation of numerical models against experimental data for positive surface jets in confluences.

1.3. Research Objectives, Novelty, and Contributions

As discussed in the previous section, surface discharges are a critical environmental concern. However, in some instances, surface discharges are unavoidable, thus deeper understanding of their mixing behavior is required. Most studies on jets in crossflows in the literature have focused on vertical buoyant jets. Relatively few studies have been conducted on horizontal surface jets. To better understand the mixing behavior of surface buoyant jets discharging into crossflow conditions, particularly in junction areas, it is essential to study the jet distributions within the affected zones. This represents a challenging hydrodynamic problem that, to the best of the author's knowledge, has not been investigated. Specifically, to the best of the author's knowledge, no research has investigated outfall mixing in junction areas, thus there is a significant gap in the current understanding of this topic. In the existing literature, research has concentrated on either jet in crossflow or flow structures within confluence channels as separate topics. However, there has been little to no investigation into the behavior of jets specifically in confluence areas. Moreover, development of an accurate method for estimating the mixing of surface jets in crossflows is required for improving predictive capabilities and mitigating environmental impacts.

To address this research gap, a comprehensive research program was developed to examine for the first time the mixing of effluent jets in confluence zones. New measurement techniques were utilized to yield more accurate experimental results, thereby enhancing the quality of the data available. Specifically, Laser-Induced Fluorescence (LIF) was employed to conduct experiments on jets in confluence areas. The results of these experiments were compared with those generated by Computational Fluid Dynamics (CFD) models to assess the accuracy and efficiency of these numerical models. The specific objectives of this study were to explore the following aspects of surface discharges of buoyant jets in crossflow in confluence zones:

- Enhance the understanding of surface jets in confluence areas, with a particular focus on the mixing behavior in the zones near the discharge point (near-field of the outfalls).
- Conduct experimental investigations to analyze the characteristics of flow behavior by performing concentration measurements in a controlled laboratory setting.
- Examine the influence of buoyancy effects by incorporating the necessary buoyancy terms into turbulence models using the open-source CFD software, OpenFOAM.

- Compare the results obtained from CFD modelling with both existing data in the literature and the experimental measurements conducted in this study.
- Assess the performance of various turbulence models and identify the best-performing model capable of accurately predicting the mixing behavior of surface jets.
- Determine the most effective modeling approach for handling flow dynamics in confluence areas and utilize this model to further investigate and expand upon the experimental data obtained.

The novel contributions of this study can be outlined as follows:

- **Experimental Setup Design and Construction:** Development and construction in the Hydraulics Laboratory of a specialized experimental confluence flume with a glass bottom designed to measure two-dimensional (2-D) concentration and/or velocity distributions using Laser-Induced Fluorescence (LIF) or Particle Image Velocimetry (PIV) technology. This setup facilitates more precise measurements and contributes valuable new data to the field.
- **First 2-D Concentration Distribution Measurements:** This study is the first to measure concentration distributions across horizontal sections within the mixing zone of horizontal surface jets discharging into a confluence area.
- **Pioneering CFD Modeling of Surface Jets in Confluence Regions:** This research is the first to apply Computational Fluid Dynamics (CFD) modeling to the study of the mixing behavior of surface jets discharging into confluence regions.

1.4. Scope of the Study

This study investigates the mixing behavior of positively buoyant surface jets in channel confluence regions through both experimental and numerical approaches. The research emphasizes understanding how hydrodynamic conditions in complex flow structures, such as confluence areas, influence jet trajectories, mixing patterns, and pollutant dispersion. The scope of this research includes:

1. **Experimental Analysis:**

    - Development of a specialized experimental setup for conducting Laser-Induced Fluorescence (LIF) experiments, enabling high-resolution concentration measurements in controlled flume environments.
    - Examination of jet behavior under varying discharge conditions, Froude numbers, and nozzle positions to assess mixing efficiency and trajectory deviations.

2. **Numerical Modeling:**

    - Utilization of Computational Fluid Dynamics (CFD) simulations to replicate and extend experimental findings.
    - Comparison of various turbulence models, including RANS, LES, and DES, to evaluate their performance in predicting jet mixing dynamics.
    - Application of numerical methods to explore scenarios and parameters that are challenging to replicate experimentally, such as lower jet flow rates or alternate discharge positions.

3. **Environmental Implications:**

    - Analysis of mixing efficiencies and their implications for effluent dispersion in natural water systems, emphasizing applications in urban wastewater management and environmental mitigation strategies.

1.5.Thesis Outline

This thesis encompasses both experimental and numerical investigations of surface jets in junction areas. The remainder of this thesis is organized as follows.

- **Chapter 2:** A comprehensive review of the background and literature related to surface jets, confluence flows, and related topics. This chapter provides the foundational context necessary for understanding subsequent research.
- **Chapter 3:** This chapter presents numerical results focused on the vortical structures generated within confluence channels. Specifically, this part reviews and explores confluence flow dynamics through numerical simulations conducted in an open-channel

confluence flume with an equilibrium degraded bed bathymetry and compares the outcomes with those from a flatbed scenario. This study evaluates six turbulence models—Reynolds-Averaged Navier–Stokes (RANS) (standard k–ε, realizable k–ε, k–ω SST, V2-f), Large-Eddy Simulation (LES), and Detached Eddy Simulation (DES)—using rigid lid and Volume of Fluid (VoF) methods. This paper is already published in the journal of Water.

- **Chapter 4:** This chapter details the experimental work conducted in the current study, focusing on the mixing behavior of buoyant surface jets in confluence areas. The key findings include the extraction of mean concentration distributions and jet widening from the experimental data. Understanding the influence of ambient currents and jet discharge characteristics on the performance of warm polluted outfalls is crucial for mitigating the ecological impact of effluents discharged from a diffuser in a confluence region. To address this, laser-induced fluorescence (LIF) experiments were conducted to investigate the combined effects of jet strength and nozzle location on the mixing of positive or neutral jets discharging into a plane perpendicular to the crossflows. The trajectory and mixing behavior of surface crossflow jets within a channel junction were examined. Two different nozzle discharge locations and velocities were studied to assess the three-dimensional jet trajectory and concentration distribution. The investigations revealed that a jet issued into the main channel exhibited more effective mixing and wider dispersion compared to a jet issued in the tributary. This enhanced mixing in the main channel is attributed to the presence of a shear layer, which confines the tributary jet to a narrower width, thereby limiting its ability to mix effectively with the ambient water. This chapter has been submitted to the journal Environmental Processes.
- **Chapter 5:** This chapter includes numerical investigations of the surface buoyant jets in crossflows, examining ten experimental cases numerically. This work extends the experimental investigation into areas that could not be fully explored in the laboratory owing to physical limitations. The findings from this chapter submitted to a journal, and further work from this chapter is intended for future submission.
- **Chapter 6:** A summary of the key achievements and conclusions of the research, along with recommendations for future work in this field. This chapter synthesizes the findings

from previous chapters and provides guidance for continuing investigations into surface jet mixing in confluence areas.

1.6. List of Publications

1- Behzad, E.; Mohammadian, A.; Rennie, C.D.; Yu, Q. Numerical simulation of confluence flow in a degraded bed. Water **2024**, 16, 85. https://doi.org/10.3390/w16010085. (chapter 3 of the current thesis which has been published).

2- Behzad, E.; Rennie, C.D.; Mohammadian, A.; Taherian, M. Numerical experimental investigation of positively buoyant surface jet in confluence regions. (chapter 4 of the current thesis which has been submitted to Environmental Processes).

3- Behzad, E.; Mohammadian, A.; Rennie, C.D.; Goodarzi, D. Numerical simulation of surface positive jet in confluence flow (chapter 5 of the current thesis which has been submitted to Engineering Applications of Computational Fluid Mechanics)

2. Background and Literature Review

2.1. Introduction

The increasing human population and settling near rivers have led to a significant increase in municipal and industrial wastewater discharge into rivers and streams. This trend underscores the critical importance of investigating the fate and transport of pollutants in water bodies to mitigate human health risks. Pollutants can be discharged either at the surface or through pipes at varying depths in both moving and still water [42]. Several numerical and experimental studies have been conducted to enhance the understanding of the mixing processes. This chapter provides a review of the background and literature related to the field of mixing.

2.2. Jets in Crossflow

The discharge of a steady jet into a uniform crossflow, known as a jet-in-crossflow, has a variety of industrial applications. It is frequently utilized in industrial exhaust systems and diffusers for desalination and power plants. A schematic representation of a jet in crossflow is shown in Figure 4. Jets are typically expelled from a nozzle and undergo bending due to the influence of crossflow. The crossflow forces acting on the jet boundaries cause deflection and deformation, significantly affecting the behavior [8].

The dynamics of a jet in a crossflow is inherently more complex than those of a jet in still water [42–44]. The trajectory of a jet in crossflow is influenced by the ambient water velocity (u) and the jet's initial velocity (u_o). The interaction between these velocities plays a key role in shaping the trajectory of the jet. When a turbulent jet interacts with an ambient current, the boundaries of the jet are shaped by the shear stress that arises from the velocity gradient between the jet and current [42,45]. Consequently, the jet velocity in the crossflow significantly affects its mixing behavior, dispersion patterns, and potential environmental impacts [43].

To analyze the trajectory of the jet, a Cartesian coordinate system is used, with the symmetry plane along the X-axis in the direction of the crossflow and the Z-axis along the jet flow path. The most critical parameter for describing the flow field is the velocity ratio (r), which is defined as the ratio between the jet velocity (u_j) and crossflow velocity (u_a).

$$r = u_j / u_a \qquad (1)$$

The jet trajectory can be described as the line connecting the highest velocities in each cross section or as the streamline originating from the center of the circular orifice. For warm jets, the trajectory of the local ultimate temperature is particularly interesting. Empirical formulations have been developed to match experimental observations. Pratte and Baines (1967) [46] demonstrated that the jet trajectory follows the equation

$$\frac{Z}{D} = Ar\left(\frac{x}{D.r}\right)^{b} \qquad (2)$$

where D is the orifice diameter, r is the velocity ratio ($r = u_j/u_a$), and A and b are the empirically fitted parameters. These formulations help predict the behavior of the jet under various conditions.

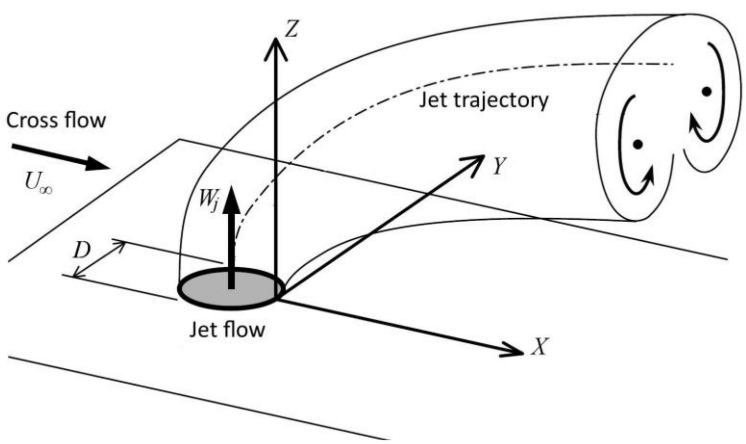

Figure 4. Generic jet in crossflow [47]

However, Eq. 2 does not fully capture the intricate details of the jet structure and mixing mechanisms, as highlighted by some studies[47–49]. Williams and Wood (1966) [50] introduced the momentum flux ratio *R*, which accounts for the effects of density and temperature variations:

$$R = \sqrt{\frac{\rho_j {u_j}^2}{\rho_m {u_m}^2}} \qquad (3)$$

where ρ_j and u_j represent the density and velocity of the jet, respectively, and ρ_m and u_m denote the density and velocity of the crossflow, respectively. When the density difference between the jet and crossflow is negligible, the expressions for the velocity ratio r and momentum flux ratio R become identical.

The parameter R is crucial for defining different flow regimes. When R is less than 2, the momentum of the jet is relatively weak, significantly preventing it from penetrating the mainstream flow. In this regime, the jet tends to attach to the downstream wall and exhibits minimal resistance to the crossflow. For R values between 2 and 10, the jet penetrates more deeply into the crossflow, reducing its contact with the downstream wall. As R approaches infinity ($R \to \infty$), the upper limit is reached, which corresponds to the behavior of a free jet. The coherent structures and flow dynamics of the jet are heavily influenced by this momentum flux ratio, making it a key factor in understanding jet-crossflow interactions.

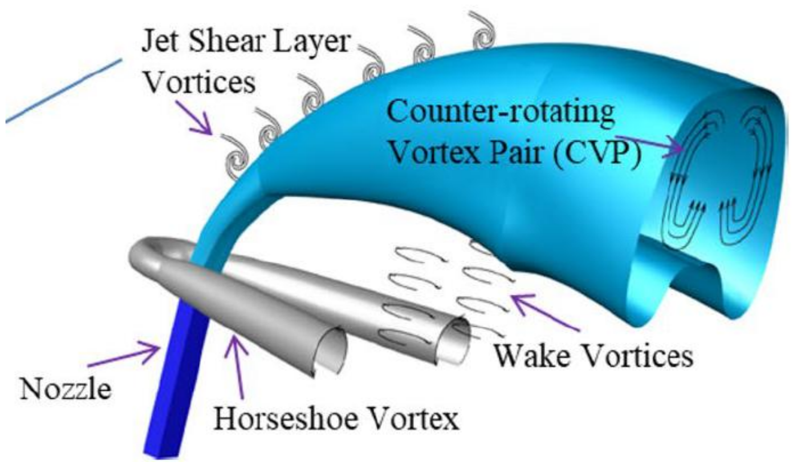

Figure 5. Main vortical structures [51]

In the discharge of jets in crossflows, four primary types of vortices can be generated (Figure 5) [8]:

1. **Counter-Rotating Vortex Pair (CVP):** is the primary vortex structure that persists along the trajectory of the jet as it moves through ambient water. This enduring vortex pair significantly enhanced mixing along the jet path by maintaining a consistent influence on the surrounding fluid [52]. The continuous rotational motion of the CVP and its interaction with the crossflow contribute to sustained turbulence and efficient dispersion of the jet momentum, thereby improving the overall mixing effectiveness within the ambient water [45].
2. **Horseshoe vortex:** The horseshoe vortex generated by a discharging jet in a crossflow can take on three different forms depending on the Reynolds number and velocity ratios of the

jet. This vortex is similar to the horseshoe vortex produced by a circular cylinder. It forms due to the adverse pressure gradient upstream of the jet.

3. **Shear-layer vortices:** The vortices arise in the boundary layer of the jet and are most prominent at the beginning of the discharge. The shear layer of the jet, which generates the Counter-Rotating Vortex Pair (CVP), causes roll-up of the leading and trailing edges of the jet. This phenomenon induces the Kelvin-Helmholtz instability, as shown in Figure 6.

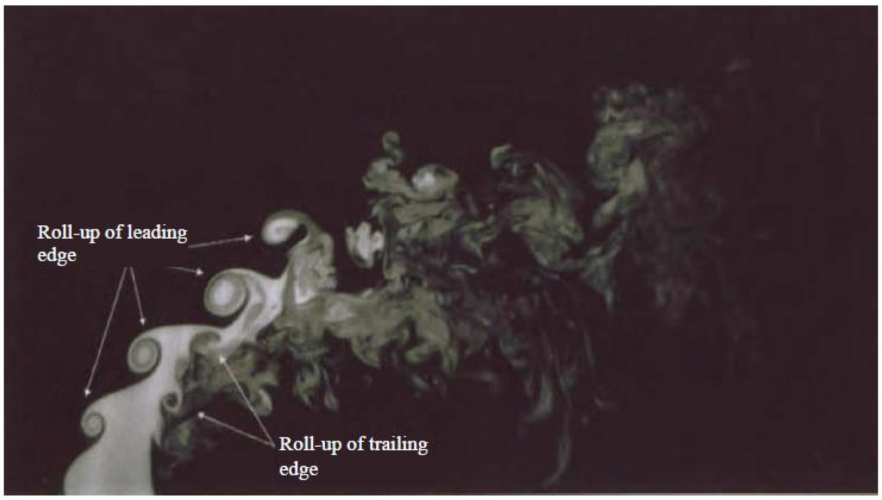

Figure 6. Shear-layer ring vortices [53]

4. **Wake Vortices:** Among the four types of vortices, wake vortices are the least understood and the most complex. Those produced by the discharge of jets in crossflows resemble vortices shed from a solid cylinder.

Wake vortices and shear-layer vortices naturally fluctuate and are usually filtered out of the velocity measurements by averaging over time. In contrast, the Counter-Rotating Vortex Pair (CVP) and horseshoe vortices exhibit both steady mean flow features and unsteady components [54].

A positively buoyant jet is formed when a less dense fluid is released into a denser fluid. Such jets are commonly observed in facilities such as multistage flash desalination plants, where elevated-temperature wastewater from the plant's cooling system is discharged [55]. The buoyancy effect causes the positively buoyant jet to exhibit a curved trajectory extending upward to the surface regime. An example for a positively buoyant jet in still ambient fluid is shown in Figure 7.

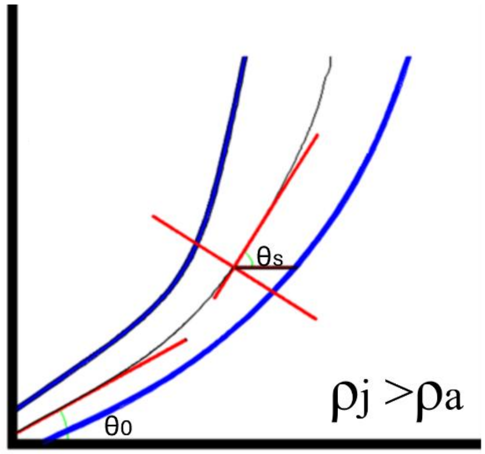

Figure 7. Schematic shape of a positive jet in quiescent ambient fluid [56]

The trajectory of the jet is established by connecting the points featuring the maximum time-averaged concentration in each cross section. The parameter θ (θ_o or θ_s) in Figure 7 represents the inclination angle, signifying the direction angle of the instantaneous velocity along the central axis in relation to the horizontal direction. Theoretically, θ reaches 90 degrees at the end of the trajectory, causing the jet to become vertically upward [57].

Buoyant surface jets, generated by discharging near the free surface, are observed in natural and industrial settings. These include the release of heated cooling water and discharge of treated wastewater into water bodies [7]. Surface discharges are environmentally sensitive method because of reduced dilution, necessitating reliable predictive planning methods, especially for small sources and heavily polluted streams [7]. Consequently, surface discharge has been extensively investigated and has become the focus of numerous studies, which will be reviewed in the next section.

2.3.Buoyant Surface Jets

Early investigations into surface thermal discharge patterns were initiated by Dunn et al. 1975, [58], followed by computational modeling using mathematical models and turbulence closure techniques [59]. In the 1960s, research focused on surface buoyant jets, prompted by concerns over the environmental impact of heated cooling water discharges from power plants. Notable contributors during this period conducted laboratory experiments and the developed integral jet models [60].

2.3.1. Surface Jets Classification

A schematic representation of the ambient water body and the discharge configuration is shown in Figure 8. The main channel is characterized by the average depth H_a, width BS, ambient velocity u_a, and density ρ_a. The outfall channel is defined by width b_0, depth h_0, and cross-sectional area $a_0=b_0h_0$. The channel has an orientation angle θ_0 relative to the direction of the main channel. The discharge is characterized by velocity U_0 and density difference $\Delta\rho_0=\rho_a-\rho_o$, where ρ_0 is the discharge density.

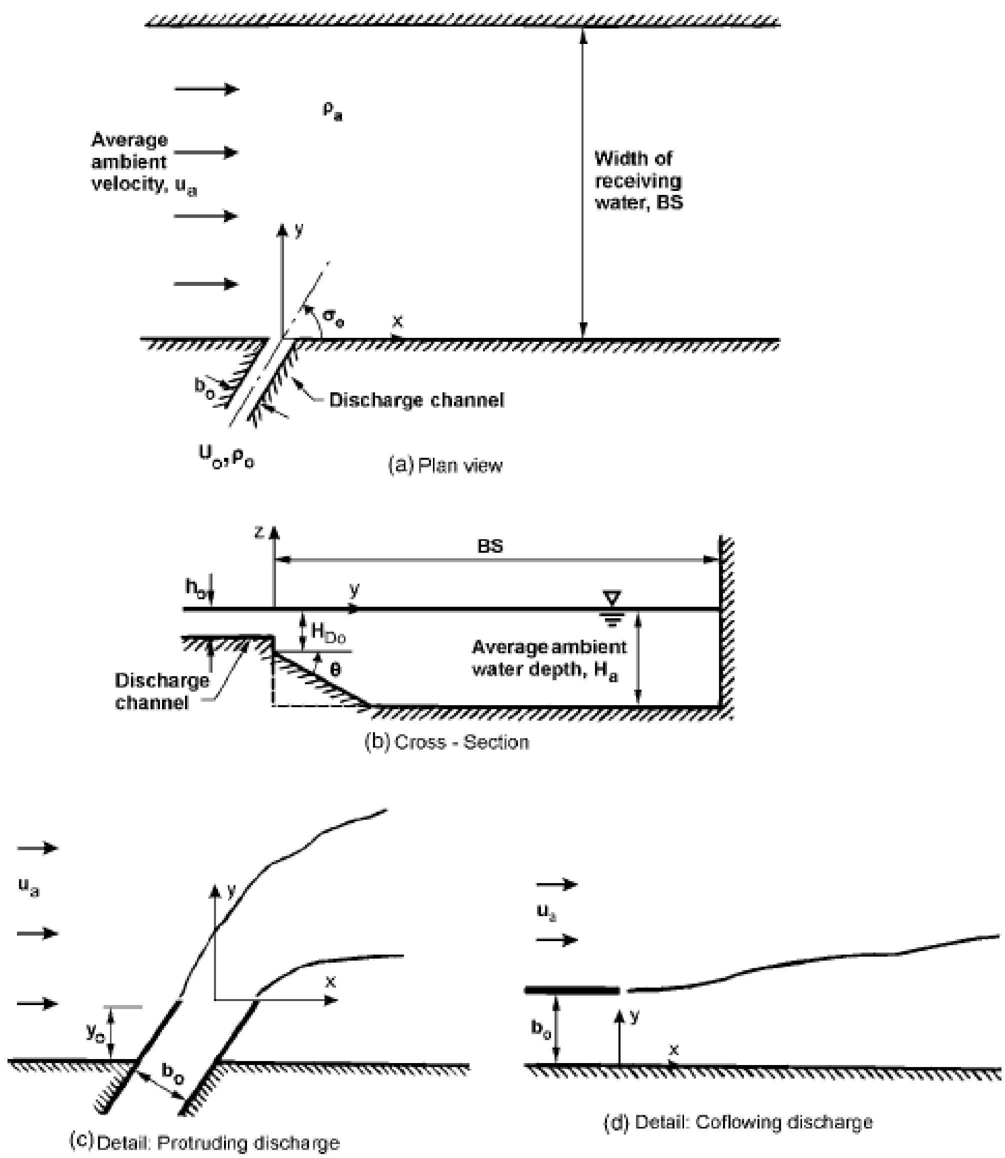

Figure 8. Schematic geometry of surface discharge in crossflow [7]

The key flow characteristics include the jet flow rate (Q_0), jet momentum flux (M_0), and jet buoyancy flux (J_0). These parameters can be calculated as follows.

Jet flow rate	$Q_0 = u_0 a_0$
Jet momentum flux	$M_0 = u_0 Q_0$
Jet buoyancy flux	$J_0 = Q_0 g'_0$
Discharge buoyant acceleration	$g'_0 = g(\Delta\rho_0/\rho_0)$

To derive the relevant length scales, the fluxes can be combined with u_a, the mean ambient crossflow velocity. These relationships are summarized as follows [61,62]:

Discharge length scale	$L_Q = Q_0/M_0^{1/2}$
Jet-to-plume length scale	$L_M = M_0^{3/4}/J_0^{1/2}$
Jet-to-crossflow length scale	$L_m = M_0^{1/2}/\overline{u_a}$
Plume-to-crossflow length scale	$L_b = J_0/\overline{u_a}^3$

- **L_M**: The jet-to-plume length scale, which measures the distance over which the flow transitions from momentum-dominated (jet-like) to buoyancy-dominated (plume-like).

- **L_m**: Jet-to-crossflow length scale, which indicates the distance over which the jet transitions from a weakly deflected region to a strongly deflected region. At this scale, the crossflow exerts a significant influence, causing the jet to begin sinking.

- **L_Q**: The discharge length scale, which determines the distance over which the entrained ambient volumetric flux becomes approximately equal to the source volumetric flux. Beyond this length, the dynamic influence of the source volumetric flux diminishes.

- **L_b**: Plume-to-crossflow (buoyancy) length scale, which specifies the vertical location at which the ambient flow begins to strongly influence the plunging plume.

These length scales are crucial for understanding the complex interactions among jets, plumes, and crossflows in various fluid dynamics scenarios. Schematic representations of these length scales are illustrated in Figure 9 by Taherian and Mohammadian (2021) [61]. These diagrams visually depict the transitions between different flow regimes, highlighting the critical distances at which the momentum, buoyancy, and crossflow forces dominate the behavior of the jet and plume.

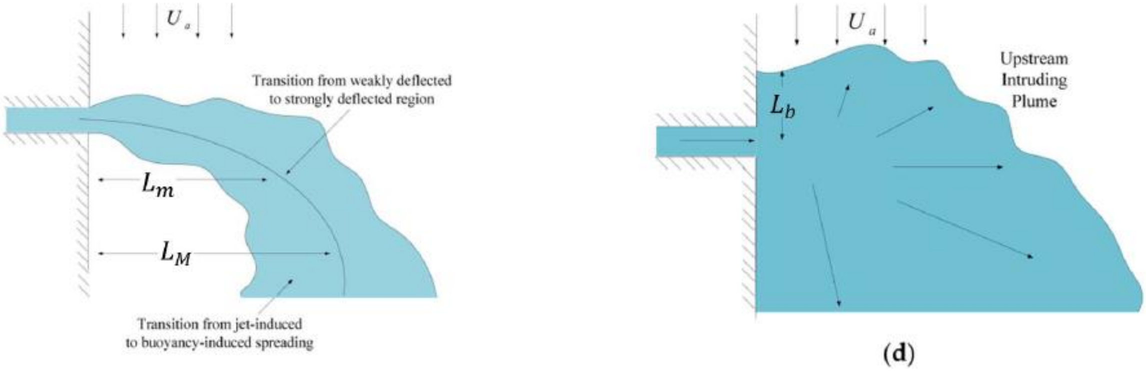

Figure 9. Length scales for different surface discharges [61]

Length-scale parameters for buoyant surface jet classifications were introduced by Jirka et al. [60], and Chu and Jirka [63] provided the initial classification for buoyant surface jets in cross-flows. A comprehensive classification system by Jones et al. [7] categorized surface jets into four main classes: free jets, shoreline-attached jets, wall jets, and upstream intruding plumes and shown in Figure 10.

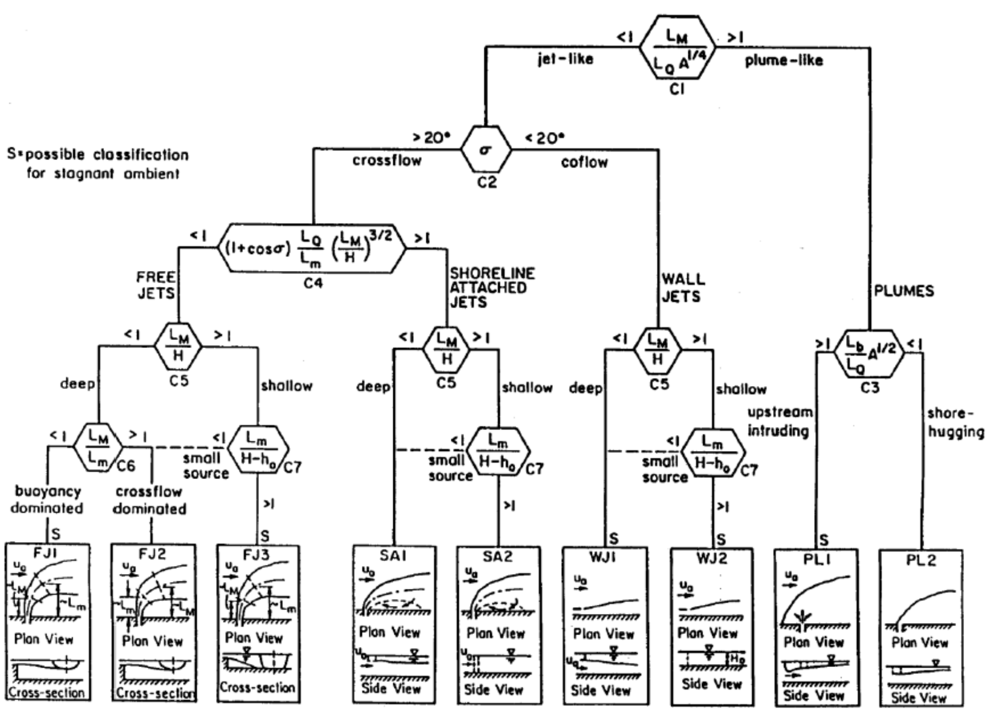

Figure 10. classification of buoyant surface discharges [7]

2.4. Confluence channel

For detailed information on confluence dynamics and related discussions, please refer to Section 3 of this thesis.

3. Numerical Simulation of Confluence Flow in a Degraded Bed[1]

3.1. Abstract

The fluid dynamics of open channel confluences are highly complex due to flow separation, secondary currents, and mixing. Although numerous studies in the past few decades have focused on the numerical simulation of confluence flow, deformed beds were rarely used. This study attempts to address this issue through numerical simulation of the flow behavior in an open channel confluence flume with an equilibrium degraded bed in OpenFOAM to compare the results with flatbed. In the present study, six turbulence models, including Reynolds-Averaged Navier-Stokes (RANS) (standard k–ε, realizable k–ε, k–ω SST, V2-f), large-eddy simulation (LES) and detached eddy simulation (DES) models were performed using rigid lid and volume of fluid (VoF) methods. The accuracy of the models was statistically analyzed by comparing with observation data, and their performance was prioritized accordingly. The results of this study demonstrated that the LES model had the best performance, with a minimum average normalized mean square error (NRMSE) of 3% under the VoF assumption and 17% under the rigid lid method. Also, the study found that in the case of a degraded bed, the recirculation zone is much shorter and even missing near the bed, leading to differences in the secondary flow. The investigation also further illuminated the intricate interplay of vortical structures within the confluence zone. Notably, the number and behavior of vortices were found to be influenced by channel geometry and size, as well as interactions between separated shear layers. Circulation within the separation zone near the inner bank differed in rotation between the degraded and flatbed cases.

Keywords: fluid mechanics, RANS, LES, DES, rigid lid, volume of fluid

[1] This section of the study has been published as: Behzad, E.; Mohammadian, A.; Rennie, C.D.; Yu, Q. Numerical Simulation of Confluence Flow in a Degraded Bed. Water 2024, 16, 85. https://doi.org/10.3390/w16010085 [64].

Article Highlights

- The study examines confluence channels with flat and degraded beds using CFD.
- LES model provides most accurate flow velocity predictions, particularly with VoF approach, whereas RANS models such as k-ω SST have limitations in complex geometries.
- Depositional bar in degraded bed scenario alters flow patterns and reduces recirculation zones.
- Vortices form due to shear layer interactions and geometry, influencing flow dynamics.
- Weaker flow contraction in degraded bed scenario affects overall flow behavior.

3.2.Introduction

Confluences are characterized by the convergence of two or more flows and distinguished by complex flow structure, hydraulic geometry, and sediment transport. Such complexity has led researchers to neglect interactions between flows, sediment, and bed morphology at confluences [65]. The conceptual model of the flow structure in a confluence was first developed by Mosley, (1976) [9] (Figure 11); his laboratory research laid the framework for determining the vital governing elements of bed geomorphology (junction angle and discharge ratio) associated with flow structure at confluences. Flow structure at such confluences is typically composed of six different flow zones including: (1) stagnation zone near the upstream junction corner, (2) deflection region, (3) separation zone below the downstream junction corner, (4) flow recovery zone at the downstream of the confluence, (5) acceleration zone as the flow enters the downstream, and (6) shear layer between the confluent flows. Several principal factors including junction angle, discharge or momentum ratio, bed level (accordant or discordant), channel geometry and any differences in density between the incoming flows can affect the confluence morphodynamics [20,66,67,21].

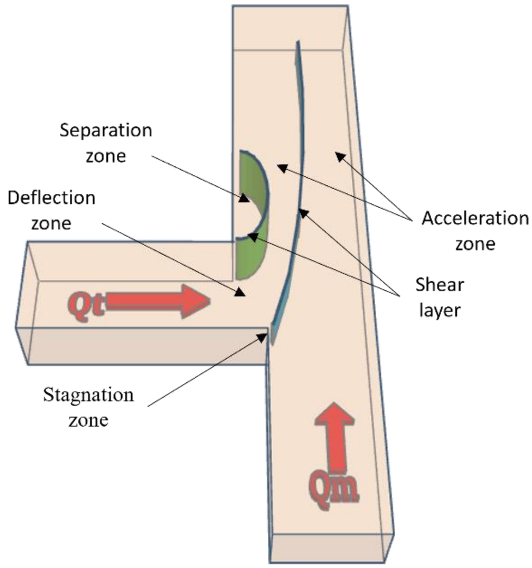

Figure 11. A schematic of junction presenting different flow zones
(Qt and Qm being the discharges of the upstream tributary and main channel, respectively)

Because these factors substantially impact bed morphology at channel junctions, a comprehensive understanding of the hydro-morphodynamics of channel confluences requires comprehending interactions between the flow and bed morphology. With the advancement of measuring devices and computer technology, it is now possible to capture precisely and describe the three-dimensional flow structure, material movement, bed evolution, and biological and environmental implications at river confluences. Consequently, recent years have seen an increase in the number of studies on river confluences and a diversification of study approaches, including laboratory experiments [9–19], field experiments [26–37,20,38–40], and numerical simulation [20–25].

However, due to the limitations of physical models (associated with scale effects) and field studies (labor- and time-consuming), as well as their dependency on the accuracy of measuring techniques, it is desirable to develop numerical simulation techniques to reduce the costs. Turbulent flows are calculated using a variety of approaches. Those approaches either calculate the turbulent flow directly (Direct Numerical Simulation, or DNS in short) or indirectly. The indirect modelling approach that has relatively low computation cost is to employ Reynolds-averaged Navier-Stokes (RANS) equations with suitable models for turbulent quantities. Other indirect approaches include large eddy simulation (LES), in which one computes time-varying flow, but sub-grid-scale motions are modelled with a turbulence model. A wall function may be used if the grid does not resolve the viscous sublayer. Alternatively, detached eddy simulation (DES) employs a RANS model near the wall's boundary and applies LES to capture the time-dependent flow away from edges. The separation of the two is characterized by the grid size. The advantage of this method is that it can significantly reduce the computational cost compared to an LES approach. Recently, several studies have utilized numerical simulations to investigate flow behavior in open-channel junctions, as will be reviewed in three subsections below. Bradbrook et al., 2000

3.2.1. RANS Simulations

Bradbrook et al., (2000) [24] simulated confluence flow patterns and the results were assessed qualitatively. A variety of parameters such as momentum flux ratio, cross-sectional area and the density differences between incoming flows were studied to find out their effects on thermal mixing at a small stream confluence. It was shown that the combination of the three parameters affect the rates and patterns of thermal mixing. Bradbrook et al. used renormalization group-based (RNG) and standard k-ε turbulence models to specify velocity field, secondary currents, and time-averaged pressure in channel confluences. Simulations of idealized laboratory-style channels demonstrated that a symmetrical confluence produced two counter-rotating secondary flows on either side of the shear layer; however, in the case of an asymmetrical junction, there was only one cell on the side of the curved tributary.

Huang et al., (2002) [68] used the experimental data from Shumate, (1998) [69] and set up a 3D numerical model with two different flow conditions for a channel junction with a 90° angle to study open-channel confluence flow. RANS equations with k-ω turbulence model were the governing equations under the assumptions of incompressible and steady-state flow. The 3D model was demonstrated to successfully reproduce hydrodynamic characteristics of the junction flow. The separation zone was situated along the left bank of the main channel immediately following the junction and was smaller, closer to the channel bed than near the water surface. Also, as the junction angle increased, the separation zone size and strength grew larger.

Shakibainia et al., (2010) [70] used SSIM2.0 for a comprehensive 3D numerical study of secondary circulation, flow in the separation zone, velocity field, and water level in different flow conditions with varying discharge ratios, junction angles, and Froude numbers. It was concluded that flow structure at channel confluences is greatly impacted by the secondary flow. The secondary flows emerged in roughly three counter-rotating helical cells across the section immediately following the junction. The first helical cell formed in the separation zone, and because silt is deposited here, this type of cell may disappear in natural rivers. Due to the deflection of the tributary flow in the direction of the main channel, the second helical cell developed. These cells are thought to be the strongest in the confluence and gradually weaken downstream of the main channel. Due to the interaction of the second cell and the flow of the main channel, the third helical cell appeared within the main channel flow with rotation counter to that of the second cell (see Figure 7 in Shakibania et al., 2010).

Similarly, Song et al., (2012) [71] performed 3D simulations of secondary flow in confluent and curved channels. The equations of depth-averaged shallow water together with dispersion stresses were solved by the SU/PG scheme. They used Shumate, (1998) [69] experimental data to validate the proposed model. The computed values of the depth-averaged velocity and the water surface profile over the channel revealed good comparison with laboratory data, which indicated that secondary velocity profiles were appropriately preserved. They demonstrated that two counter-rotating cells are produced downstream of the junction, one from the main river and the other from the branch river. Due to the fluid's viscosity, they rotate against each other and eventually dissipate as they move downstream. Shaheed et al.

Shaheed et al. (2019) [72] conducted a 3D numerical simulation model in an open-source software, "OpenFOAM," to simulate secondary currents in open-channel confluences. The behavior of these currents was simulated by using the finite volume method (FVM). They employed standard "k–ε" and "realizable k–ε" turbulence models, and their results indicated that the "realizable k–ε" model had better performance.

Tang et al., (2018) [73] developed another 3-D numerical model based on the RANS and Reynolds Stress Turbulence model to model flow patterns and contaminant transport with different bed morphologies. In their study, the effects of bed morphology on the hydrodynamics and the transport of contaminants on degraded beds at 90-degree channel confluences were investigated and the results were validated by experimental data. The results show that the shear layer and two counter-rotating helical cells controlled the distribution of contaminant, which are affected by the discharge ratio and the bed morphology.

Penna et al., (2018) [74] simulated ten confluence angles ranging from 45 to 90 degrees to examine the effects of confluence angle on flow structure. The Reynolds averaged Navier–Stokes (RANS) equations in three dimensions were solved using a computational method incorporating a k-ε turbulence closure model. The results suggested that an increase in the confluence angle produced a broader and longer retardation zone at the upstream junction and separation zone. As the angle of confluence increases, so does the flow deflection at the entrance of the tributary to the main channel. However, the confluence angle does not necessarily increase the more significant streamwise velocity.

3.2.2. LES Simulations

Schindfessel et al., (2017) [75] investigated the effect of various cross-sectional formations on the separation zone in a sharped-edge open channel confluence. Four distinct cross-sectional shapes were analyzed using a large-eddy simulation (LES) model. There was a considerable variance in the separation zone dimensions for non-rectangular geometries due to lateral currents that may diminish the local momentum deficit.

Le et al. (2019) employed LES to inspect the hydrodynamics of a natural confluence zone in the Mississippi River. Data from remote sensing (light detection and ranging; LiDAR) and field measurements were used to construct the digital elevation model. The LES results were used to gain more insight on the river flow dynamics, and to illustrate the long-range impacts of hydraulic structures on the downstream flow. This study demonstrated the feasibility of high-resolution LES for large-scale rivers by considering the detailed bathymetry and submerged hydraulic structures [76].

Ramos, Schindfessel, Pêgo, & Mulder, (2019) [77] used the experimental data collected by Yuan et al., (2016) [78] to develop a numerical model in OpenFOAM. In this study, flow ratio and downstream Froude number of two geometries were compared with experimental results by Yuan (2016) in a flume with a wider downstream than the upstream main and tributary channels. The focus of this study was downstream of the channel junction, and the LES results were used to examine the downstream channel width influence on turbulent flow features. Extension of the downstream channel turns out to decrease the backwater effects, the flow contraction, and the associated water surface depression. Furthermore, the three-dimensionality of the separation zone in the mean flow is enhanced due to complex flow patterns, resulting in a reduced width and length of the recirculation zone in the lowest third of the water column.

Turbulence flow behavior through a rectangular confluence channel was also investigated by Herrera-Granados (2021) and laboratory records were compared with the simulation results of LES and RANS models. The model output was in good agreement with time-average factors, but was not sufficient for the proper estimation of the turbulence quantities [79].

Duguay et al. (2022) used an LES model in OpenFOAM and resolved three categories of large-scale turbulent structures namely (1) vertically oriented (Kelvin–Helmholtz) vortices; (2) secondary flow helical cells and (3) smaller, strongly coherent streamwise- oriented vortices. Intricate interactions among divided flow over the scour hole's avalanche face, upwelling tributary flow as well as downwelling main channel flow were the main causes for the mixing at this asymmetric mesoscale fluvial confluence. To create a stronger mixing, both vertically oriented and streamwise- oriented vortices were firmly coupled. It is worthy to note that similar interactions were predicted via collective analysis of instant eddy-resolved modelling and aerial studies of turbulent mixing of natural turbidity gradients within the mixing interface [80].

3.2.3. DES Simulations

Constantinescu et al., (2011) [37] employed an eddy-resolving DES numerical model at an asymmetrical river junction with a concordant bed to model the mean flow and large-scale turbulence structure. The simulation targeted a confluence with a momentum ratio between the two incoming streams close to one. The results of the simulation implied that the quasi-two-dimensional eddies were dominant in the mixing interface.

Horna-Munoz et al., (2020) [23] studied the effects of density differences between incoming flows at a small, concordant bed in a natural river confluence. The simulation was carried out using a DES model. The predicted flow patterns demonstrated that secondary flow increased with increasing distance from the confluence junction.

Cheng & Constantinescu, (2020) [21] used the DES model to investigate the effects of stratification caused by density variations between two incoming flows using a confluence in a medium-sized stream and a highly discordant bed.

Jiang et al., (2022) [25] investigated flow hydrodynamics and mixing at the asymmetric confluence of the Yangtze River and the Poyang Lake channel using eddy-resolving numerical approaches. The result revealed that the flow hydrodynamics and mixing processes at the large ($W/D > 50$)

confluence shared many similarities with those typically observed at small natural confluences with a concordant bed, as well as some significant differences.

In order to numerically model the hydrodynamics of river confluences, the turbulence closure and the water surface treatment should be chosen carefully. Whereas numerous studies in the past few decades have focused on the simulation of confluences (Table 1), to the best of authors' knowledge, no deformed beds have been examined by comparison of simulations performed using a wide range of different turbulence models namely, RANS (standard k–ε, realizable k–ε, k–ω SST, V2-f), LES, and DES with two free surface methods (rigid lid and VOF).

Table 1. Summary of Some Previous Numerical Confluence Studies, Compared with the Current Study

Research(s)	**Model dimensions**	**Governing equations**	**Model domain**
Bradbrook et al., (2000) [24]	3-D	RANS	Flatbed
Huang et al., (2002) [68]	3-D	RANS	Flatbed
Stockstill, (2007) [81]	2-D		Flatbed
Shakibainia et al., (2010) [70]	3-D	RANS	Flatbed
Constantinescu et al., (2011) [37]	3-D	DES	Deformed bed
Song et al., (2012) [71]	3-D	RANS	Flatbed
Sukhodolov et al., (2017) [20]	3-D	RANS	Deformed bed
Schindfessel et al., (2017) [75]	3-D	LES	Flatbed
Tang et al., (2018)[73]	3-D	RANS	Deformed bed
Cheng & Constantinescu, (2018) [22]	3-D	DES	Deformed bed
Shaheed et al., (2019)[72]	3-D	RANS	Flatbed
Le et al., (2019) [76]	3-D	LES	Deformed bed
Ramos, Schindfessel, Pêgo, & De Mulder, (2019a) [82]	3-D	LES	Flatbed
Ramos, Schindfessel, Pêgo, & De Mulder, (2019b) [83]	3-D	LES	Flatbed
Jin et al., (2020) [84]	3-D	LES	Deformed bed
Cheng & Constantinescu, (2020)[21]	3-D	DES	Deformed bed
Horna-Munoz et al., (2020) [23]	3-D	DES	Deformed bed
Ramos, Schindfessel, Pêgo, & Mulder, (2019) [77]	3-D	LES, RANS	Flatbed
Duguay et al., (2022) [80]	3-D	LES	Deformed bed
Yan et al., (2022) [85]	2-D		Deformed bed
Jiang et al., (2022) [25]	3-D	DES	Deformed bed
This Study	3-D	LES, DES, RANS	Deformed bed

Hence, the main objective of this study is to implement these simulation techniques to model the flow field of a confluence with a degraded bed and determine the accuracy of the results to investigate the effect of bed morphology on secondary currents. To achieve this goal, first a degraded bed case studied experimentally by Yu et al., (2020) [16] was simulated to validate the numerical models. Then, the most accurate simulation was selected, and the degraded bed was replaced by flatbed to investigate the effect of differences in bed morphology on confluence hydrodynamics. Specifically, the impacts on flow deflections, separation zone, and secondary flow.

3.3.Numerical Methodology and Model verification

3.3.1. Numerical framework

OpenFOAM version 6.0, an open-source computational fluid dynamics (CFD) application, was utilized to conduct the numerical simulations in the present investigation. This toolkit provides a flexible and configurable framework for solving the governing equations for a viscous, incompressible flow. RANS, LES, and DES were used in this study to model the turbulent nature of these flows. OpenFOAM's finite volume approach is founded on a structured mesh with non-uniform distribution. Each control volume's dynamic attributes are defined by its centroid. The mesh supports an unlimited number of control volume points per face. In the numerical analysis, divergence is calculated using the Van Leer method, Laplacian terms are calculated using a corrected Gauss linear scheme, and interpolation is performed using a linear approach. This analysis uses an adjustable time increment, which means that each time step is determined depending on the previous time step in order to maximise accuracy; nevertheless, this method increases computing cost and time.

To solve the governing equations, the 'interFoam' and 'pimpleFoam' solvers of OpenFOAM were used to compare a combination of the finite volume method with either the volume of fluid (VOF) or the rigid lid method for free surface simulations. InterFoam can solve problems with dynamic mesh. In this solver, the pressure correction algorithm PIMPLE (which constructs a nonlinear set of equations and solves them using an iterative approach) was used to track the fluid flow, while the VOF method was utilised to track the free surface. PISO (pressure implicit with splitting of operator) and SIMPLE (semi-implicit method for pressure-linked equations) are combined to form the PIMPLE algorithm. The PISO and PIMPLE methods are suited for transient situations, while the SIMPLE approach is used for steady-state problems. They are, however, all iterative problem solvers. First order Euler scheme was used to discretize the temporal term while the Gauss linear method was employed for the gradient term. Corrected Gauss linear method was applied for the Laplacian. In addition, a Gauss Van Leer plus Gauss linear scheme was used to define the divergence terms, and a linear scheme was used to discretize the interpolation term. Every individual variable was assigned certain tolerance levels. As a result, the desired convergence was anticipated to take place during the iteration. The level of accuracy was defined as 10^{-5} for the fraction of liquid (α) and 10^{-8} for pressure and velocity in the Gauss–Seidel method for solving the resulting linear system of equations.

3.3.2. Hydraulic conditions

The experimental case used for validating the numerical approaches was previously described by[16]. This work examined confluence morphodynamics as well as deposition patterns of contaminated sediments. The dimensions of the flume were 40 cm (height) with different widths for the upstream (30 cm) and downstream (40cm) channels (Figure 12). Two pumps with same fixed flow rate (30 L/s) were deployed. The flow discharge in each channel was measured by ultrasonic flowmeters and could be altered using valves. A weir gate was installed at the downstream end of the flume to adjust the flow depth throughout the flume. An equilibrium degraded channel bed was established for the given flow regime, and then the bed was fixed to enable flow velocimetry and subsequent contaminated sediment feeding experiments. For further investigation through numerical simulations, the equilibrium degraded bed was initially transformed into a flatbed, and the outcomes of this alteration were thoroughly examined. The implications of this alteration are discussed in subsequent parts of this paper. In the present paper, the test scenario of a 90° channel confluence with a discharge ratio of R_Q=1.5 was utilized where $R_Q=Q_t/Q_m$ with Qt and Qm being the discharges of the upstream tributary channel and main of the open channel, respectively. Consequently, the discharge ratio was identical for all cases and shared the same Froude and Reynolds (Re) numbers, as shown in Table 2.

Table 2. Summary of the Hydraulic and Geometric Data [16]

Variable	Symbol (unit)	Value
Confluence junction angle	α (-)	90°
Discharge ratio	R_Q^*(-)	3:2
Tributary discharge	Q_t (L/s)	9
Main channel upstream discharge	Q_m (L/s)	6
Main channel downstream discharge (Total discharge)	Q_d (L/s)	15
Water depth	D (m)	0.16
Reynolds number	Re (-)	0.145×10^5
Froude number	Fr (-)	0.15

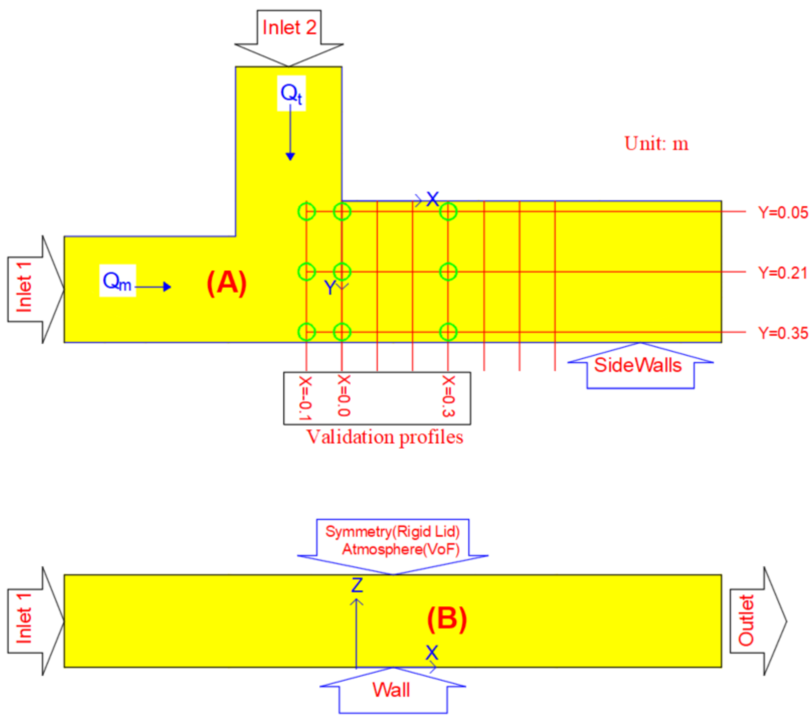

Figure 12. Measured sections, validation profiles for the simulation area and boundary conditions of the Flume A) plan view B) side view. Q_t is the discharge of tributary channel while Q_m is the discharge of main channel. Green circles mark the profiles that are used to compare the modeled and measured data (see more details in Section 3.1)

3.3.3. Mesh Generation

In this study, snappyHexMesh was used to generate the mesh, which is shown in Figure 3. The size of the numerical domain is the same as the physical field of the experiment [16]. The grid size gradually increases from each boundary since a smooth grid transition is essential to make the numerical calculation stable (Figure 13).

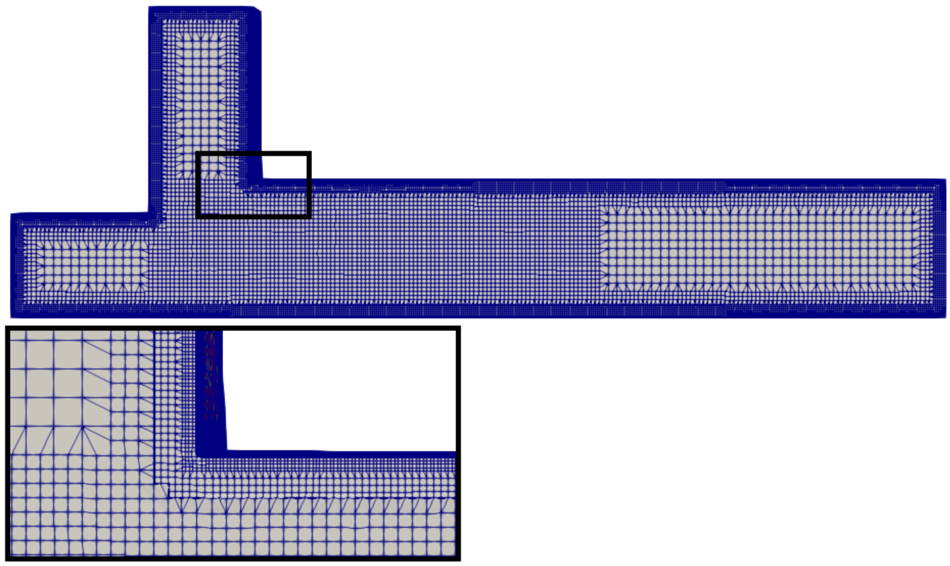

Figure 13. Mesh grids of the domain in OpenFOAM platform, on scale of 1 to 10 (for RANS turbulence models) in order to visualize the distribution of the mesh grids.

The geometry of the channel was created using Salome platform. A total of 2000 points were defined to create the degraded bed as opposed to the flatbeds that require a drastically lower number of points (i.e., 8 points). A Salome-generated bed surface map in this model is demonstrated in Figure 14.

3.3.4. Boundary Conditions

To achieve accurate simulation, different boundary conditions were employed as illustrated in Figure 12. Hydraulically standard wall functions were employed which includes four different boundaries: the two inlets and one outlet of the channel, the walls (including side walls and bottom), and the surface of the flow (symmetry for rigid lid and atmosphere for VoF). Water discharge was specified at the inlets. Zero gradient condition was considered at the outlet.

3.3.5. Wall Function Boundaries

Turbulence and velocity parameters are required in the cell closest to the wall because there is typically insufficient cell spacing near solid borders to resolve the laminar sublayer. The 'universal' law of the wall, which is based on shear velocity, is usually utilized. The fundamental presumptions of this law rely on the existence of a local turbulence equilibrium, which is unstable in the presence of flow separation. Consequently, the non-equilibrium version of the law of the wall [86] may be applied, which uses the square root of the turbulent kinetic energy as the characteristic velocity scale [87].

The 'universal' law is as follows:

$$\frac{U_r}{U_\tau} = \frac{\ln\,(E\Upsilon^+)}{\kappa} \tag{4}$$

With $U_\tau = \sqrt{\tau/\rho}$ and $\Upsilon^+ = \frac{U_\tau \Upsilon}{\mu}$

where U_r is the velocity parallel to the wall, U_τ is the shear velocity, τ is the bed shear stress, E is the roughness parameter, Υ^+ is the nondimensional wall distance, Υ is the normal distance to the wall, μ is the fluid kinematic viscosity, and κ is the von Karman constant (0.4). [86] can be used to connect the shear velocity to the local kinetic energy under the assumption that there is a local equilibrium of turbulence;

$$k = \frac{U_\tau^2}{\sqrt{c'_\mu}} \tag{5}$$

The boundary condition for ε is given by:

$$\varepsilon = (c'_\mu)^{3/4} \frac{k^{3/2}}{\kappa \Upsilon} \tag{6}$$

Because the assumption of local equilibrium (Equation (5)) does not hold in the presence of separation, $\sqrt{k}$ is employed in the non-equilibrium wall function as shown below by Shaheed et al. (2021) [88];

$$\frac{U_r \sqrt{k}}{U_\tau^2} = \frac{\ln\,(0.25 c'_\mu E \sqrt{k} \Upsilon}{0.25 c'_\mu \kappa} \tag{7}$$

where k is taken from the transport equation.

3.3.6. Free surface

Due to surface depression and elevation, which are characteristics of confluence flow dynamics [29,89], the free surface in the model must be simulated. Because identifying the exact contours of the free surface elevation is challenging, the assumption of a 'rigid lid' has been commonly employed in prior publications, which viewed the surface as a plane. Regarding the symmetry plane, all surface normal derivatives are set to zero. If the surface is not fixed, a change in water depth may occur, reflected by the surface pressure, which is not set to zero. Therefore, a pressure greater than zero signifies super-elevation, and a pressure less than zero represents surface depression. This means that the pressure gradient term in the momentum equations considers the variance in the position of the water surface. In contrast, it is not considered in the mass continuity equation, which could lead to predictions of maximum velocity in areas of super-elevation [89] and the opposite in areas of surface depression. Another strategy is based on free-surface capturing (e.g., the volume of fluid method), which simulates the location of the free surface. Free-surface capturing methods are typically more accurate than rigid-lid methods [88].

3.3.7. Bed morphology

Figure 14 demonstrates the degraded bed morphology with the bed area possessing a wide range of elevation with zones of erosion and deposition. From the downstream corner to the outer bank, a massive, curving scour hole developed. Intriguingly, based on observations made during the development of the bed, the curving scour hole was initially comprised of two independent scour holes that progressively joined in the middle of the channel. One of these two scour holes was round and placed at the downstream corner of the junction (the solid red rectangle); we will refer to it as the "corner scour hole." The scour hole that was roughly centred in the channel (the solid red circle) will be referred to as the "midchannel scour hole." Between the upstream and downstream bars (the red dashed circle) a second, shallower scour hole formed; it will be referred to as the "downstream scour hole". In addition, a conical bar formed near the downstream junction but was not connected to it (the solid cyan circle). It will henceforth be referred to as the "upstream bar." A bar in the shape of a fan was created at the flow recovery zone (the cyan dashed circle), which will henceforth be referred to as the "downstream bar."[16].

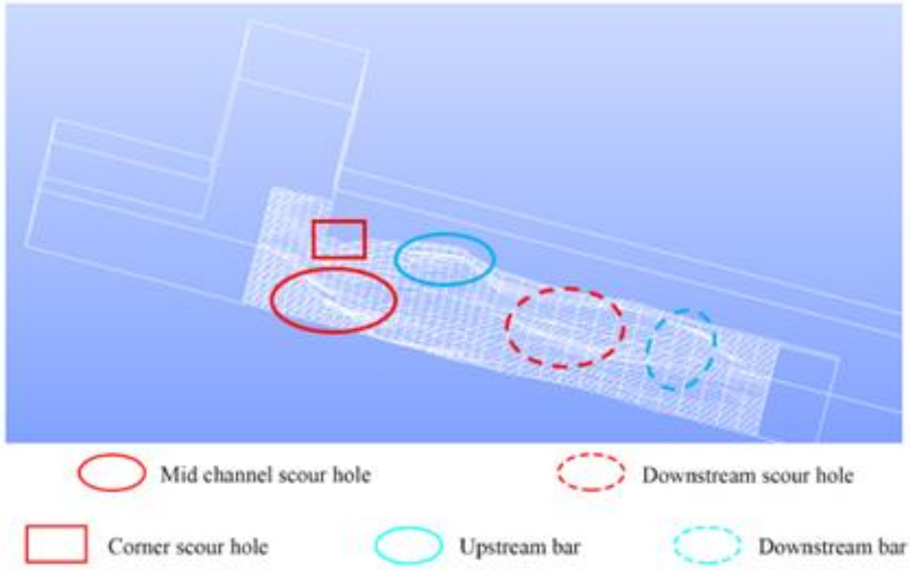

Figure 14. Contour map of equilibrium bed morphology in Salome platform. The red solid circle, red dashed circle, red solid rectangle, cyan solid circle, and cyan dashed circle indicate the mid-channel scour hole, downstream scour hole, corner scour hole, upstream bar, and downstream bar, respectively.

3.4. Model verification

3.4.1. Determination of solution

The Free Surface Model is used in open channel flow, while the Rigid Lid is used in closed channel flow. In the Free Surface Model, both air and water flows are considered in the simulation, which allows for a deformed interface, while in the Rigid-Lid Model, only the water flow is considered. InterFoam solver is used in this study, which is usually utilized for incompressible and turbulent flows in the cases of open channels (also referred to as the Free Surface Model). The free water surface was simulated using the volume of fluid (VOF) method. Also, pimpleFoam solver is used and the numerical treatment was done by means of a flat rigid lid, in which the free surface was treated as a flat, horizontal, and frictionless rigid lid at the top boundary. For discussion on the rigid-lid approach in other flow cases, see Constantinescu et al., (2012) [90].

3.4.2. Governing Equations

3.4.2.1. Reynolds Averaged Navier-Stokes (RANS) Equations

Fluid-related problems may be simulated using Reynolds averaged Navier-Stokes (RANS) equations which take the following form for the case of incompressible flow:

$$\frac{\partial \bar{u}_i}{\partial t} + \bar{u}_j \frac{\partial \bar{u}_i}{\partial x_j} = -\frac{1}{\rho}\frac{\partial \bar{p}}{\partial x_i} + \frac{\partial}{\partial x_j}\left[\vartheta\left(\frac{\partial \bar{u}_i}{\partial x_j} + \frac{\partial \bar{u}_j}{\partial x_i}\right)\right] - \frac{\partial}{\partial x_j}\overline{(u_i' u_j')} + g_i \tag{8}$$

And continuity equation:

$$\frac{\partial \bar{u}_i}{\partial x_i} = 0 \tag{9}$$

where ρ = density of the fluid; p = pressure; u_i= mean velocity in the i-direction,i=x, y, z, which refer to the streamwise, cross-stream, and vertical directions, respectively; u_i' represents the corresponding fluctuating components; t is time; υ is kinematic viscosity of the fluid, $\overline{u_i' u_j'}$ are the time-averaged turbulent Reynolds shear stresses ,and g is gravitational acceleration. The flow properties have been disintegrated into their mean and fluctuating components, and integrated over time (i.e., time-averaged). Dependent variables are a function of both space coordinates and time. For general 3D turbulent flows, there are four equations including the continuity equation. In theory, these would be enough equations to solve all three velocity components and the pressure, but there are six more unknowns: the Reynolds stresses, $u_i' u_j'$ to represent turbulent effects. So, the Reynolds stresses must be modeled to complete the equations.

Several models have been developed to resolve the distribution of eddy viscosity over the flow field. Eddy viscosity is typically used to model the turbulent effects lost in averaging in a computational fluid dynamic (CFD) simulation. The model addresses the dissipation of energy which was neglected due to the turbulence. Turbulence models allow the calculation of the mean flow prior to calculating the time-dependent flow field for the different levels of complexity of flows and computational cost. During the past four decades, two-equation models (e.g. k-epsilon and k-omega) have served as the foundation for modelling eddy viscosity in RANS [91]. Two-equation turbulence models enable both turbulent length and time scales to be determined based on Boussinesq's assumption (i.e., the turbulence stress is modelled as a function of the velocity gradients and the eddy viscosity).

3.4.2.2. Large Eddy Simulation (LES) models

In these models, eddies are categorized by their size based on the local grid spacing. Large eddies are computed directly by solving the Navier-Stokes (NS) equations, while small eddies are calculated with a sub-grid model based on the Boussinesq theory. The spatial filter is employed to disintegrate velocities into two parts: the resolved parts ($\widetilde{U}$, which captures eddies larger than the filter width) and residual parts (u', fluctuation velocity of small eddies modeled in sub-grid) [92], and u_i= mean velocity in the i-direction (i=x,y,z). The filter width is related to the cell volume. Particularly, the filter width needs to be defined in a way that captures the smallest eddies of interest.

$$u(x,t) = \widetilde{U}(x,t) + u'(x,t) = \bar{u}_i + u'_i \tag{10}$$

u'_i: Fluctuating velocity in tensor notation

$$\bar{u}_i(x,t) = \iiint G(x-\xi;\Delta)u_i(\zeta,t)d^3\zeta \tag{11}$$

where spatial filter (G) is defined as follows:

$$(x-\zeta;\Delta) = \begin{cases} 1/\Delta^3 \rightarrow \text{if } |x_i - \zeta_i| < \Delta x_i/2 \\ 0 \rightarrow \text{ otherwise} \end{cases} \tag{12}$$

And the first filter is defined as: $\Delta = (\Delta x \Delta y \Delta z)^{1/3}$

Δ: Cut-off width in LES models.

After applying the spatial filter, the filtered NS equations are:

$$\frac{\partial \bar{u}_i}{\partial x_i} = 0 \tag{13}$$

$$\rho\frac{\partial \bar{u}_i}{\partial t} + \rho\frac{\partial(\overline{u_i u_j})}{\partial x_j} = -\frac{\partial p}{\partial x_i} + \frac{\partial}{\partial x_j}[\mu\left(\frac{\partial \bar{u}_i}{\partial x_j} + \frac{\partial \bar{u}_j}{\partial x_i}\right)] \tag{14}$$

The interactions between large scale filtered eddies $\bar{u}_i$ and the Sub Grid-Scale (SGS) modeled eddies u' lead to the nonlinear term $\overline{u_i u_j}$ written as:

$$\overline{u_i u_j} = \bar{u}_i\bar{u}_j + \overline{u_i u'_j} + \overline{u'_i u_j} + \overline{u'_i u'_j} = \bar{u}_i\bar{u}_j - \tau_{ij}^{SGS} \tag{12}$$

After substitution, the filtered NS equation can be expressed as:

$$\rho\frac{\partial \tilde{u}_i}{\partial t} + \rho\widetilde{u_j}\frac{\partial(\widetilde{u_i})}{\partial x_j} = -\frac{\partial \tilde{p}}{\partial x_i} + \frac{\partial \widetilde{\tau_{ij}}}{\partial x_j} - \rho\frac{\partial \tau_{ij}^{SGS}}{\partial x_j} \tag{15}$$

$\tilde{u}_i$: Favre-averaged velocity in tensor notation

The Navier-Stokes equations are averaged over the cell volume [93] and, as with Reynolds averaging, produce unknown stresses related to SGS motion. These stresses (τ_{ij}) are given by:

$$\tau_{ij} = -2\rho\vartheta_t S_{ij} \tag{16}$$

Where ρ is the fluid density, ϑ_t is the eddy viscosity, and S_{ij} is the local mean strain rate:

$$S_{ij} = 0.5\left(\frac{\partial u_i}{\partial x_j} + \frac{\partial u_j}{\partial x_i}\right) \tag{17}$$

The eddy viscosity is determined using a mixing-length relationship:

$$\vartheta_t = l^2(2S_{ij}\frac{\partial u_i}{\partial x_j})^{1/2} \tag{18}$$

The mixing length, l, is the characteristic length of unresolved eddies, defined as:

$$l = \min\,(C_s h, \kappa d_{wall})$$

where Cs is the Smagorinsky constant, κ is the von Karman constant and d_{wall} is the normal distance to the nearest wall, and h is the representative mesh interval:

$$h = \sqrt{\frac{dx^2 + dy^2 + dz^2}{3}}$$

where dx, dy, dz are the local mesh dimensions in the three coordinate directions.
Further details of this model can be found in [82,94].

3.4.2.3.Detached Eddy Simulation (DES) models

The best performance in the RANS model was observed in the near-wall region. However, the LES model showed its best performance anywhere in the simulation area except the near-wall region. The DES model employs the specification of both RANS and LES approaches, leading to a potentially more accurate model. The large-scale turbulent flow structures are typically addressed by the LES model [95]. It has been proven that the DES approach is more economical in computational costs while generating highly accurate results [96,97].
The turbulence specific dissipation rate equation is as follows:

$$\frac{D\tilde{\nu}}{Dt} = c_{b1}\tilde{S}\tilde{\nu} + \frac{1}{\sigma}\left[\nabla.\left((\nu + \tilde{\nu})\nabla\tilde{\nu}\right) + c_{b2}\nabla\tilde{\nu})^2\right] - c_{\omega 1}f_\omega[\frac{\tilde{\nu}}{d}]^2 \tag{19}$$

Where $\tilde{\nu}$ is the working variable,

$$\tilde{S} \equiv S + (\frac{\tilde{\nu}}{\kappa^2 d^2}) f_{\upsilon 2}, \ f_{\upsilon 2} = 1 - \chi/(1 + \chi f_{\upsilon 1}) \tag{20}$$

and S is the magnitude of the vorticity. The eddy viscosity ϑ_t is obtained from

$$\vartheta_t = \tilde{\nu} f_{\upsilon 1}\ , \ f_{\upsilon 1} = \chi^3/(\chi^3 + c_{\upsilon 1}^3), \ \chi \equiv \tilde{\nu}/\upsilon \tag{21}$$

where υ is the molecular viscosity. The function f_ω is given by

$$f_\omega = g[\frac{1+c_\omega^6}{g^6+c_\omega^6}]^{1/6}, \ g = r + c_{\omega 2}(r^6 - r), \ r \equiv \frac{\tilde{\nu}}{\tilde{S}\kappa^2 d^2} \tag{22}$$

For further details and values of the coefficients, the reader may refer to [98].

3.4.3. Wall-normal distance of first grid cell

Large Reynolds numbers of the confluence model make it computationally impractical to place the near wall grid point within one wall unit (z+) from solid boundaries, where

$$z^+ = \frac{z u_\tau}{\nu}$$

and u_τ is the friction velocity, z is the absolute distance from the wall, ν is the kinematic viscosity. However, wall model LES (WMLES), i.e., LES with wall functions, overcomes this requirement by identifying the primary grid point within the log-law region (30 < z+ < 500). Although details of near-bed turbulence are not obtained, the wall modelled approach has been widely applied to investigate large-scale turbulent phenomena within the outer region of the water column in flume and fluvial applications [80]. A velocity-based wall function was employed to ascertain the near-wall turbulent viscosity and bed shear stress caused by the rough solid boundary. This condition was met for all the simulations, with z+ being usually above 30.

3.4.4. Mesh sensitivity analysis and Verification of turbulent kinetic energy (TKE)

The meshes used in this study were specified based on the mesh sensitivity and independency analysis and used for the validation described in section 3. Mesh sensitivity analysis was performed to choose the optimum mesh size, by finding the coarsest mesh size for which velocity results did not differ for a finer mesh. The developed model was thus run with three cell numbers of 801254, 1004209 and 1205052 for RANS models. It was found that velocity results did not change substantially (around 0.04%) between the 1004209 and 1205052 meshes, thus the 1004209 mesh was selected for RANS group. Also, 6376502 was chosen for LES group based on verification of TKE.

Table 3. Numbers of mesh cells.

Turbulence model	Number of cells	Number of cells	Number of cells	Number of cells	Number of cells
	Round 1			Round 2	
RANS	801254	1004209	1205052	-	-
LES	801254	1004209	1205052	6376502	7456287
DES	801254	1004209	1205052	6376502	7456287

Pope (2004) [99] suggested that in order to use LES models effectively, it is important to resolve at least 80% of the TKE (k_{res}) on the mesh. According to equation 20, over 80% of the cells in both simulations meet this requirement.

$$K_{res} = \frac{1}{2}(\overline{u'^2} + \overline{v'^2} + \overline{w'^2}) \tag{23}$$

where u', v', and w' are the velocity fluctuations in the streamwise, lateral, and vertical directions, and the overbars represent time-averaging.

3.5.Results and Discussion

3.5.1. Model Validation and Comparison

Figure 15 to Figure 20 provide a detailed examination of the time-averaged velocity streamwise component (U) for both LES and DES simulations, as well as the velocity streamwise component for RANS models, at various points along the bed as indicated by circles in Figure 12. The results of the simulations show a reasonable level of agreement with the experimental data, however, there is room for improvement in some areas closest to the bed. It is suggested that a different approach, such as not using wall functions, may be needed to achieve better results. The study by Yu et al. (2020) [16] does not provide water depth data for further validation of the simulated results.

3.5.2. Velocity

Figure 15 to Figure 20 show the measured and modeled streamwise velocity at 9 profiles where U is the streamwise velocity (m/s) and Z is the elevation above the bottom of the flume (m). The selected profiles were located in the intersection of the main and tributary channel (X=-0.1), near the downstream junction corner (X=0), and after the junction including the flow separation zone (X=0.3;Figure 17 and Figure 20).

In general, greater deviations from the experimental data were observed for the rigid lid simulations (Figure 18 to Figure 20) than the VoF approach (Figure 15 to Figure 17). Under VoF approach, the streamwise velocities before the junction (X=-0.1) and at the junction (X=0) were in better agreement with experimental data than after the junction (X=0.3). This could be due to eddies caused by the merging of the tributary and main flows, which impeded a precise compliance with the data obtained from the experiment. According to Dinh Thanh et al., (2010) [100], the complexity of the flow features in X=0.3 could be ascribed to the separation/recirculation zone and secondary flow.

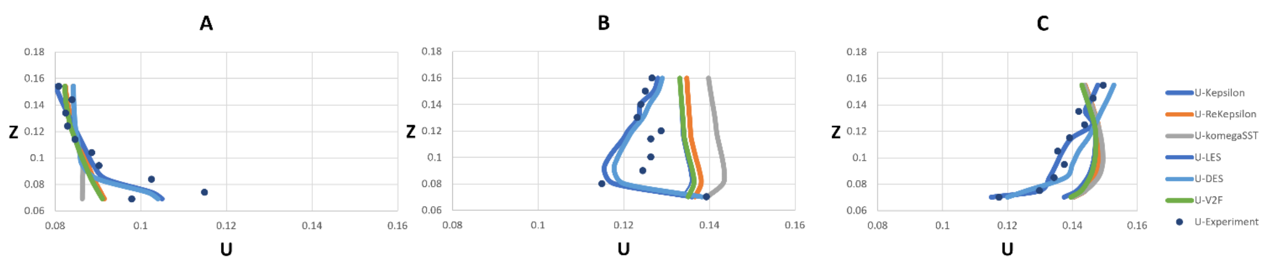

Figure 15. Measured and modeled streamwise velocities (m/s) (Volume of Fluid) at X=-0.1 and A) Y=0.05 B) Y=0.21 C) Y=0.35. The height of channel (Z) is identical for all cases.

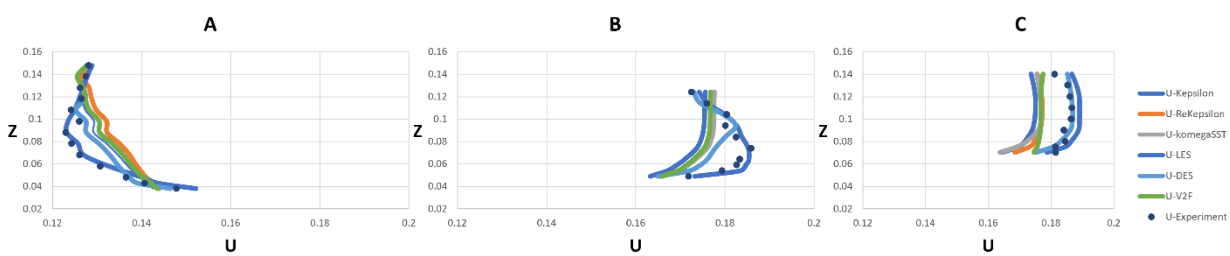

Figure 16. Measured and modeled streamwise velocities (m/s) (Volume of Fluid) at X=0 and A) Y=0.05 B) Y=0.21 C) Y=0.35. The height of channel (Z) is identical for all cases.

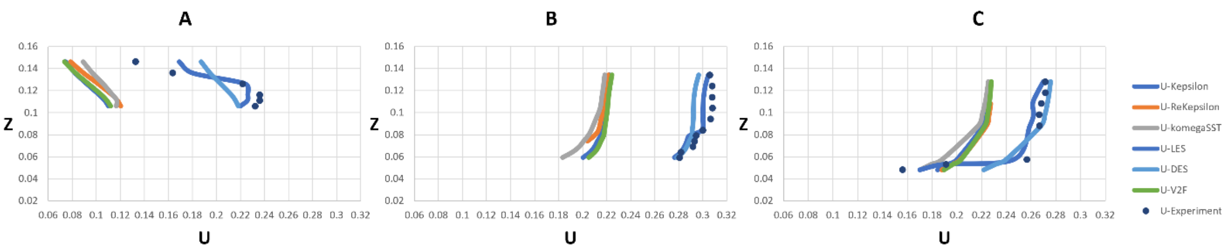

Figure 17. Measured and modeled streamwise velocities (m/s) (Volume of Fluid) at X=0.3 and A) Y=0.05 B) Y=0.21 C) Y=0. 35. The height of channel (Z) is identical for all cases.

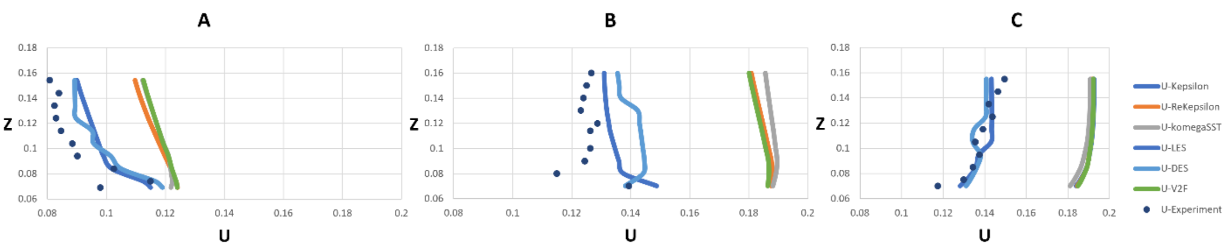

Figure 18. Measured and modeled streamwise velocities (m/s) (Rigid lid) at X=-0.1 and A) Y=0.05 B) Y=0.21 C) Y=0.35. The height of Figures (Z) is identical for all cases.

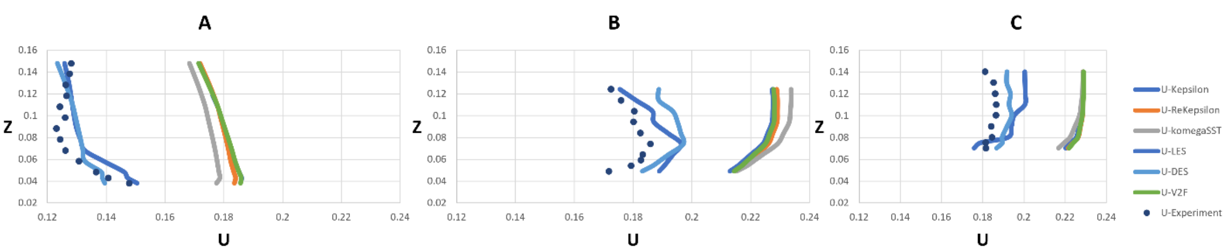

Figure 19. Measured and modeled streamwise velocities (m/s) (Rigid lid) at X=0 and A) Y=0.05 B) Y=0.21 C) Y=0.35. The height of Figures (Z) is identical for all cases.

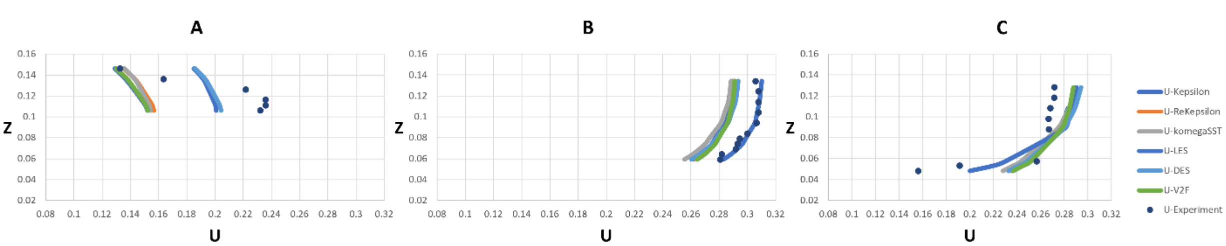

Figure 20. Measured and modeled streamwise velocities (m/s) (Rigid lid) at X=0.3 and A) Y=0.05 B) Y=0.21 C) Y=0.35. The height of channel (Z) is identical for all cases.

At first glance, there appears to be only small differences in predicted flow velocity between the six turbulence models and two different free surface methods (i.e., VoF and rigid lid). Nevertheless, a statistical analysis is required to reveal their detailed differences. The statistical analysis involved calculation of the root mean square error (RMSE) and normalized root mean square error (NRMSE) for 6 turbulence models and two flow surface models (see Table 4 andTable 5):

$$\mathrm{RMSE} = \sqrt{\frac{\sum(\mathrm{U_{experiment}} - \mathrm{U_{Simulation}})^2}{\mathrm{n}}} \tag{24}$$

$$\mathrm{NRMSE} = \frac{\mathrm{RMSE}}{\mathrm{Ave(U_{Simulation})}} \tag{25}$$

where n is the number of observation data and U is streamwise velocity.

The LES model provided the lowest average velocity error in both methods (i.e., VoF and rigid lid) compared to the other five turbulence models applied in this study. This model also provided the minimum error percentages in the average value of all the cross-sections as well as within most individual sections. This result suggests that the LES model is more reliable for predicting flow velocities in complex flow geometries such as confluent channels than the other five turbulence models. Based on the statistical indicators in Table 4 and Table 5, it can also be concluded that the k-ω SST model is not a viable method to simulate cases with complex geometry.

The average range of the error for the VoF and rigid lid methods were computed to be 3% to 16% and 15% to 26%, respectively, which shows the reliability of the VoF method in this case. Thus, subsequent flow structure analysis will be presented using the model results under the LES turbulence model and VoF method. Finally, the error values for the other turbulence models did not follow a consistent trend. It is noteworthy that most of the turbulence models used in this study revealed a reliable error percentage at most profiles except for the profile at X=0.3, Y=0.05. This profile was located in the separation zone with small eddies, which makes it more difficult to predict the flow behavior in this zone.

Table 4. RMSE and NRMSE of the simulated velocity data vs. experimental data with VoF method.

X (m)	Y (m)	Error	k-ε	Realizable k-ε	k- ω SST	LES	DES	V2F
-0.1	0.05	RMSE (m/s)	0.009	0.009	0.011	0.005	0.006	0.009
		NRMSE (-)	0.10	0.10	0.12	0.06	0.07	0.10
-0.1	0.21	RMSE (m/s)	0.010	0.011	0.016	0.005	0.005	0.010
		NRMSE	0.08	0.09	0.13	0.04	0.04	0.08

-0.1	0.35	RMSE (m/s)	0.010	0.011	0.012	0.002	0.005	0.011
		NRMSE	0.07	0.08	0.08	0.01	0.03	0.07
0	0.05	RMSE (m/s)	0.004	0.006	0.005	0.002	0.003	0.005
		NRMSE	0.03	0.05	0.04	0.02	0.02	0.04
0	0.21	RMSE (m/s)	0.009	0.007	0.007	0.002	0.005	0.007
		NRMSE	0.05	0.04	0.04	0.01	0.03	0.04
0	0.35	RMSE (m/s)	0.012	0.009	0.011	0.003	0.003	0.008
		NRMSE	0.07	0.05	0.06	0.02	0.01	0.04
0.3	0.05	RMSE (m/s)	0.104	0.096	0.094	0.017	0.028	0.103
		NRMSE	0.51	0.47	0.46	0.08	0.14	0.51
0.3	0.21	RMSE (m/s)	0.084	0.081	0.092	0.005	0.010	0.081
		NRMSE	0.28	0.27	0.31	0.02	0.03	0.27
0.3	0.35	RMSE	0.042	0.040	0.045	0.008	0.028	0.041
		NRMSE	0.17	0.16	0.18	0.03	0.11	0.17
		Average NRMSE	0.15	0.15	0.16	0.03	0.15	0.15

Table 5. RMSE and NRMSE of the simulated data vs. experimental data with rigid lid method.

X	Y	Error	k-ε	Realizable k-ε	k-ω SST	LES	DES	V2F
-0.1	0.05	RMSE (m/s)	0.026	0.026	0.027	0.028	0.027	0.027
		NRMSE	0.28	0.28	0.30	0.31	0.30	0.30
-0.1	0.21	RMSE (m/s)	0.070	0.071	0.073	0.061	0.073	0.070
		NRMSE	0.60	0.61	0.63	0.53	0.63	0.60
-0.1	0.35	RMSE (m/s)	0.053	0.053	0.051	0.049	0.051	0.053
		NRMSE	0.36	0.35	0.34	0.33	0.34	0.36
0	0.05	RMSE (m/s)	0.004	0.006	0.005	0.002	0.003	0.005
		NRMSE	0.03	0.05	0.04	0.02	0.02	0.04
0	0.21	RMSE (m/s)	0.009	0.007	0.007	0.002	0.005	0.007
		NRMSE	0.05	0.04	0.04	0.01	0.03	0.04
0	0.35	RMSE (m/s)	0.012	0.009	0.011	0.003	0.003	0.008
		NRMSE	0.07	0.05	0.06	0.02	0.01	0.04
0.3	0.05	RMSE (m/s)	0.104	0.096	0.094	0.017	0.028	0.103
		NRMSE	0.51	0.47	0.46	0.08	0.14	0.51

0.3	0.21	RMSE (m/s)	0.084	0.081	0.092	0.005	0.010	0.081
		NRMSE	0.28	0.27	0.31	0.02	0.03	0.27
0.3	0.35	RMSE (m/s)	0.042	0.040	0.045	0.008	0.028	0.041
		NRMSE	0.17	0.16	0.18	0.03	0.11	0.17
		Average NRMSE	0.26	0.25	0.26	0.15	0.18	0.26

In the comparison between the rigid lid and VOF approaches for a channel confluence described above, it was shown that the VOF method provides better results than the rigid lid approach. This is due to the significant role of the free surface variations in flow structure. In the rigid lid method, however, water surface is assumed to be constant, and this effect is simulated by an increased surface pressure at the location of superelevation. While this approach can be reasonable to some extent, it is not as accurate as simulation of actual free surface, which is accomplished using the VOF method.

3.5.3. Turbulence characteristics

Figure 21 and Figure 22 display the TKE profiles from the LES-VOF simulation at six locations along the X=-1 and X=0.3 plane in the main channel, which has the highest level of turbulence. Despite similarities, some variations can be seen, which could be caused by the less precise temporal resolution of the acoustic Doppler velocimetry measurements in the study by Yu et al. (2020) [40].

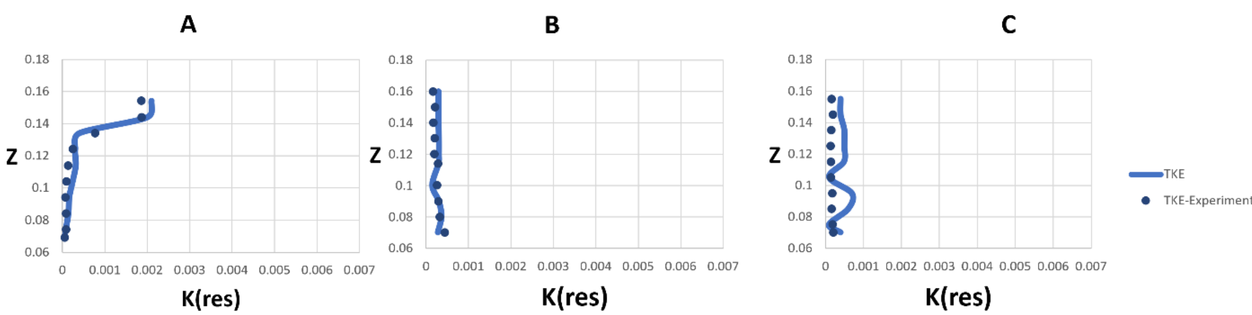

Figure 21.Comparison of measured and predicted TKE profiles at X=-0.1 and A) Y=0.05 B) Y=0.21 C) Y=0.35.

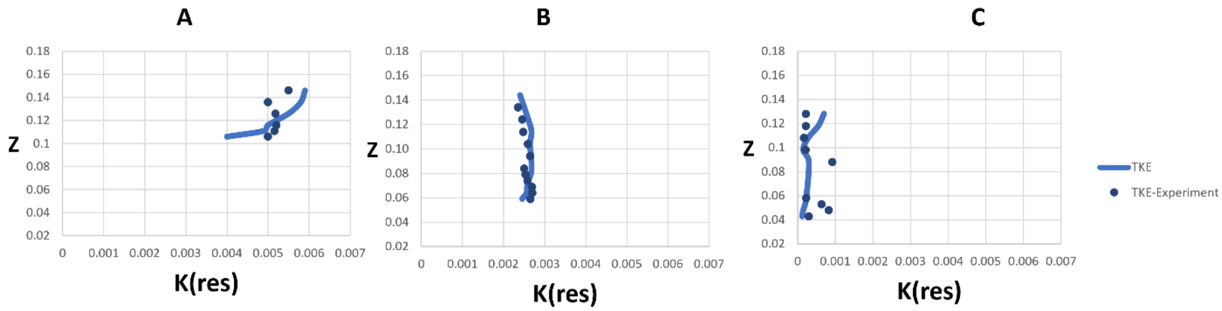

Figure 22. Comparison of measured and predicted TKE (resolved) profiles at X=0.3 and A) Y=0.05 B) Y=0.21 C) Y=0.35.

3.6. LES Deformed Bed Versus Flatbed

3.6.1. Time-averaged Longitudinal Velocity field

Figure 23 shows the time-averaged surface longitudinal velocity field of the confluent channel surface over 100 timesteps after reaching the steady state in the LES model under VoF approach for flat and degraded morphology, which, as shown above, had the lowest errors of the tested models. As shown in the figure, velocities in the upstream main and tributary channel were relatively low. However, after the intersection of the two channels, the velocity increased and reached the maximum value. The separation zone refers to the region near the wall downstream of channel junctions where the velocity of the flow is reduced. The recirculation within these separation zones is depicted by negative velocities, suggesting a motion against the upstream direction. From Figure 23 It is evident that the separation zone is larger in a flatbed compared to a degraded bed. The highest velocities are observed immediately after the junction in the primary flow region of the main channel, which is constricted by the presence of the separation zone. The maximum velocity moved from the junction towards the outer bank of the downstream main channel. In cases of a degraded bed, the reduction in maximum velocity may be attributed to the enlargement of the constricted section caused by scour.

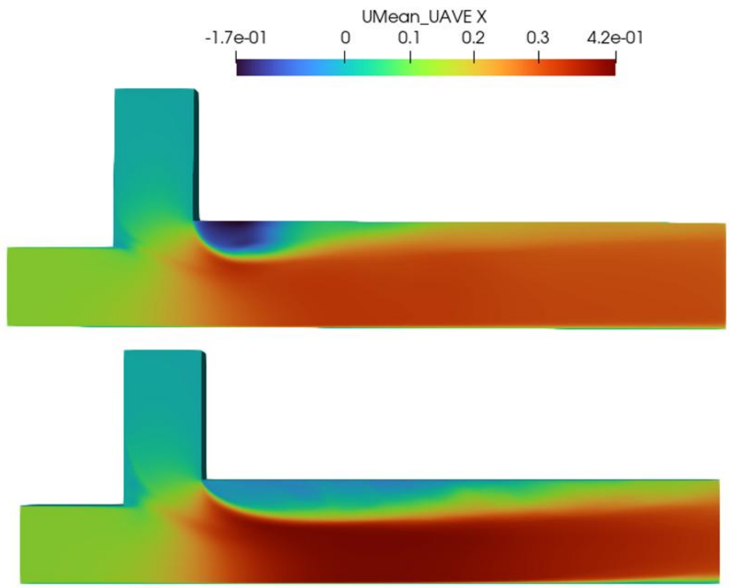

Figure 23. Distribution of time-averaged Longitudinal Velocity (m/s) after reaching the steady state (top; degraded bed, bottom; flatbed)

Figure 24 shows the distribution of time-averaged longitudinal velocity after reaching the steady state at X=0.2 for degraded and flatbeds. The velocity patterns differ between the near surface and near bed regions, especially when the bed is degraded. Near the surface, the separation zone is larger in terms of length and width, which varies from top to bottom due to the angle at which the branch channel flow enters. There is also increased recirculation within the separation zone near the surface, which will be explained in more detail later.

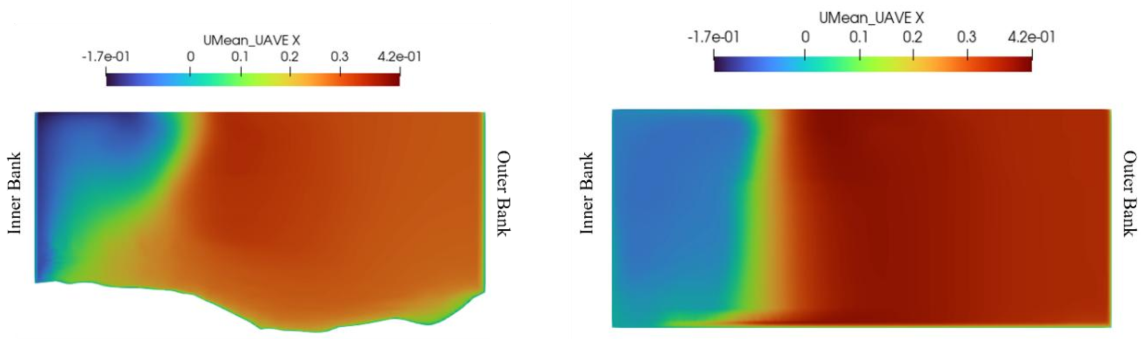

Figure 24. Distribution of time-averaged Longitudinal Velocity (m/s) after the steady state at X=0.2 (Left; degraded bed, Right; flatbed)

3.6.2. Streamlines

Figure 25 presents an illustration of the flow patterns observed in a confluence zone. The figure displays streamline of the simulated time-averaged velocity fields, which indicate an increase in flow velocity towards the downstream confluence for both the flatbed and degraded bed scenarios. The flow streamlines were based on averaging 100-time steps of the LES model under VoF approach were processed using ParaView. In the flatbed case, the flow separates at the corner and forms a recirculation zone, while in the degraded bed case, the streamlines are concentrated in the scour hole and guided upstream by the depositional bar, resulting in a smaller recirculation zone. Furthermore, the streamlines are color-coded based on the streamwise velocity component, revealing that there is less contraction of the main channel flow in the degraded bed case next to the separation zone. Also, while the flow streamlines in the upstream were mostly parallel, as the flow approached the junction, the streamlines tended to be concentrical, creating strong flow curvature in the confluence. Rotating flow at the corner of the junction, which occurred due to the separation zone, is also illustrated in this figure. The results of the simulation indicated the capability of the LES model to predict both flow curvature in the confluence and recirculation in the separation zone.

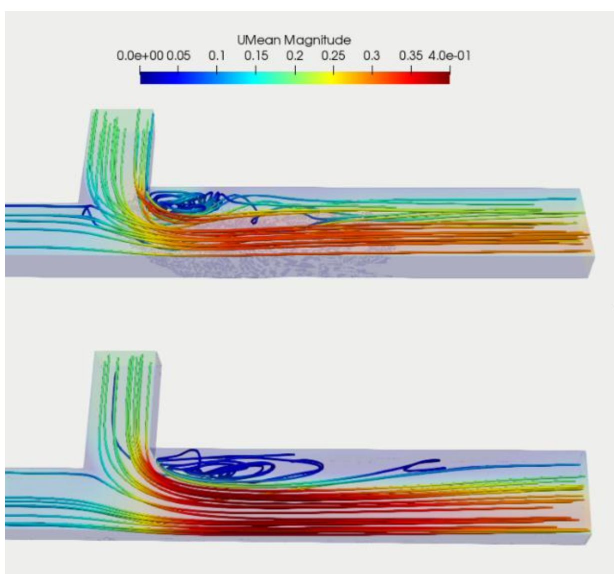

Figure 25. Streamlines of simulated time-averaged flow velocity (m/s) in confluence channel with LES model: top, degraded bed; bottom, flatbed. Light blue (upstream main channel) and green (tributary channel) streamlines merge and establish the red

streamlines (high velocity) in the downstream of the junction. Separation zone is displayed by interwoven blue streamline (top; degraded bed, bottom; flatbed)

3.6.3. v-w vector characteristics

To better illustrate the time-averaged velocity field, Figure 26A (degraded bed), B (flatbed) displays the X=0.65 cross-section of the downstream channel, with the in-plane component (v; w) depicted using vectors and the normal component (u) through color representation. Secondary circulation cells evident in the vector distributions are labelled. Additionally, flow streamlines for each case at the same section are shown in Figure 26C and D.

The separation zone in the flatbed scenario exists throughout the entire water column, but it has two vertically stacked counter rotating recirculation cells, and its width becomes narrower near the bed. Alternatively, the separation zone in the degraded bed case is wider near the bed and most importantly its transverse secondary circulation cells have different rotation than in the flatbed case. This may be related to the more significant lateral velocity vectors in the degraded bed scenario, which does not display circulation cells outside of the separation zone at X=0.65. On the other hand, Figure 26 (B and D) highlights that in the flatbed case two counter-rotating cells occur in the main confluence flow outside of the separation zone. One narrow clockwise circulation cell is directly adjacent to the separation zone shear layer and is associated with the tributary flow path. The other larger cell is associated with the main channel flow. The presence of these two cells illustrates the merging of the tributary flow into the main channel flow. To examine this process further, Figure 27 provides streamlines at sections upstream and downstream for both cases. Immediately upstream (X=0.50) in the flatbed case the narrow central cell is larger with greater circulation before integration (Figure 27B), whereas complete mixing of the two flows has occurred further downstream (Figure 27D). These results portray the cohesive convergence of the two flow paths and provide a concise visual representation of the confluence hydrodynamics. Interestingly, the main channel cell begins to develop further downstream (X=0.95) in the degraded bed case (Figure 27D), indicating the evolving nature of the flow patterns along the studied reach.

The bed shear, which is influenced by the secondary circulation cells, contributes to the scouring that can be seen in the cross-section of the degraded bed case. In open channel confluences, the momentum near the surface is generally greater than near the bed. This is due to the acceleration of water near the surface caused by velocity gradients resulting from the merging of tributary and main channel flows. The presence of roughness at the boundary of a fluid flow significantly influences the velocity and momentum distribution, resulting in reduced values near the bed compared to the free surface. This variation in momentum distribution has significant implications for flow dynamics, sediment transport, and channel morphology in confluence regions. Due to the greater lateral momentum near the surface compared to near the bed, the water at the surface has a noticeable velocity towards the shear layer. The water surface is slightly deflected by the incoming water from the main channel. This generates a secondary current that is visible in the depicted diagram (Figure 26B). The cross-sections also show that the secondary flow in the degraded bed scenario is notably distinct from the one in the flatbed scenario, primarily because of the existence of the depositional bar.

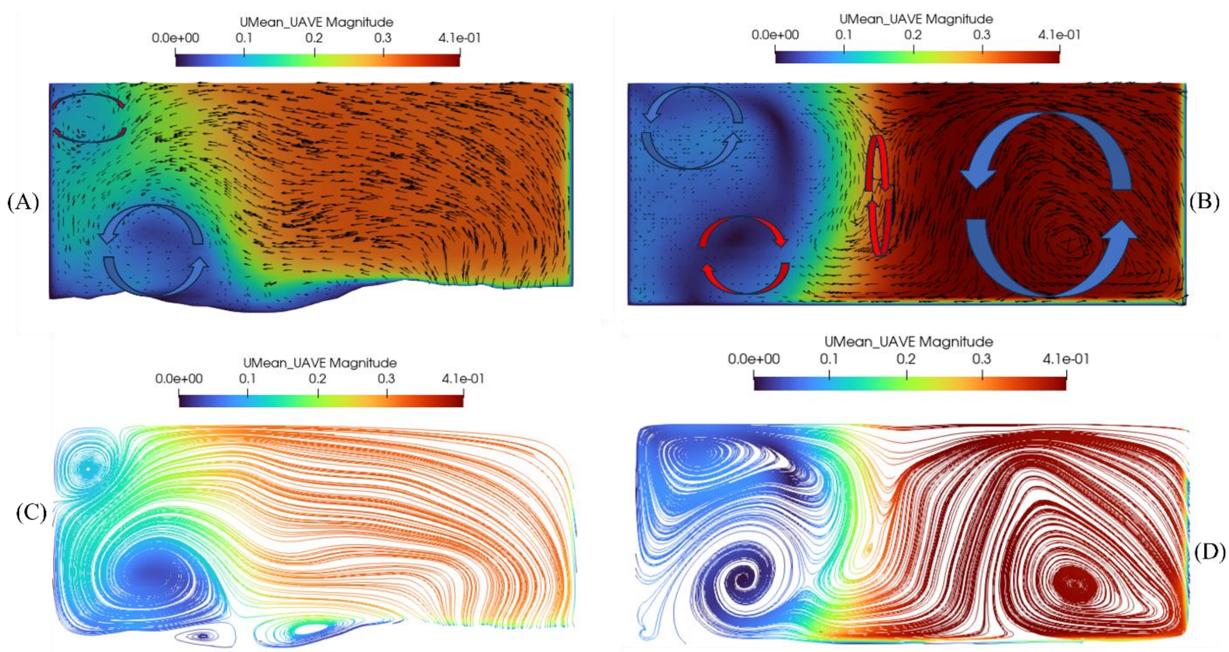

Figure 26. Cross-sections of time-averaged streamwise velocity in downstream main channel at X=0.65 (facing downstream), also showing (A , B) in-plane component of time-averaged velocity (v-w vectors), and (C, D) streamlines (right: flatbed case; left: degraded bed case).

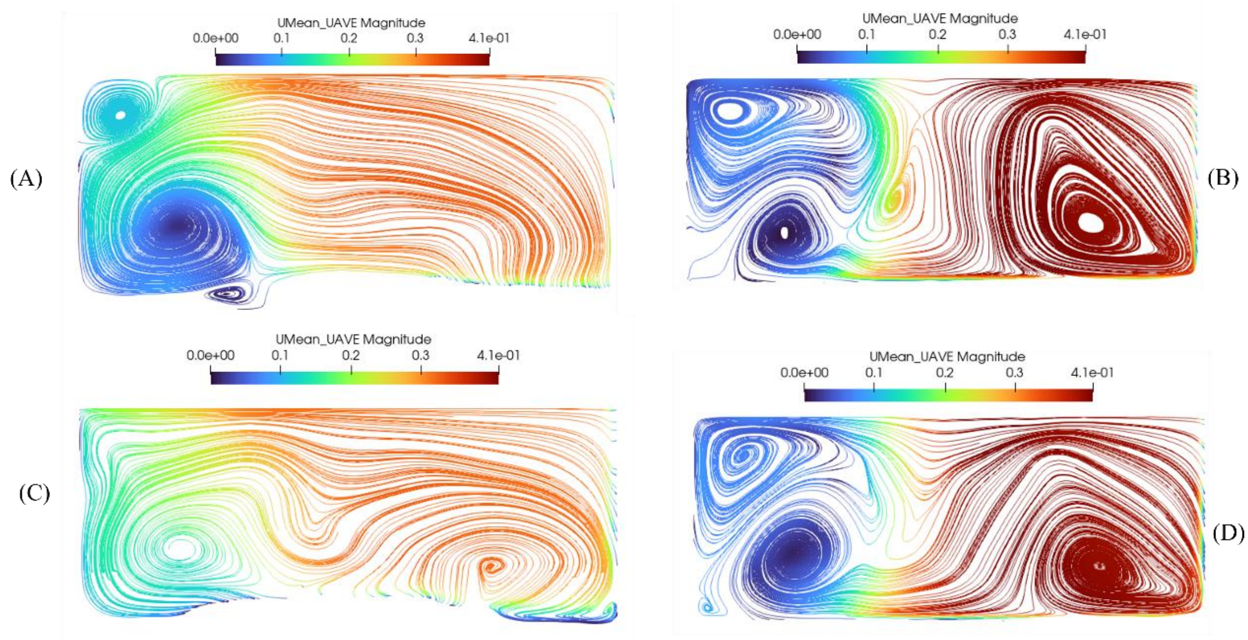

Figure 27. Cross-sections of time-averaged streamwise velocity in downstream main channel of flatbed case at X=0.50 (B) and X=0.80 (D) and degraded bed at X=0.50 (A) and X=0.95 (C)

3.6.4. Vorticity

The mixing structure of the two cases displays variations, which are also evident in the patterns of vorticity, as shown in a horizontal plane near the free surface (Figure 28) and in sections (Figure 29) These variations result primarily from differences in geometry and the interactions between the separated shear layers on either side of the separation zone [101]. In both situations, a strong shear layer arises close to the inner bank. The blue (negative) vorticity near the inner bank in the degraded bed case (Figure 28top, Figure 29) A, B) is consistent with reverse secondary circulation in the recirculation zone (Figure 26A, C), which is caused by the sudden drop in flow depth in this area due to the presence of the upstream bar. The results depicted in Figure 29 demonstrate how the characteristics of the flume and flow affect the behavior of the vortical structures in the separation zone.

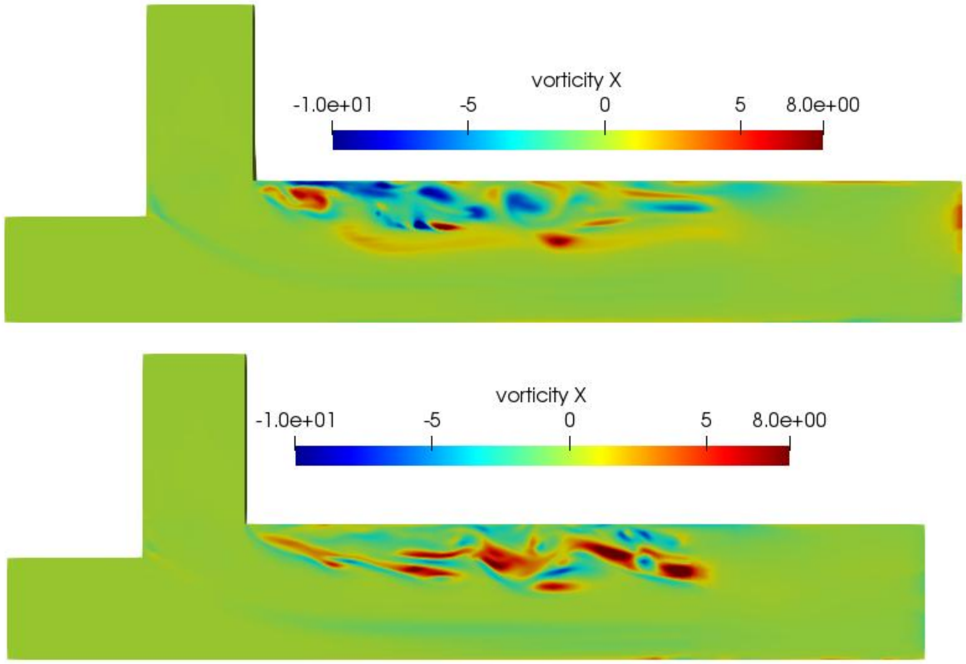

Figure 28. Distribution of the vorticity, in the instantaneous flow (Z=0.12) (top: degraded bed, bottom: flatbed)

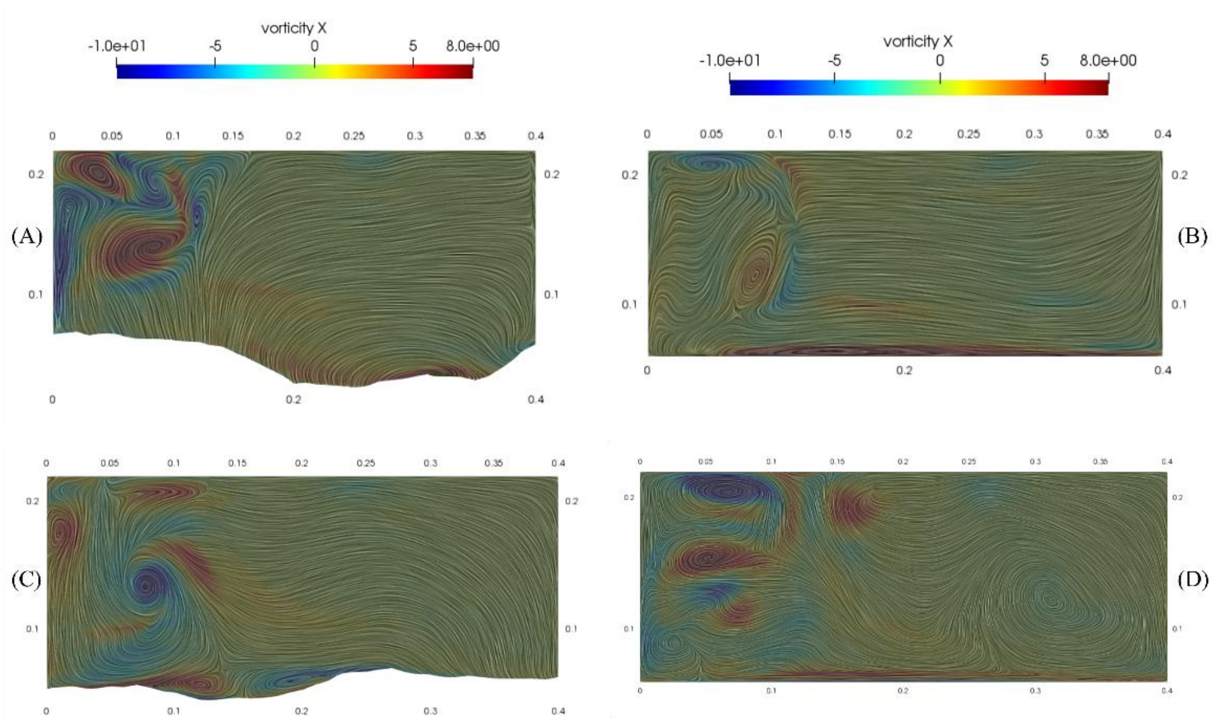

Figure 29.Distribution of the vorticity (left: degraded bed, right: flatbed) (A&B; X=0.2 and C&D; X=0.65)

3.6.5. TKE

TKE was investigated into two different cross-sections for both flat and degraded bed. For instances of degraded beds, significant values of TKE are noticed in the mixing layer between the converging flows (refer to cross-section x=0.3 in Figure 30 A&B). Values are even higher in the shear layer around the related recirculation zone (RZ). Moving away from the RZ, the TKE values decrease and the TKE distribution expands. This can be seen in the cross-section x=0.6 of Figure 30 C&D.

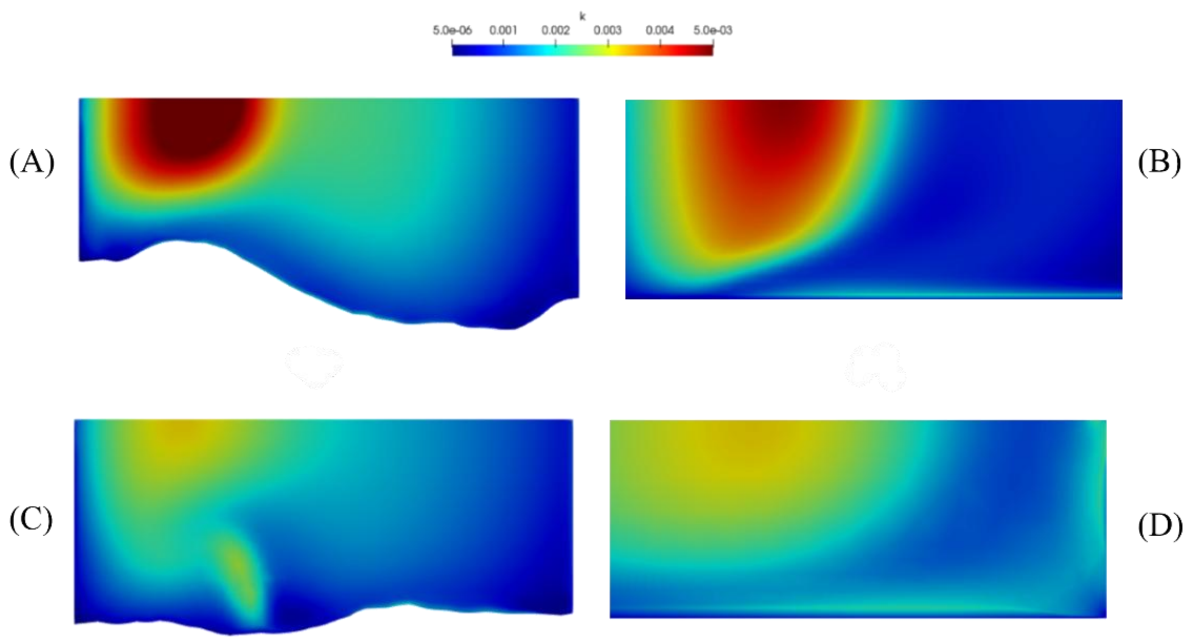

Figure 30. Cross-section at X=0.3(A, B) and X=0.6 (C, D) showing the TKE (m^2/s^2)

3.7. Conclusions

A confluence channel with a degraded bed and flatbed were modeled and investigated under a number of turbulence models with two surface models using 3D OpenFOAM to compare the accuracy of six different turbulence models [RANS (standard k–ε, realizable k–ε, k–ω SST, V2F), LES, and DES]. Special attention was given to the flow characteristics in the confluence zone, including secondary currents and coherent vortical structures. Data validation was performed, and the accuracy of the model was analyzed using a statistical assessment. The following highlights could be concluded from this study:

- The simulations captured the flow patterns in the confluence zone, including the formation of recirculation zones and secondary flow, with a strong shear layer forming near the inner bank after the junction. The maximum velocity diverts from the tributary channel to the outer bank of the main channel, with substantial flow curvature through the confluence zone.
- Velocity Prediction: The simulations showed a reasonable level of agreement with the experimental data, particularly for the VoF approach. However, there were areas closest to the bed where improvement is needed. The LES model provided the lowest average velocity error compared to other turbulence models, indicating its reliability in predicting flow velocities in complex flow geometries such as confluent channels. The k-ω SST model was found to be less suitable for simulating cases with complex geometry. In terms of accuracy in both VoF and rigid lid approaches, LES best predicted the confluence flow behaviour followed by realizable DES, k-ε, V2F, K-ε, and K-ω SST. Although it had higher cost of CPU time, a good agreement was observed between the LES-VoF results and the experimental data. On the other hand, RANS family models demonstrated relatively identical poor results with minor differences in the cross-section immediately after the junction.
- VoF method was concluded to be a more promising water surface model for complex structures with compound flow behavior than the rigid lid method.
- The degraded bed scenario exhibited smaller recirculation zones and different secondary flow characteristics compared to the flatbed scenario. The presence of a depositional bar in the degraded bed case affected the flow patterns and secondary circulation.
- In the degraded bed scenario, the recirculation area was discovered to be considerably shorter and narrower or not present at all near the bed as a result of the intricate interplay between the flow and the scour hole and the depositional bar. Secondary circulation in the recirculation zone had different rotation in the degraded bed case than the flatbed case due to the presence of the depositional bar.
- The contraction of the flow in the main channel is weaker in the case of a degraded bed.
- The simulations revealed the formation of vorticity in the confluence zone. The number and behavior of vortices were influenced by the geometry and size of the flow channels.

The interactions between separated shear layers played significant role in the formation and behavior of vortices.

- The generation of vortices in the flow field was mainly ascribed to: (1) variation of the shear layer caused by velocity difference between two channels; and (2) fluid element swirl in the transition zone rooted in the angle between channels.
- The obtained results show the promising applicability of OpenFOAM CFD simulations in resolving the problems associated with the confluence channel design.

4. Experimental Investigation of Positively Buoyant Surface Jet in Confluence Regions

4.1. Abstract

Understanding the influence of ambient currents and jet discharge characteristics on warm polluted outfall performance is crucial for mitigating the ecological impact of effluents discharge in a confluence region. To this end, laser-induced fluorescence (LIF) experiments were conducted to investigate the combined effects of jet strength and nozzle location on the mixing of a positive or neutral jet issuing into a plane perpendicular to the crossflows. The trajectory and mixing within a channel junction of surface crossflow jets is investigated. Two different nozzle discharge locations and velocities were studied to assess the 3D jet trajectory and concentration distribution. The investigations revealed that a jet issued into the main channel mixes more effectively with wider dispersion compared with a jet issued in the tributary. This is due to the shear layer in the main channel, which restricts the jet in tributary to a narrower width, limiting its ability to mix effectively with ambient water.

Keywords: Positively Buoyant Jet, Surface Jet, laser-induced fluorescence, LIF

Article Highlights

- The study examines the influence of ambient currents and jet discharge characteristics on warm polluted outfall
- Laser-induced fluorescence (LIF) experiments were conducted to investigate the combined effects of jet strength and nozzle location on the mixing of a positive or neutral jet.
- The results demonstrated that the discharge rate and buoyancy influenced both the jet trajectory and dilution, with increased velocity and buoyancy leading to enhanced mixing and a wider dispersion of the jet.

4.2. Introduction

Urban development near rivers has led to the increased release of municipal and industrial wastewater into water bodies. Although several studies have explored wastewater movement in rivers, further investigation is needed to understand the impact of effluent discharge on river health [102,103]. The discharge of effluent into flowing water, termed jet in crossflow, has applications in industry, hydraulics, and the environment [42,104–106].

The hydrodynamics of a jet in crossflow is inherently complex, especially when the jet is released in areas of the river with complex structures, such as a confluence channel junction. To the best of the authors' knowledge, the mixing of a jet in a confluence zone has never been investigated. This study aims to investigate effluent discharges released in confluence areas to examine the effect of the junction on the outfall. First, the hydrodynamics of both jets in crossflow and confluences are reviewed briefly in the following sections.

4.3. Jet in crossflow

When a less-dense discharge is introduced into a denser fluid, it gives rise to a positive buoyant jet. Specifically, a positive buoyant surface jet is formed when discharged near the free surface. This phenomenon is commonly observed in both natural and industrial settings, such as the release of heated cooling water [107] and discharge of treated wastewater into water bodies [108]. This method is the most traditional and economical method for releasing pollutants into rivers or coastal areas. Due to their limited dilution factor, usually ten or below, surface discharges tend to pose greater environmental risks compared to submerged alternatives [7].

The dilution factor is a measure of the amount of pollution that has been diluted or reduced in concentration. The dilution factor is calculated using the following equation.

$$\text{Dilution Factor} = \frac{\text{Volume of initial Concentration}}{\text{Volume of final Concentration}} \qquad (26)$$

In equation (1), "Volume of Initial Solution" refers to the volume of the concentrated pollution before dilution, and "Volume of Final Solution" refers to the total volume of the diluted pollution after dilution.

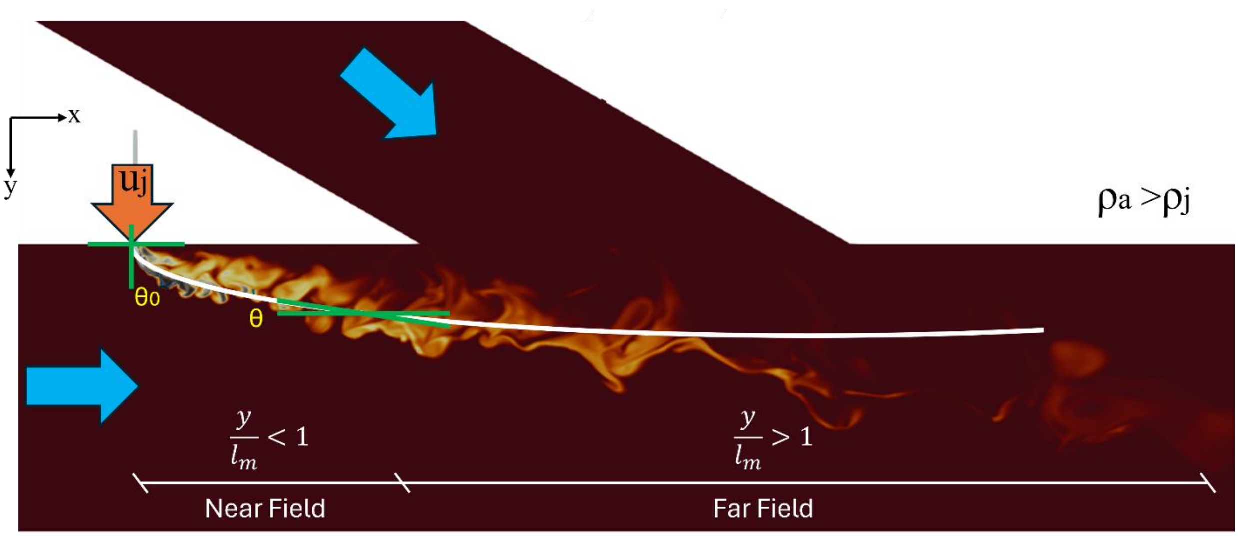

Figure 31. Schematic shape of a positive surface jet in crossflow with the approximate location of near and far field. (Top View). l_m is the jet-in-crossflow length scale.

The trajectory of the jet is established by connecting the points with the maximum time-averaged concentration in each cross section (Figure 31). The angle θ represents the inclination angle of the jet, signifying the direction angle of the instantaneous velocity along the central axis in relation to the crossflow direction (θ_o is the initial angle, while θ denotes angles along the trajectory). Theoretically, θ reaches zero degrees at the end of the trajectory.

The length-scale parameters for buoyant surface jet classifications were introduced by Jirka et al. [60], and Chu and Jirka [63] provided an initial classification for buoyant surface jets in crossflows. A comprehensive classification system by Jones et al. [7] categorized surface jets into four main classes as either free jets, shoreline-attached jets, wall jets, or upstream intruding plumes, using the parameters defined in Table 6 and Table 7 where a_0 is the cross-sectional area of the jet, g is the gravitational acceleration, ρ is the water density, and $\Delta\rho_0$ is the difference in discharge density ($\Delta\rho_0 = \rho_a - \rho_0$).

Table 6. Dynamic length scales of jets

Discharge length scale	$L_Q = Q_0/M_0^{1/2}$
Jet-to-plume length scale	$L_M = M_0^{3/4}/J_0^{1/2}$
Jet-to-crossflow length scale	$l_m = M_0^{1/2}/\overline{u_a}$
Plume-to-crossflow length scale	$l_b = J_0/\overline{u_a}^3$

Table 7.Flow characteristics of jets

Jet flow rate	$Q_0 = \overline{u_0}a_0$
Jet momentum flux	$M_0 = \overline{u_0}Q_0$
Jet buoyancy flux	$J_0 = Q_0\, g_0'$
Discharge buoyant acceleration	$g_0' = g(\Delta\rho_0/\rho_0)$

A crossflow buoyant jet can be categorized into four distinct asymptotic regimes based on whether buoyancy, momentum, or crossflow primarily influences the jet's mixing characteristics (Figure 31) [61]:

- Momentum Dominated Near-Field ($y/l_m << 1$): This regime occurs when the initial jet momentum significantly influences the jet discharge.
- Momentum Dominated Far-Field ($y/l_m >> 1$): In this regime, the crossflow effects become significant in the jet discharge.
- Buoyancy Dominated Near-Field ($y/l_b << 1$): This regime is characterized by the initial plume buoyancy playing a crucial role in the plume discharge.
- Buoyancy Dominated Far-Field ($y/l_b >> 1$): The crossflow effects become prominent in the plume discharge.

where y represents the cross-channel distance, and l_m and l_b are the lengths of the near-field for a momentum-dominated jet or buoyancy-dominated plume, respectively (Figure 31).

Early investigations into surface thermal discharge patterns were initiated by Dunn et al. (1975)[58], followed by computational modeling using mathematical models and turbulence closure techniques [59]. In the 1960s, research focused on surface buoyant jets, prompted by concerns over the environmental impact of heated cooling water discharges from power plants. Notable contributions during this period were laboratory experiments and integral jet models [60].

A surface jet discharging into a crossflow transition along its trajectory. In the "zone of flow establishment" immediately following the nozzle, the flow undergoes a transformation into a sheared jet-like velocity distribution. In this region, buoyancy has a minimal impact, and the flow is primarily governed by the momentum of the jet, conforming to a Gaussian distribution. As the momentum diminishes, the jet shifts towards the crossflow, entering a plume-like condition. Mixing in this zone is influenced by buoyancy effects and secondary flows, which collectively form a near-field zone. In the far field, mixing is predominantly governed by buoyant spreading or passive diffusion (Figure 31) [108], [7].

Researchers have explored surface jets to enhance understanding of these phenomena. Anwar [109] conducted experiments to assess the vertical and horizontal isotherms of warm surface jets (73 ˚C) discharged from a rectangular channel into a cold crossflow (15 ˚C). The study revealed a strong depth dependence of the jet axis, and the mutual interaction between the buoyant surface jet and crossflow generated a zone with overshoot velocity at the outer edge of the jet. Additionally, a slow-moving zone was observed on the lee side of the buoyant jet, along with a return flow closer to the inner wall (near the discharge point) of the flume. Gawad et al. [110] investigated the effects of horizontal surface and submerged jets in crossflows, highlighting similar Gaussian distributions in the excess jet velocity and concentration in both the lateral and vertical directions for cases without strong bank reattachment and recirculation.

Gharavi et al. (2020) [108] conducted experimental measurements of the 3-D velocity field to enhance the understanding of the flow structure of surface jets under crossflow conditions. Stereoscopic Particle Image Velocimetry (PIV) was employed to measure the instantaneous spatial and temporal velocity distributions in a measurement zone downstream of the jet discharge point. This study identified the formation and evolution of vortices in the flow structure. This vortex in the surface jet in crossflow exhibited similarities to one half of the counter-rotating vortex pair (CVP) typical of submerged jets in crossflows. It was inferred that the water surface behaved as a plane of symmetry (Figure 32).

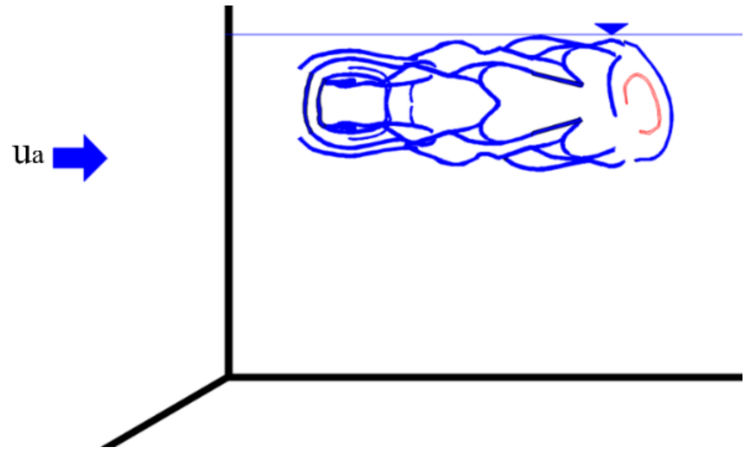

Figure 32. Schematic shape of surface jet [108]

4.4. Confluence Hydrodynamics

Channel confluences are hydrological systems in which two or more channels converge, resulting in complex flow structures. These structures can be challenging to understand and model due to the complexity of the flow physics involved. Over the years, researchers have attempted to gain a better understanding of the behavior of open-channel confluences using experimental methods [10,15–18], numerical methods [31], [32], [33], [34], and field experiments [36,38–40]. Best (1987) [41] proposed a generalized model for river confluences that included six different zones (Figure 33). These zones are characterized by different flow patterns and velocities. The first zone is the stagnation zone, where water from the tributary branch river is impeded by the main river, causing a build-up of water. The second zone is the deflection zone, where the flow from the branch river changes direction to align with that of the main river channel. The third zone is the separation zone, which is the area immediately after the junction close to the inner bank of the main river. The velocity in this zone is usually low, yet highly turbulent with flow recirculation. The fourth zone is the maximum velocity zone, which occurs in the contraction or acceleration zone between the shear layer and outer and inner banks of the main river. The fifth zone is the flow recovery zone, in which the flow begins to recover from the turbulence generated in the shear plane. The sixth and final zone is the shear plane, which occurs at the branch river entrance to the main river and is the primary source of turbulence generation due to differences in their velocity fields.

After the confluence junction, various river characteristics change significantly, including alterations in water surface and bed level. Additionally, a range of phenomena can be observed, such as the transport of sediment, dispersion of pollutants, erosion and deposition processes, and river migration [111].

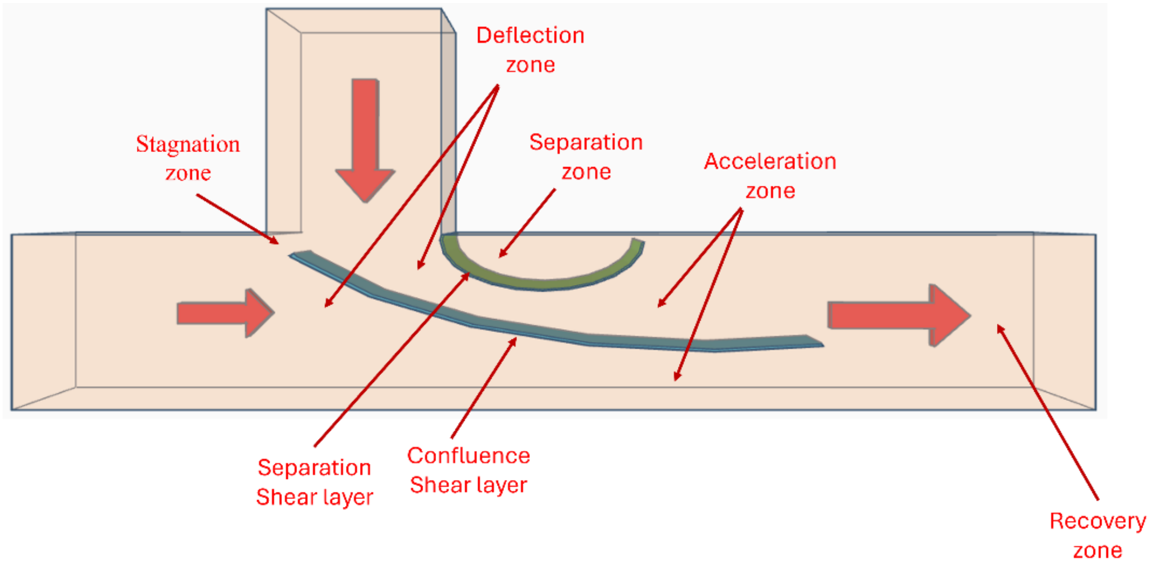

Figure 33. Flow characteristics in channel confluences (based on Best, 1987 [41])

Several key elements, such as junction angle, ratio of discharge or momentum between the main channel and tributary flows, bed level (accordant or discordant), channel geometry, and any differences in density between the incoming flows, can affect the morphodynamics of a confluence [112,65,113,114]. While channel confluences have been studied for several decades, it is evident that examination of these details continues to accelerate [115–118]. Significant research efforts have focused on investigating the phenomenon of flow mixing at confluences [38,119,120]. Furthermore, there has been considerable interest in studying the relationship between sediment transport and the morphology of river systems [40,121,122].

According to previous studies, confluences can be categorized based on their width-to-depth ratio as either small ($W/H < 10$), medium ($10 < W / H < 50$), or large scale ($W / H > 50$) [40,65]. Recently, researchers have explored the possibility of applying findings from small laboratory and field experiments to large rivers, thus this scaling categorization should be considered [123]. It has been suggested that for large width-to-depth ratios, the influence of secondary currents is diminished due to increased roughness caused by the shape of the riverbed. Consequently, it may be challenging to extend observations from small to large-scale confluences [65].

4.5. Objective

Despite numerous investigations into confluence channels or jets in crossflow, there is still a gap in existing studies. To the best of the authors' knowledge, no prior study has explored the dynamics of positively buoyant surface jets in confluence regions. Recognizing this research gap, our study aims to provide a comprehensive investigation of the behavior and characteristics of positively buoyant surface jets in the complex context of confluence regions. We inspect not only the fundamental features of these jets but also their concentration patterns and trajectories within the intricate dynamics of river confluences. Different jet in cross flow categories that can occur when a buoyant surface jet is discharged into a confluence are examined, by considering variable jet location, momentum, and buoyancy. Specifically, laboratory flume experiments were conducted in an open-channel confluence with injection of an effluent jet into either the tributary or main channel upstream of the confluence zone. For various jet and confluence flow scenarios, laser-induced fluorescence was utilized to evaluate the mixing of the effluent within the confluence zone. Through a systematic exploration of this uncharted territory, we seek to contribute valuable insights into the understanding of the flow patterns, turbulence, concentration dynamics, and trajectory behaviors associated with positively buoyant surface jets in confluence areas.

4.6. Methodology

4.6.1. Experimental Setup and Flume Configuration

The experiments were conducted at the Water Resources Engineering Laboratory of the University of Ottawa using a flume designed to simulate confluence-flow scenarios. The flume was 8 m in length, 1.1 m in width, and 0.6 m in depth (Figure 4a). Within the flume, a confluence channel was meticulously designed to replicate river confluence dynamics with the convergence of the two channels positioned 1.1 m downstream of the flume entrance. The upstream main channel and tributary channel were specifically configured with widths of 0.20 m and 0.15 m, respectively. The downstream channel maintained a width of 0.20 m, ensuring a coherent representation of channel dimensions within the experimental setup. The angle between the two channels was set at 30°, which falls within the natural range of observed confluence angles [124]. The flow depth was kept at 10 cm in both channels. For better visualization, the side walls and bottom of the flume were made of tempered glass. Three adjustable speed pumps in parallel were installed under the flume to recirculate water from the flume outlet tank to the flume inlet tank, facilitating controlled flow conditions.

The experimental setup facilitated the discharge of buoyant surface thermal jets into the confluence flow. The jet discharge nozzle was connected to a constant-head tank positioned above the flume. The constant head tank was raised to a height of 0.8 meters above the nozzle tip to maintain a consistent hydraulic driving head for the discharge. Jet flow control was achieved using two valves and the flow rate was quantified using a flowmeter. (Figure 34b). Two distinct scenarios were considered for the surface thermal jet discharge location: one in the main upstream channel, and the other in the tributary channel (Figure 4a). Both scenarios involved initiating the thermal jet through round nozzles with a diameter (d) of 4 mm, approximately 200 mm upstream of the confluence junction, specifically at the water surface, to investigate the influence of the channel hydrodynamics and geometry on the jet behavior.

(a)

(b)

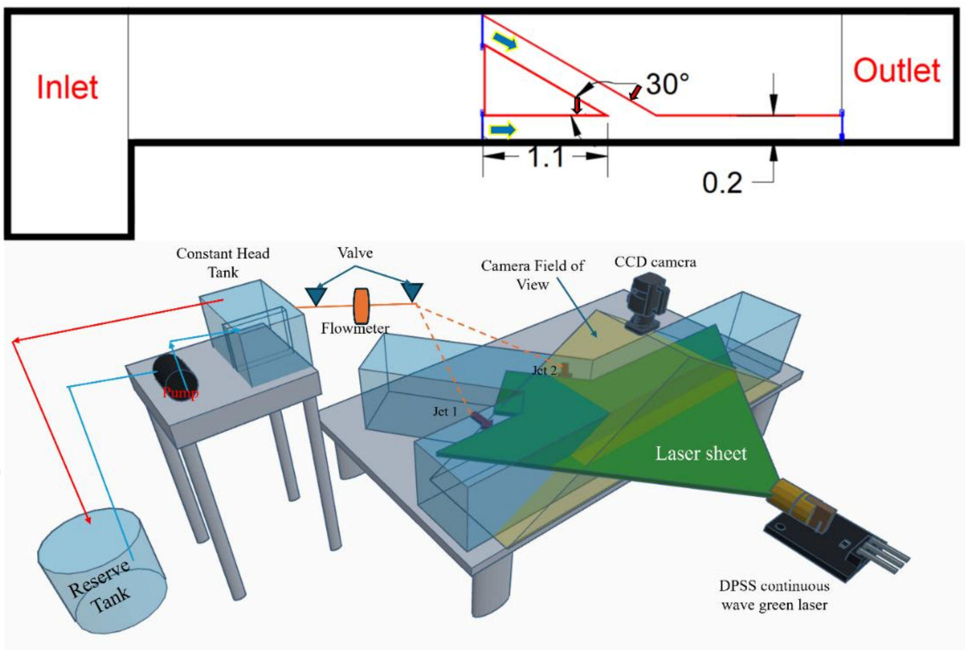

Figure 34. a) plan-view layout of the flume and confluence model (dimensions in m) with confluence flow directions (green arrows) and effluent jet inflow locations (red arrows), b) schematic of the LIF experimental setup,

4.6.2. Experimental Parameters

In this study, a range of jet and ambient conditions was systematically investigated using a nozzle diameter (D) of 4 mm. The jet densiometric Froude number (Fr) (Equation 2) was varied from 2 to 5.4. Table 3 lists the experimental conditions for each test case, emphasizing the key parameters considered in this study. The effluent used in the experiments represents the thermal jet discharge. Fresh tap water was used to simulate ambient conditions within the flume. Control over effluent temperature and density variations was meticulously maintained to replicate realistic thermal jet scenarios. Temperature adjustments were made to ensure a constant temperature between 15 and 25°C for the source discharge and 15°C for the ambient water. The discharge densities ranged from 997 to 999.1 kg/m³, reflecting the variability of the thermal buoyancy effects in the positively buoyant surface jets. The discharge rate from the nozzle was measured using a flowmeter to monitor and control thermal jet characteristics.

$$Fr = \frac{u_j}{\sqrt{g'_0 \times D}} \tag{27}$$

Where u_j is jet velocity and D is nozzle diameter.

Table 8. Experimental conditions

	Q (L/h)	**u_j (m/s)**	**u_{a_m} (m/s)**	**u_{a_b} (m/s)**	**$u_r = u_a/u_j$**	**Jet Density (Kg/m^3)**	**Crossflow Density (Kg/m^3)**	**g'_0**	**Fr**	**L_Q**	**L_M**
R_1(Jet1)	2.50	0.06	0.10	0.02	1.81	997.05	999.70	0.03	5.42	0.004	0.02
R_2(Jet2)	2.50	0.06	0.10	0.02	0.36	997.05	999.70	0.03	5.42	0.004	0.02
R_3(Jet1)	1.00	0.02	0.10	0.02	4.52	996.52	999.61	0.03	2.01	0.004	0.001
R_4(Jet2)	1.00	0.02	0.10	0.02	0.90	996.52	999.61	0.03	2.01	0.004	0.001
R_5(Jet1)	2.50	0.06	0.10	0.02	1.81	997.77	997.77	0.00	_	0.004	_
R_6(Jet2)	1.00	0.02	0.10	0.02	4.52	997.77	997.77	0.00	_	0.004	_
R_7(Jet1)	1.00	0.02	0.10	0.02	0.90	997.77	997.77	0.00	_	0.004	_
R_8(Jet2)	2.50	0.06	0.10	0.02	0.36	997.77	997.77	0.00	_	0.004	_
R_9(Jet1)	2.50	0.06	0.10	0.00	1.81	997.05	999.70	0.03	5.42	0.004	0.02
R_{10}(Jet2)	2.50	0.06	0.10	0.00	0.00	997.05	999.70	0.03	5.42	0.004	0.02

Ambient Velocity (u_a): General ambient velocity in the experimental setup.
Main Channel Velocity (u_{a-m}): Velocity in the main channel.
Tributary Channel Velocity (u_{a-b}): Velocity in the tributary channel.
Velocity Ratio (u_r): The ratio of ambient velocity to jet velocity.

4.6.3. Flow Visualization Techniques

To enhance the visualization of the flow patterns, 0.04 gram of Rhodamine 6G dye was added to the source discharge tank containing warm water. This dye serves as a tracer, emitting a longer wavelength of incident light to improve visibility. A diode-pumped solid-state (DPSS) continuous-wave green laser with an output power of 10 W and wavelength of 532 nm was employed to induce fluorescence in the dye throughout a horizontal laser sheet (Figure 4b). The flow dynamics and interactions within the confluence flow were captured using a high-speed charge-coupled (CCD) camera positioned above the flume (Figure 4b). Operating at 100 frames per second, this camera ensured that consecutive frames were uncorrelated, offering a comprehensive view of the flow fields. The camera boasted a resolution of 2336 × 1728 pixels and provided detailed, high-quality imagery. A C-mount 12 mm lens with an f/1.4 aperture was employed to increase the coverage area. Continuous acquisition was maintained, and the exposure time was set to 1/4000 for effective capture of the dynamic behavior of the thermal jets. The captured images were stored with a Mono8 bit resolution, utilizing 256 grayscale levels. This setup enhanced the quality and contrast of the obtained images, ensuring accurate and detailed visualization of the flow phenomena. The camera was connected to a computer through a PCI frame grabber facilitated by two attached camera-link cables. This connection allows for efficient data transfer and real-time monitoring of the flow dynamics. Figure 35 shows a raw image captured by the camera. This configuration rendered the jet flow bright against a dark background, with each pixel's light intensity level ranging from pure black to pure white. Thus, recorded images provided a detailed representation of the flow characteristics. The concentration of the tracer dye was linearly correlated with the light intensity [125], facilitating quantitative analysis of the thermal jet concentration within the flow. Pure white was associated with the initial concentration (C_o), and pure black with zero concentration.

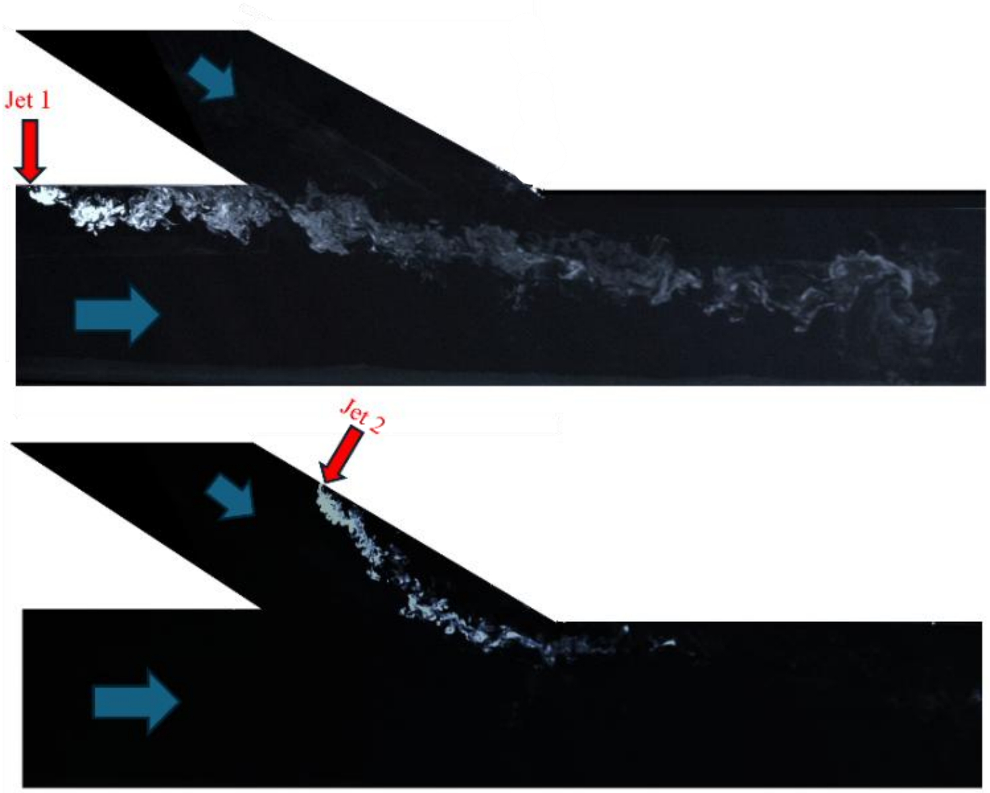

Figure 35. raw image captured by the camera.

4.6.4. Processing and Data Analysis

Before initiating the jet discharge, a preliminary set of approximately 100 images capturing only the background, devoid of Buoyant Jets, was recorded and time averaged. This process aims to eliminate extraneous light sources unrelated to the jet fluid concentration. Upon achieving steady flow conditions, a series of 3,000 images was recorded, encompassing the jet discharge phase. Subsequently, the background image was subtracted from the images containing the jet to eliminate background light interference.

The post-processing of the captured images was conducted using MATLAB code tailored to the experimental requirements. This code analyzes grayscale images pixel-by-pixel to determine tracer concentrations and subsequently converts them into color-coded representations. A statistical analysis, including time-averaged images and their variance, was performed by analyzing consecutive frames. After this analysis, the concentration distribution fields and contours were generated based on the nondimensionalized C/C_0 parameter, where C_0 represents the initial discharge concentration. These visualizations elucidate the degree of mean concentration reduction, providing insights into the dilution level compared to the initial concentration.

Visualizing intricate flow patterns within a flume is a critical aspect of this study. To determine the dilution levels, the experimental setup incorporated a horizontal laser sheet positioned at the nozzle level. The image processing procedure illustrated in Figure 34b elucidates the precise location of the trajectory and facilitated a comprehensive analysis of dilution within the confluence flow. This approach provided insight into the dispersion characteristics of thermal jet discharge under varying conditions.

Sequentially altering the vertical position of the laser sheet emission across the flume width allowed for the creation of eight distinct slices, each spaced approximately 25 mm apart. These slices provided a detailed cross-sectional view of the flow dynamics. The captured frames from these slices were subsequently compiled using ParaView visualization software tools, enabling the generation of both 2D and 3D representations of the mean flow fields.

4.7. Results and Discussion

4.7.1. General Observations

4.7.1.1. Instantaneous Visualization

Figure 36 provides detailed visualizations of the instantaneous concentration flow fields for two experimental cases, R3 and R4, which differ in their discharge locations, allowing us to compare the impacts on jet flow in the confluence channels.

In Case R3, the jet reached the confluence and encountered the shear layer, which pushed it away from the inner bank. This deviation alters the trajectory, enhancing its mixing efficiency with the ambient flow. The broader exposure of the jet to the surrounding fluid allows for a dynamic interaction between the jet momentum and varying velocities at the confluence. The presence of rotating tracer bundles, marked by blue rectangles, indicates the active mixing and redistribution of fluid properties, contributing to a diversified flow pattern. This scenario underscores the beneficial effects of strategic jet placement in promoting effective mixing within a channel. Conversely, Case R4 presents a scenario in which the jet is discharged into a narrower section of the channel closer to the inner bank. This proximity causes part of the jet to be trapped in a separation zone, thereby limiting its initial mixing. However, as the jet progresses into the recovery zone, it begins to spread more evenly across the channel width. Despite the delayed start, the jet in R4 eventually achieves a broad distribution of fluid, though the initial confinement affects the efficiency and pattern of mixing.

A comparison of Cases R3 and R4 highlights the profound impact of discharge locations on fluid dynamics within the confluence channels. In Case R3, the jet is effectively pushed away from the inner bank, thereby facilitating early and efficient mixing. This is attributed to the increased interaction with the surrounding fluid dynamics, which promotes the development of Kelvin-Helmholtz instabilities and enhances the mixing process. In contrast, the positioning in Case R4 restricts the initial spread of the jet, leading to a more confined flow pattern that only begins to disperse upon reaching a recovery zone.

These observations emphasize the critical role of the discharge location in influencing the development of flow instabilities and the overall effectiveness of mixing processes in confluence channels. Understanding these dynamics is essential for optimizing fluid mixing and management strategies for engineering and environmental applications.

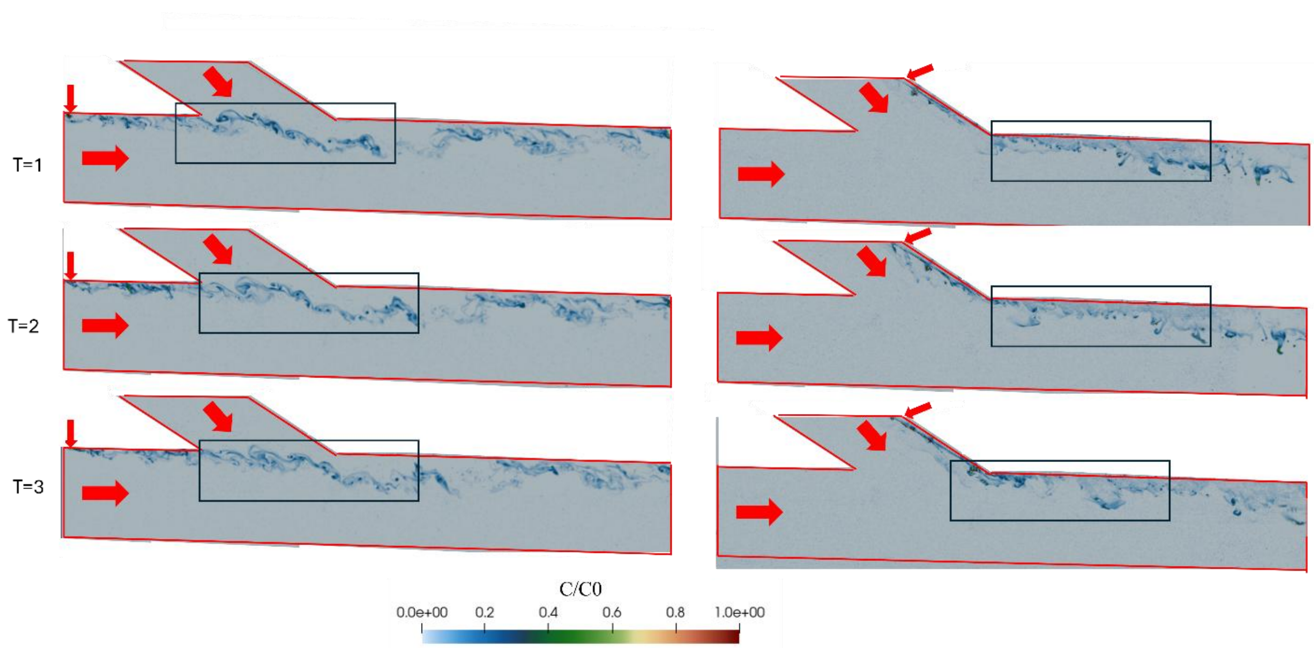

Figure 36. Instantaneous concentration flow fields for case R3 (left) & R4 (right). T=1 marks the moment when KH is created, T=2 is 0.1 seconds after T=1, and T=3 is 0.2 seconds after T=1.

4.7.2. Timed-averaged Visualization

The time-averaged flow depictions of the jets were visualized using the ParaView software tool, as illustrated in Figure 37. When the jet is introduced into the main channel, it initially travels close to the channel wall until it reaches the junction. At this point, the jet encounters the shear layer created by the confluence, which pushes it away from the wall. As the jet progresses into the recovery zone, it is redirected back towards the wall, resuming its movement near the channel boundary.

In the tributary channel discharge scenario, the movement of the jet mimics some aspects of its behavior in the main channel, but within a more confined space. Initially, the jet travels close to the channel wall. Upon reaching the junction, it encounters the confluence shear layer, which compels the jet to remain near the wall but with a narrower width than the main channel discharge case. Additionally, a part of the jet becomes trapped in the separation zone at this point, which restricts its initial ability to mix with the surrounding water.

Cases R3 and R4 represent specific instances within a broader array of scenarios explored in this study. Although these cases provide insights into the spatial dynamics and immediate effects of jet behavior in confluence channels, they serve as a preliminary focus. The subsequent sections of this paper delve into additional variables that significantly influence jet dynamics, such as temperature and velocity. The effects of these factors on jet penetration and overall fluid interaction within different the confluence zone are thoroughly discussed.

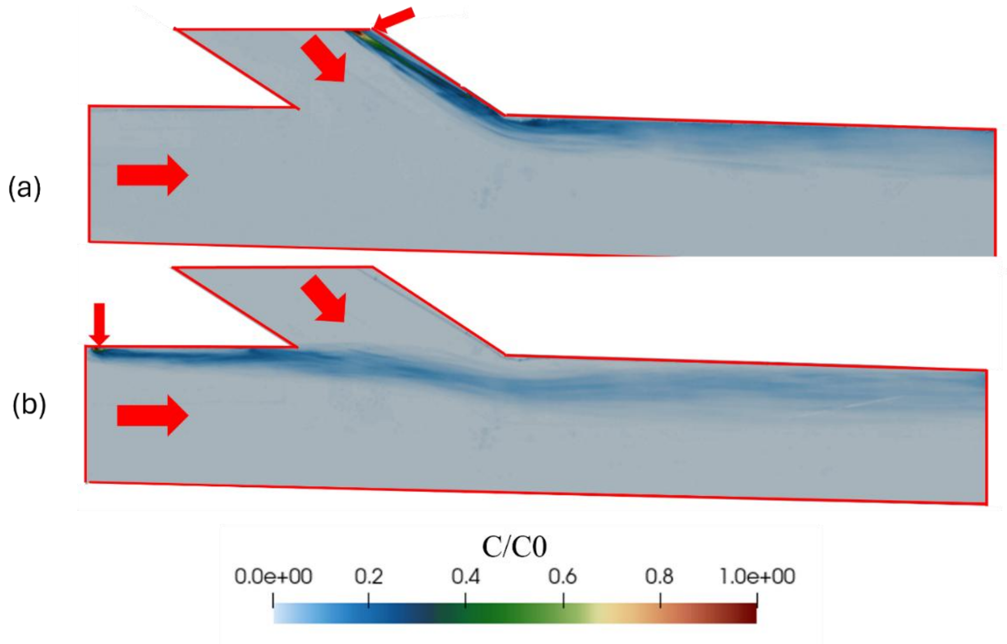

Figure 37. Time-averaged concentration contours (a) Jet in main channel (case R3) (b) Jet in tributary (case R4).

4.7.3. Visualization of the Case of Stagnant Flow Conditions in the Tributary Channel

This section explores the dynamics of a jet when introduced into a channel system in which one part, the tributary, is under stagnant flow conditions. Under these conditions, the behavior of the jet can vary significantly depending on its point of release, either into the main channel or directly into the tributary. By investigating these scenarios, we aim to understand the fluid mechanics and flow behaviors that emerge when a moving jet encounters a stagnant tributary (or a large embayment), thereby providing insights into the complexities of fluid dynamics in engineered and natural waterways. The following analysis details how the jet behaves in each scenario, as illustrated in Figure 38, and discusses the implications of these behaviors for fluid mixing and channel flow management.

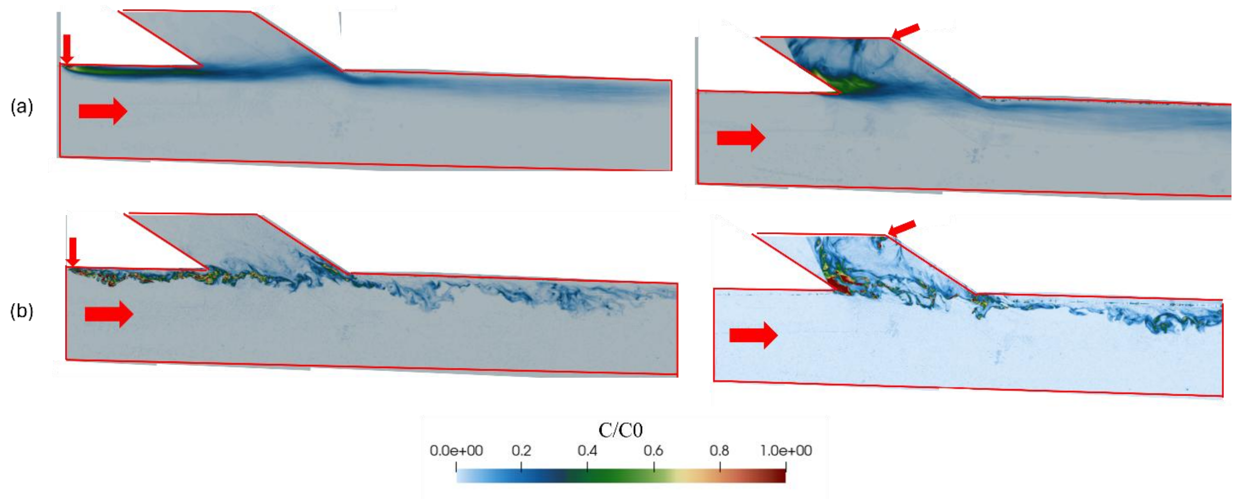

Figure 38. Visualization of the cases of stagnant flow conditions in the tributary channel for case R9 (left) and case R10 (right). (a) is time-averaged and (b) is instantaneous.

When the jet is released into the main channel under conditions where the tributary channel is stagnant, the jet behaves similarly to its behavior in a simple, unobstructed channel. However, a portion of the jet diverges into the tributary channel. This diversion occurs primarily due to the formation of a shear layer between the main flow and the stagnant zone. This shear layer creates instabilities and turbulence, which enhance mixing and facilitate the penetration of the jet into the stagnant zone. The absence of opposing flow in the tributary further reduces hydrodynamic resistance, allowing part of the jet to "spill" into the tributary. This phenomenon can be visualized as the jet exploiting the path of least resistance, where stagnant water does not provide the usual dynamic pressure or velocity profiles that would otherwise influence and restrict the flow direction.

In the second scenario, where the jet is released directly into the stagnant tributary, a shear layer forms at the junction between the tributary and main channel. This shear layer is crucial because it acts as a dynamic boundary that governs flow characteristics. The presence of the shear layer at the junction results in the jet being initially confined within the tributary due to the differences in velocity and momentum between the jet and stagnant flow conditions. Over time, the jet gradually penetrated into this shear layer, slowly diffusing and releasing into the main channel. This slower release is characterized by the gradual mixing of the jet with the main channel's flow, The shear-induced turbulence at the junction enhances mixing and facilitates the transition into broader channel dynamics. This phenomenon of shear-induced turbulence and enhanced mixing also occurs when the jet is discharged into the main channel, highlighting the critical role of shear layers in influencing fluid dynamics and mixing efficiency in both scenarios.

4.8. Jet Trajectory

4.8.1. Jet-1 Trajectory

The trajectory of a jet can be described as the path along which the concentration is the highest [126]. For non-dimensionalization, the jet diameter was used as the length scale, and the mixing behavior was analyzed up to the distance of 200 jet diameters downstream. Figure 39 illustrates the paths of the surface jets within the channel at the confluence. It is evident that the trajectories are influenced by the Froude number (Fr), which varied across different scenarios. This variation suggests that the dynamic interplay between the buoyancy of the flow and the channel geometry shapes the jet behavior. Notably, the figures reveal a slight difference in the trajectory between positive and neutral jets when released at the surface. This divergence is primarily due to buoyancy differences. Positive jets, which are lighter than the ambient fluid, tend to rise due to the buoyant forces. Because they are released near the surface, the surface acts as a symmetry plane and further influences their upward movement. Conversely, neutral jets, which are buoyancy-neutral relative to the surrounding fluid, follow a more level trajectory, influenced not by buoyancy but by the prevailing flow dynamics within the channel. This leads to observed variations in how each jet navigates the confluence zone, reflecting the subtle yet substantial impact of buoyancy on jet behavior. Additionally, R1 and R5 have bigger velocities compared to R3 and R7, further affecting the trajectory and dynamics of the jets in the channel.

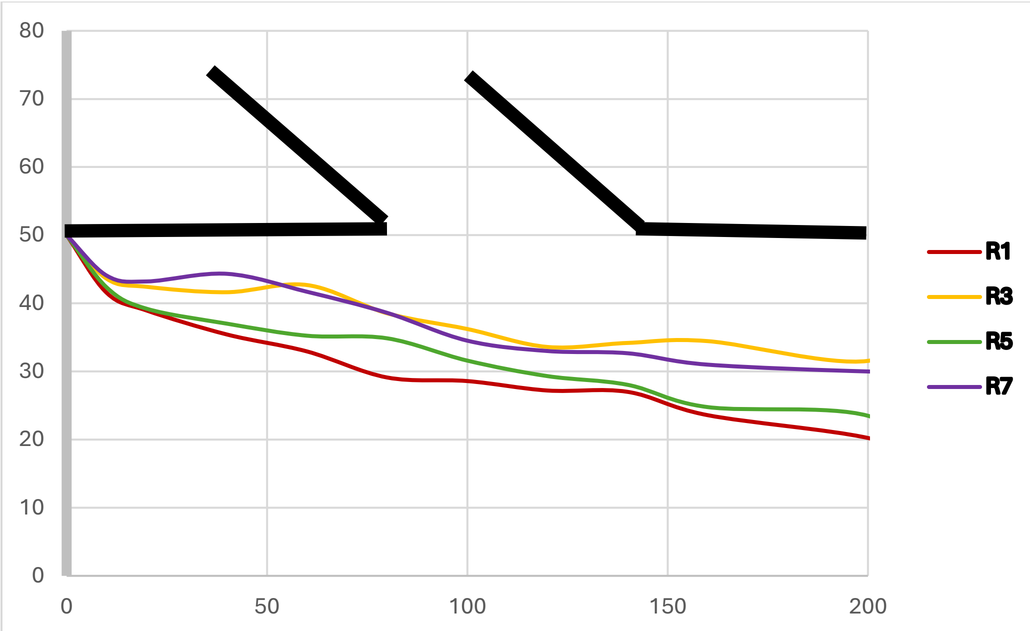

Figure 39. Trajectories of the Jet-1 test cases

4.8.2. Jet-2 Trajectory

Figure 40 depicts the trajectory of jet-2 within the tributary channel under various scenarios. It is evident from this figure that the jet is constrained by the shear layer of the channel, preventing it from spreading across the channel width. Consequently, the jet follows a path of limited width, remaining close to the inner bank of the channel. The same situation occurs for either positive or neutral jets released into the tributary. Positive jets, although lighter and typically rising above the surrounding fluid, find their upward movement blocked by their release near the surface. This confinement near the surface restricts their ability to rise, causing them to exhibit behavior similar to that of neutral jets under these specific conditions. Both types of jets, despite their inherent differences in buoyancy, are influenced significantly by the shear layer and proximity to the surface, which together dictate a similar trajectory along a narrow path within the tributary channel.

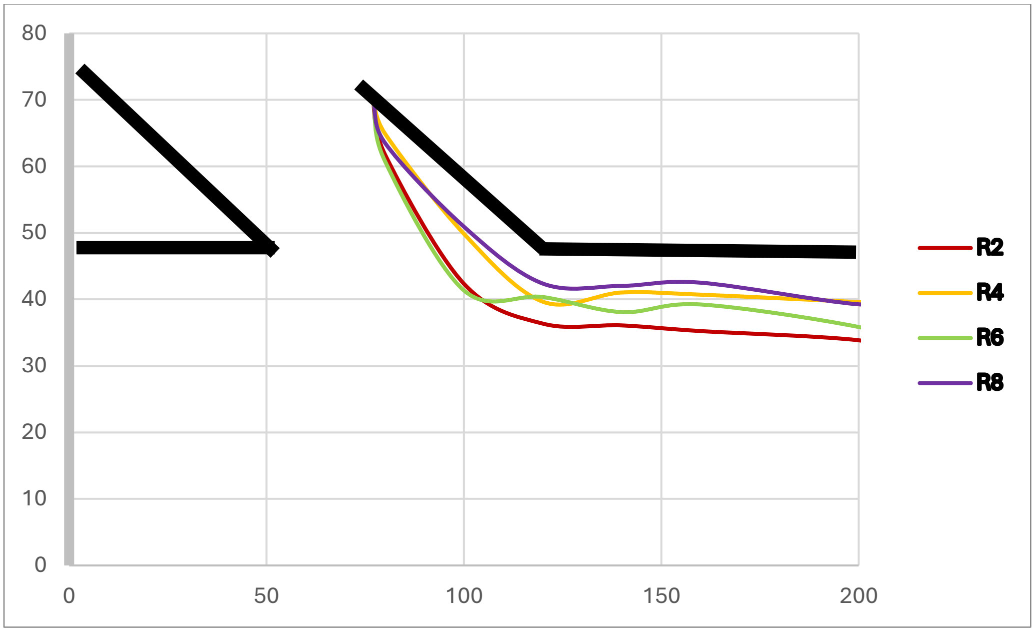

Figure 40. Trajectories of the Jet-2 test cases

4.8.3. Jet Trajectory in the Case of Stagnant Flow Conditions in the Tributary Channel

Figure 41 illustrates the trajectory of the jets when the discharge from the tributary is zero. A key observation from the R10 experiment is that, because of the shear layer of the main channel, the discharge becomes temporarily trapped within the tributary. As the jet concentration increases, it begins to release from upstream of the tributary into the main channel at the point known as the stagnation zone. In addition, when the jet is released from the main channel in this situation, it moves near the inner bank and behaves similarly to a jet in a simple channel. This positioning near the inner bank reflects a typical jet trajectory in less complex channel configurations, highlighting how the dynamics of the main channel continue to influence the jet behavior even in the absence of active discharge from the tributary.

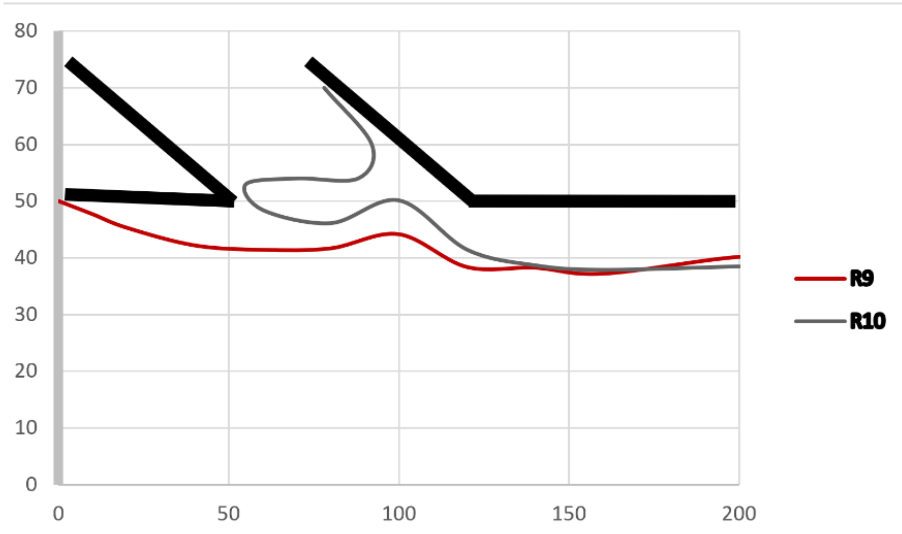

Figure 41. Trajectories of the Jets with zero discharge of the tributary

4.9.Cross-sectional Distributions and Jet Widening

Analyzing the expansion of the jet along its path provides valuable insights into the development of the jet and emphasizes the influence of both the discharge rate and placement of the discharge on the effectiveness of mixing and dilution. This section provides a better understanding of how these factors contribute to the overall performance of the jet in terms of enhancing the fluid integration and reducing the concentration gradients within the flow. By examining the growth of the jet and its interaction with the surrounding fluids, one can better comprehend the mechanisms that drive its integration and dispersion.

The normalized concentration profiles across various downstream cross-sections perpendicular to the central trajectory of the jet are depicted in Figure 42 considering different discharge ratios and densities. The parameter "b_c" denotes the distance from the jet centerline to the point where the concentration falls to $e^{-1}C_{max}$, with C_{max} representing the peak tracer concentration along the centerline. Analysis of these profiles enables comparison of the expansion of each jet at consistent cross-sectional points, demonstrating how variations in jet velocity and location affect the jet widening. Notably, a jet with the same velocity, when released in the main channel, exhibits a wider spread than a jet in the tributary (compare R1 versus R2, and R3 versus R4). This difference is primarily because the jet in the tributary is constrained by the shear layer, limiting its widening compared to the jet in the main channel. Furthermore, jets released from the same location but at different velocities demonstrate that a jet with higher velocity is wider than one with lower velocity (compare R1 versus R3, and R2 versus R4). This widening disparity can be attributed to the higher initial momentum of the faster jet. Additionally, in all cases, particularly near the jet nozzle, the widening of the half of the jet closest to the inner wall is less than the other half due to the wall's restrictive influence on the fluid flow.

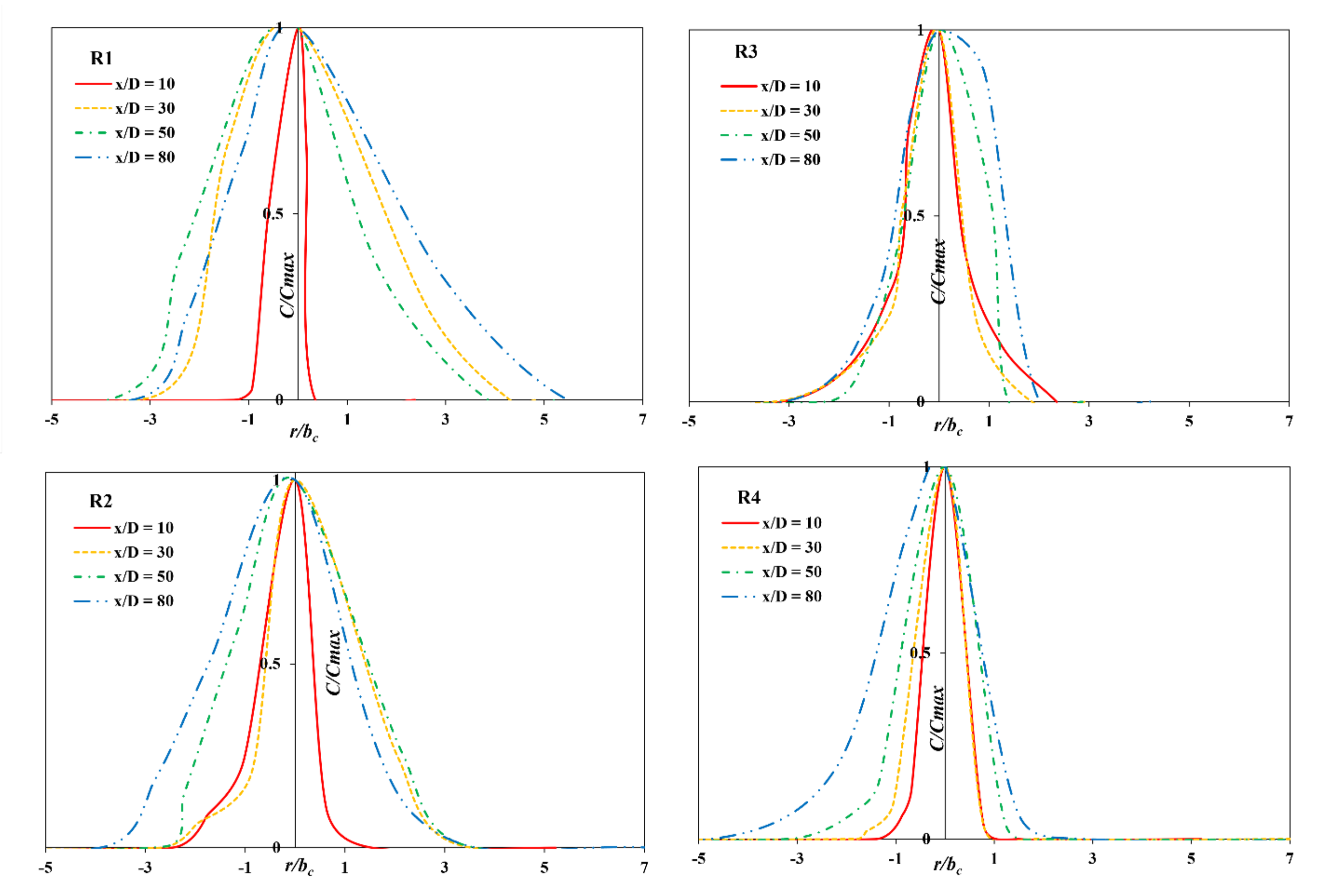

Figure 42. Jet widening profiles (r=-5 is outer bank)

Figure 43 shows the jet widening at 2.5 cm below the surface for two tests: one with a positively buoyant jet (R1) and one with a neutral jet. Comparing the figures indicates that the neutral jet has a wider distribution at this level.

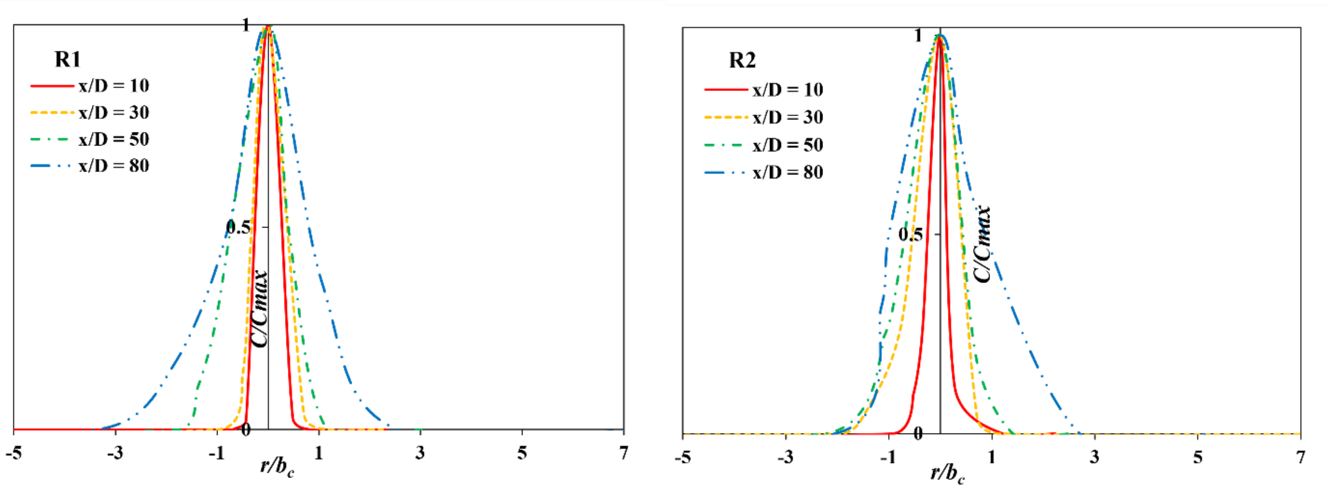

Figure 43. Jet widening profiles at 2.5cm below the surface

4.10. Variance of Concentration

The investigation of concentration fluctuations facilitates a deeper understanding of the differential mixing dynamics occurring at the interface regions between the injected jet and ambient flow. The quantification of these fluctuations is expressed through the non-dimensional variance of concentrations, denoted as σ^2/C_{max}^2, where σ represents the standard deviation of the concentration values. This variance metric is systematically evaluated at several downstream cross-sections orthogonal to the central trajectory of the jet, as demonstrated for experimental cases R1 and R3 in Figure 44. This analysis not only provides insights into the spatial distribution and intensity of mixing of the jet as it interacts with the confluence flow at various distances from the point of discharge but also underscores the variability of mixing efficiency dependent on the initial conditions and configuration of the jet.

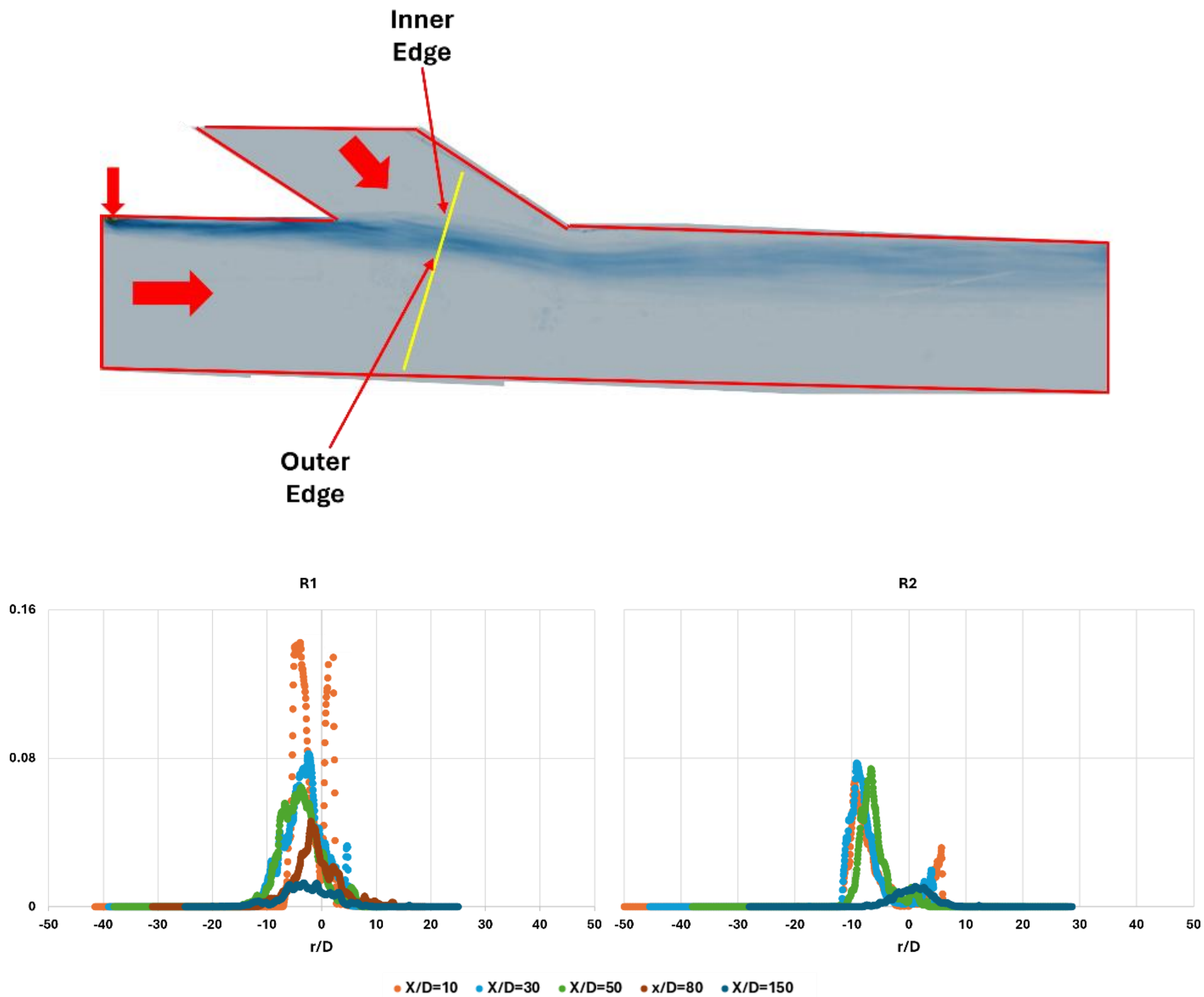

Figure 44.Concentration variance profiles, between the inner and outer edges, at different downstream cross-sections orthogonal to the central jet trajectory, for cases R1 and R2.

According to the findings, the variance profiles exhibit a bimodal distribution with a notable minimum along the jet centerline, indicating reduced mixing within the jet core itself. In contrast, dual peaks in the variance profiles are prominent, located at both the inner and outer edges of the jet's shear trajectory. Notably, the peak at the outer edge consistently surpasses that at the inner edge across all cases examined. This asymmetry is primarily attributed to the formation and subsequent disruption of Kelvin-Helmholtz (KH) instability structures, as documented in references [126,127].These instabilities play a pivotal role in enhancing turbulent mixing, particularly at the upper edge, where the differential velocity between the jet and the ambient fluid maximizes shear, thereby intensifying the mixing processes. As the trajectory progresses, the bimodal distribution of the variance profiles gradually smoothens and eventually converges into a single line. This transition indicates an increasing uniformity in mixing along the jet's path, as initial variations in concentration diminish and the fluid elements from the jet and ambient flow become more homogeneously mixed. This phenomenon typically results from the enhanced turbulence and diffusive processes that effectively redistribute the momentum and mass as the flow moves downstream. Moreover, comparisons of the variance profiles across different scenarios reveal that the variance levels are consistently lower when the jet is positioned in the main channel. This is because, when the jet is in the main channel, it can distribute over a wider width, allowing it to dilute better. This is consistent with the results of the widening and concentration distribution presented above.

As highlighted in the introduction, several confluence features significantly influence the mixing dynamics. These include the angle between the converging channels and flow ratios of the approaching streams. In our analysis, we focused on specific instances involving one angle and one flow ratio. However, it is important to note that variations in these factors can dramatically alter the jet behavior. For instance, increases in the confluence angle can enlarge the separation zone, trapping more of the discharge within it, particularly when the jet is discharged in the tributary channel. Similarly, an increase in the velocity of the tributary flow tends to push the shear layer towards the outer bank, compelling the jet in the main channel to navigate through a narrower width while increasing the turbulence in the shear layer.

Further complexities arise when considering additional scenarios that can affect jet mixing. These might include differences in channel depth, physical properties of the fluids involved, and environmental variables such as temperature gradients. Each of these factors can potentially alter flow dynamics and mixing efficiency in diverse ways. A comprehensive examination of these scenarios will provide deeper insights into the interplay between confluence features and their cumulative effects on jet behavior and fluid mixing in hydraulic systems, which is beyond the scope of this paper.

4.11. Conclusions

For the effective management of effluent discharges in river confluences, it is paramount to comprehend the factors influencing jet dynamics and mixing processes. This study explored the combined effects of varying the discharge velocities, buoyancy, and confluence geometries on the performance of surface jets. Through a series of Laser-Induced Fluorescence (LIF) experimental tests, the trajectories and concentration distributions of jets in complex flow environments were examined. The experiments focused on different scenarios in which confluence discharge and ambient flow conditions were systematically varied to assess their impact on jet behavior and mixing efficacy.

Instantaneous and time-averaged flow visualizations captured via LIF experimentation revealed various parameters such as jet trajectory, spread, and dilution rates. The results demonstrated that both the jet trajectory and dilution were influenced by the discharge rate and buoyancy, with increased velocity and buoyancy leading to enhanced mixing and a wider dispersion of the jet.

The study further highlighted that higher ambient flow velocities relative to jet speed (characterized by the parameter u_r) resulted in more dynamic interactions between the jet and ambient water, promoting greater entrainment and dilution. This was particularly evident in scenarios where the jet was discharged into the main channel, showing deviations in the jet trajectory and an increased dilution effect compared with jets in tributary channels.

In conclusion, this research provides substantial evidence that the design and placement of effluent discharges can be optimized by considering the detailed dynamics of jet behavior in confluence regions. These findings offer valuable management for environmental practices, suggesting that strategic positioning and orientation of discharges can significantly enhance the mixing and dilution of effluents, thereby minimizing their ecological impact. The insights gained from this study are not only applicable to the design of new discharge systems, but also to the improvement of existing installations in urban and industrial landscapes. Future work will aim to integrate these findings into computational models to further refine the predictions and enhance the design of effluent management systems in complex riverine environments.

5. Numerical simulation of surface positive jet in confluence flow

5.1. Abstract

This study conducts a numerical investigation of effluent discharge in river confluences, focusing on jet behavior under various hydrodynamic conditions. Aquatic ecosystems are frequently used as receiving environments for wastewater discharges, which can lead to complex phenomena impacting the ecosystem. To mitigate and manage these adverse effects, a thorough understanding of the interactions between effluents and receiving environments is crucial for promoting sound environmental management practices. To this end, the current study investigates the behavior of a warm jet in crossflow when released near the surface at the confluence of channels. This paper specifically examines how discharge location and velocity affect the jet's trajectory, dilution, and mixing efficiency. Using OpenFOAM for numerical simulations, we analyzed jets introduced into both the main and tributary channels, with a focus on different discharge velocities, particularly low-velocity discharges (Fr near one), which remain underexplored in the existing literature. Using the Large Eddy Simulation (LES) turbulence model, the numerical results showed strong agreement with experimental data, with an average error of approximately 4%, validating the model's accuracy. Key findings reveal that the confluence shear layer plays a significant role in shaping jet trajectories and enhancing mixing efficiency. Jets discharged in the main channel exhibited longer trajectories and greater interaction with ambient flow, resulting in higher dilution rates for both low- and high-velocity jets. Low-velocity jets were found to behave independently of jet velocity upon reaching the confluence, with their path being altered by the shear layer. Conversely, jets released in the tributary maintained a more consistent trajectory, unaffected by confluence dynamics.

Keywords: fluid mechanics, LES, rigid lid, confluence, OPENFOAM, surface positive jet

5.2. Introduction

Water quality standards have imposed restrictions on the release of pollutants generated by various industrial processes. Examples include discharge from desalination units, sewage, and waste heat into rivers or oceans. To address these pollution challenges, a thorough understanding of the detailed features of turbulent dispersion and efficient mixing of waste effluent with the ambient environment is essential. These discharges can occur horizontally, vertically, or at an angle, into either stagnant or flowing environments. When jets are released into the main stream, this scenario is referred to as a "jet in crossflow" [128].

Many researchers have investigated the complexity of jets in crossflow [129–131]. However, this complexity can be further intensified when jets are released in areas with intricate river geometries, such as confluence regions, as studied by Behzad et al., (2024) [132]. To the best of the authors' knowledge, no numerical investigations have focused on the mixing of jets in confluence zones, particularly for low-velocity discharges (Froude number near one). This study aims to assess the accuracy of CFD simulations for surface positively buoyant effluent discharges in confluence areas and evaluate the impact of the junction on the outfall. Additionally, it seeks to extend previous experimental investigations by exploring different discharge flow rates and confluence flow rate ratios.

5.3. Jet in crossflow

A jet in crossflow occurs when a jet of fluid enters and interacts with a crossflowing fluid. Andreopoulos and Rodi (1984) [133] observed that both the jet and the crossflow are deflected during this interaction. The crossflow bends the jet, while the crossflow itself is diverted as it encounters the jet, which behaves like a rigid obstacle when the jet momentum is sufficiently high. This interaction causes the jet to mix with and entrain fluid from the deflected flow. When the ratio of jet velocity to ambient velocity is high, the jet is slightly affected near the exit and penetrates further into the crossflow before curving [134].

Pathak et al. (2006) [135] identified four main vortical structures that characterize the flow field of a jet in crossflow: (i) shear layer vortices, which form at the interface between the jet and the crossflow and are associated with Kelvin-Helmholtz instabilities; (ii) horseshoe vortices, caused by the adverse pressure gradient upstream of the jet; (iii) wake vortices, which develop within the inner part of the jet; and (iv) counter-rotating vortex pairs (CRVP), which form in the cross plane just after the jet exit and become dominant structures further downstream

The phenomenon of jets in crossflow has been explored extensively through both experimental and numerical methods over the years [56,132,136]. A comprehensive review of these experimental and numerical investigations on the topic, covering recent decades, is provided by Taherian and Mohammadian (2021) [61].

Effluent discharges that are less dense than the receiving fluid are common in both natural and engineered systems. A typical example is the release of warm water from power plant cooling towers into rivers, often as a surface discharge due to its cost-effectiveness. However, surface discharges generally carry higher environmental risks compared to submerged alternatives [7].

The jet trajectory is determined by connecting points with the highest time-averaged concentration at each cross-section (Figure 45). The angle θ represents the jet's inclination, indicating the direction of instantaneous velocity along the central axis relative to the crossflow. θ_0 refers to the initial angle, while θ represents the angles along the jet's trajectory [132].

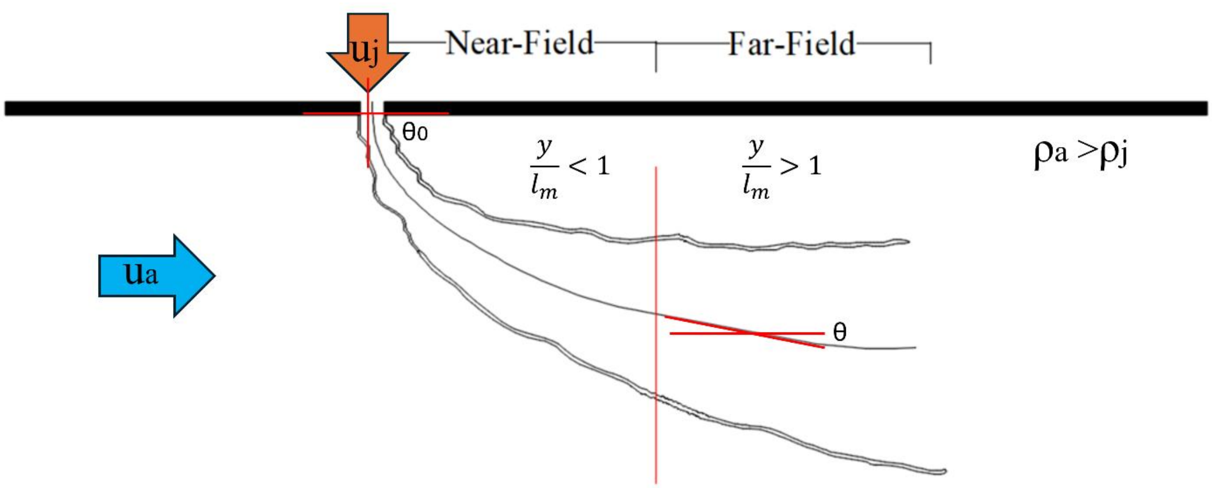

Figure 45. Schematic shape of the surface jet in crossflow (Top View). Terms are defined in the text.

One of the pioneering studies on jets was conducted by Pratte and Baines [137], who examined jet trajectories for various jet-to-crossflow velocity ratios. Additionally, early work on predicting surface discharge behavior through mathematical modeling was done by Dunn et al. [138] and McGuirk and Rodi [59,139]. These efforts were aimed at understanding the characteristics of discharges in both stagnant and crossflow conditions.

Jirka et al. (1981) [60] were the first to introduce length-scale parameters for classifying buoyant surface jets. Subsequently, Chu and Jirka (1986) [63] provided an initial framework for classifying buoyant surface jets in crossflows. Building on this foundation, Jones et al. (1989) [7] developed a more comprehensive classification system, categorizing surface jets based on the following dimensionless parameters:

$$L_Q = Q_0/M_0^{1/2} \tag{29}$$

$$L_M = M_0^{3/4}/J_0^{1/2} \tag{30}$$

$$l_m = M_0^{1/2}/\overline{u_a} \tag{31}$$

$$l_b = J_0/\overline{u_a}^3 \tag{32}$$

With

$$Q_0 = \overline{u_0} a_0$$

$$M_0 = \overline{u_0} Q_0$$

$$J_0 = Q_0\, g_0'$$

$$g_0' = g(\Delta\rho_0/\rho_0)$$

The terms are defined as follows: L_Q represent Discharge length scale, L_M denotes Jet-to-plume length scale, l_m is Jet-to-crossflow length scale, and l_b signifies Plume-to-crossflow length scale.

where Q_0 is the jet flow rate, M_0 is the jet momentum flux, J_0 is the jet buoyancy flux, a_0 represents the cross-sectional area of the jet, g is the gravitational acceleration, ρ is the water density, and $\Delta\rho_0$ is the difference in the discharge density ($\Delta\rho_0 = \rho_a - \rho_0$).

A surface buoyant jet in crossflow can be divided into four distinct asymptotic regimes depending on whether buoyancy, momentum, or crossflow predominantly affects the jet's mixing characteristics (Figure 1) [61]:

- Momentum Dominated Near-Field ($y/l_m << 1$): the jet's behavior is primarily controlled by its initial momentum.
- Momentum Dominated Far-Field ($y/l_m >> 1$): its discharge becomes strongly influenced by the crossflow.
- Buoyancy Dominated Near-Field ($y/l_b << 1$): the plume's motion is mainly driven by its initial buoyancy.

Buoyancy Dominated Far-Field ($y/l_b >> 1$): the plume's discharge is largely governed by the effects of the crossflow. In this context, y denotes the cross-channel distance. (Figure 1).

This study specifically investigated the Momentum-Dominated Near-Field and the Buoyancy-Dominated Far-Field regimes.

In a recent study, Gharavi et al. (2020) [108] utilized experimental techniques to deepen the understanding of the three-dimensional velocity field of surface buoyant jets in crossflow environments. Using Stereoscopic Particle Image Velocimetry (Stereo-PIV), they captured both spatial and temporal velocity distributions downstream of the jet discharge point. Their findings revealed the formation and development of vortices within the jet's flow structure, resembling half of the counter-rotating vortex pairs (CVPs) typically observed in submerged jets. This asymmetry was attributed to the interaction with the water surface, which acted as a plane of symmetry, suppressing one of the vortices. Key flow characteristics such as turbulent kinetic energy were measured and dissipation rate was calculated, providing insights into the complex mixing mechanisms at play in surface jets.

Behzad et al. (2024) [132] expanded upon this research by utilizing Laser-Induced Fluorescence (LIF) to obtain the first measurements of effluent discharges at channel confluences. Their systematic investigations focused on the dynamics of positively buoyant surface jets, employing experimental techniques to study the complex behavior of jets entering confluence zones under various hydrodynamic conditions. The study demonstrated that jet trajectories are influenced by both the discharge location and the confluence flow ratio.

5.4. Open Channel Confluence

The convergence of two open channels is common in natural river systems as well as in various hydraulic structures such as wastewater treatment plants and fish passage systems [140]. This confluence triggers mass and momentum transfer across the mixing layer between the two streams, significantly affecting the temporal and spatial distribution of pollutants within the rivers [78]. The flow behavior near a confluence is complex and is influenced by factors such as the free surface, upstream conditions in both the main and branch channels, and formation of a separation zone downstream of the confluence [3].

River channel confluence flow dynamics have been examined and are typically divided into six key regions: flow stagnation, deflection, separation, maximum velocity, recovery, and distinct shear layers (Figure 46) [41]. The location and size of these zones are determined by the ratio of the discharge between the two incoming streams and the angle of the river confluence [8].

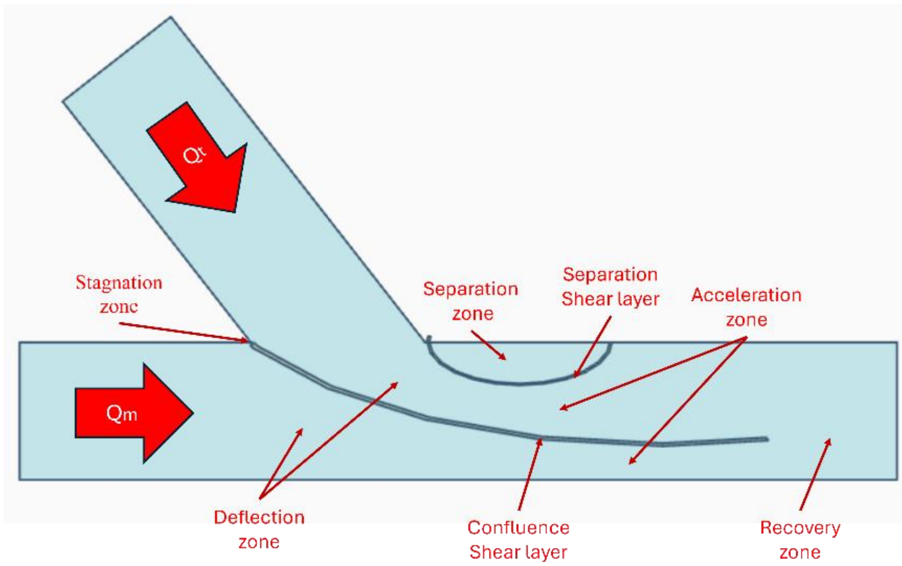

Figure 46. Flow characteristics in channel confluences (based on Best, 1987 [41])

Due to advancements in measuring devices and computer technology, it is now feasible to accurately capture and describe the three-dimensional flow structure, material transport, bed changes, and biological and environmental impacts of river confluences [64]. As a result, recent years have witnessed an increase in research on river confluences [16,142,143].

The flow dynamics, turbulent coherent structures, and turbulence characteristics at confluences have been extensively studied [65,144]. Field investigation conducted by Roy and Bergeron (1990) [145] highlighted the occurrence of flow separation zones and recirculation at downstream confluence corners in nature. Ashmore et al. (1992) [26] measured the flow field at a natural confluence, finding that flow velocity accelerates sharply at the confluence junction, with two separate high-velocity cores merging into a single core at the channel center. De Serres et al. (1999) [31] conducted a three-dimensional analysis of flow structures in river confluences, identifying mixing layers, stagnation zones, separation zones, and recovery zones.

Numerical studies, such as that of Sharifipour et al. (2015) [146], investigated the flow structure in a 90° confluence, finding that the size of the separation zone decreases as the width ratio between the tributary and the main channel increases. Behzad et al. (2024) explored the fluid dynamics of open channel confluences, focusing on the impact of bed deformation, which is often overlooked in past studies. Using OpenFOAM, they simulated flow with both flat and degraded beds, applying six turbulence models, including RANS, LES, and DES, and used rigid lid and VoF methods. LES performed best, with a 3% normalized mean square error (NRMSE) under VoF and 17% under the rigid lid. Their findings revealed that the recirculation zone was shorter or absent near the bed in degraded cases, altering secondary flow patterns. Additionally, vortical structures and circulation within the separation zone were strongly influenced by bed shape and channel geometry.

5.5. Objective

Physical models, despite their widespread use, are often limited by scale effects, while field studies tend to be labor- and time-intensive, with results heavily dependent on the precision of measurement techniques. As a result, numerical simulations offer a cost-effective alternative for investigating complex flow phenomena [64]. Despite numerous studies on confluence channels and jets in crossflow, a significant gap remains in the literature, in that the interaction between these two complex flow fields has not been studied. To the best of the authors' knowledge, the only investigation into the dynamics of positively buoyant surface jets in confluence regions was recently conducted by the authors of this study [132], and no numerical analysis has been performed to date. Recognizing this research gap, the present study seeks to conduct a comprehensive LES investigation of surface crossflow jets advecting through a channel confluence. Additionally, this study aims to extend previous experimental results by simulating low velocity plume-like jets than could be achieved in the physical model. The primary goal is to understand the behavior and trajectory of pollutants released in confluence areas, providing insights for effective mitigation strategies and minimizing environmental impacts.

5.6.Numerical Methodology

5.6.1. Governing Equations

5.6.1.1. Large Eddy Simulation (LES) model

In this study, transport of momentum and mass is computed by the nondimensional incompressible Navier-Stokes equations coupled with an advection-diffusion equation for scalar transport. An implicit-filtering-based Large Eddy Simulation (LES) method was employed to directly resolve large-scale flow structures while filtering out the smaller scales. The coupling between momentum and buoyancy forces is modeled using the Boussinesq approximation, since the density difference between the dense jet and the ambient fluid is less than 10%. The governing equations are nondimensionalized and expressed as follows [147,148].

$$\frac{\partial \tilde{u}_i}{\partial \tilde{x}_i} = 0 \tag{33}$$

$$\frac{\partial \tilde{u}_i}{\partial \tilde{t}} + \frac{\partial \tilde{u}_i \tilde{u}_j}{\partial \tilde{x}_j} = -\frac{\partial \tilde{p}}{\partial \tilde{x}_i} + \frac{1}{\mathrm{Re}} \frac{\partial^2 \tilde{u}_i}{\partial \tilde{x}_j \partial \tilde{x}_j} - \frac{\partial \tilde{\tau}_{ij}}{\partial \tilde{x}_j} + e_i^g \frac{1}{\mathrm{Fr}^2} \tilde{c}, \tag{34}$$

$$\frac{\partial \tilde{c}}{\partial \tilde{t}} + \frac{\partial \tilde{u}_i \tilde{c}}{\partial \tilde{x}_i} = \frac{1}{\mathrm{ReSc}} \frac{\partial^2 \tilde{c}}{\partial \tilde{x}_i \partial \tilde{x}_i} - \frac{\partial \tilde{\tau}_i^c}{\partial \tilde{x}_i} z, \tag{35}$$

where indices $(i, j = 1, 2, 3)$ correspond to the spatial dimensions, $\tilde{u}_i$ shows the (i)-th component of the velocity, and $\tilde{p}$ represents the pressure. The kinematic viscosity is denoted by ν, $\tilde{t}$ is time and subgrid-scale (SGS) stress tensor is expressed as $(\tilde{\tau}_{ij})$. The gravitational acceleration acts in the direction of the unit vector $(e_i^g = (0, -1, 0))$, and $(\tilde{c})$ stands for the jet concentration. Throughout this study, variables with a tilde ($\tilde{}$) are dimensionless and filtered. Dimensionless variables are defined using characteristic scales of length, velocity, and time, as detailed in Table 9.

Table 9. dimensionless variables

Parameter	**Nondimensionalization**
Spatial coordinates	$\tilde{x}_i = x_i/d_0$
Velocity	$\tilde{u}_i = u_i/U_0$
Time	$\tilde{t} = (U_0/d_0)t$
Pressure	$\tilde{p} = (d_0/\rho_a U_0^2)p$
Salinity	$\tilde{c} = c/C_0$

The Wall-Adapting Local Eddy-viscosity (WALE) model is applied as the subgrid-scale (SGS) in this study and the stress tensor τ_{ij} is defined as:

$$\tau_{ij} = 2\nu S_{ij} + \tau_{ij}^{sgs} \quad (36)$$

S_{ij} represents the resolved velocity strain rate tensor, and the SGS stress tensor τ_{ij}^{sgs} is calculated as:

$$\overline{S_{ij}} = \frac{1}{2}\left(\frac{\partial \overline{u_i}}{\partial x_j} + \frac{\partial \overline{u_j}}{\partial x_i}\right) \quad (37)$$

$$\tau_{ij}^{sgs} = 2\nu_{sgs} S_{ij} + \frac{1}{3}\tau_{kk}^{sgs}\delta_{ij} \quad (38)$$

The eddy viscosity ν_{sgs} in the WALE model is calculated using:

$$\nu_{sgs} = (C_w \Delta)^2 \frac{\left(S_{ij}^d S_{ij}^d\right)^{3/2}}{\left(S_{ij} S_{ij}\right)^{5/2} + \left(S_{ij}^d S_{ij}^d\right)^{5/4}} \quad (39)$$

where C_w represents the model constant, Δ is the filter width, and S_{ij}^d denotes the deviatoric part of the strain rate tensor. For a comprehensive discussion of this formulation, please refer to Nicoud and Ducros, (1999) and Sagaut (2006) [148,149].

5.7.Numerical framework

This study utilized OpenFOAM (Open Field Operation and Manipulation), a widely recognized open-source CFD tool implemented in C++ and commonly used in hydraulic engineering [150,151]. Specifically, the PimpleFoam solver, a rigid lid model within OpenFOAM, was employed. An implicit Euler time scheme was used for temporal discretization, while spatial discretization involved Gauss linear schemes for gradient, divergence, interpolation, and wall distance calculations. The Gauss linear scheme was employed for solving the cell gradient. The numerical models were developed based on the configuration of the physical model described in the subsequent section [152].

In this study, snappyHexMesh was used to generate the mesh, as illustrated in Figure 47. The numerical domain was designed to match the physical dimensions of the experimental field. The grid size gradually increases outward from each boundary, ensuring a smooth grid transition, which is crucial for maintaining numerical stability. The meshes were graded to achieve higher resolution, specifically in the confluence zone

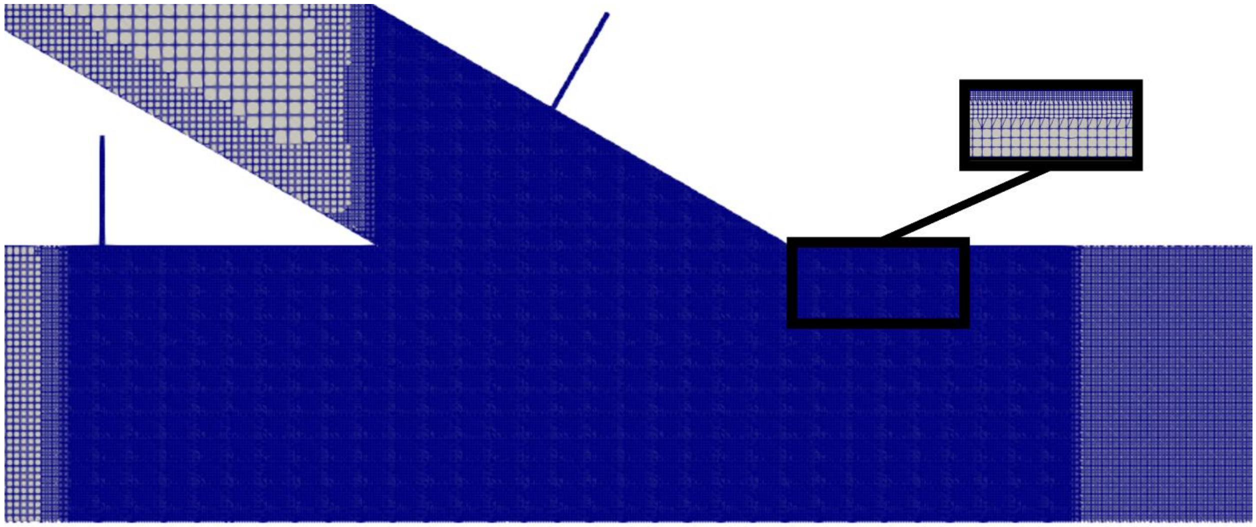

Figure 47. Mesh grids of the domain in the OpenFOAM platform were visualized on a scale of 1 to 5 to illustrate the distribution of the mesh grids.

5.7.1. Hydraulic conditions

A three-dimensional unstructured grid, shown in Figure 48, was set up for the computational analysis. A right-handed Cartesian coordinate system was used, with the x-axis increasing in the crossflow direction and the y-axis extending upward from the channel floor. The computational domain has physical dimensions of 10 cm in height, with the main channel width of 20 cm and the tributary channel width of 15 cm. This domain, modeled as a rectangular box, corresponds to a section of the recirculating water channel used in the experiments by Behzad et al, 2024 [132]. The experimental study evaluated two scenarios for surface thermal jet discharge: one with the jet released in the main upstream channel and the other in the tributary channel. The jet diameter was 4 mm, and the jet exit was located 20 cm upstream of the junction, near the water surface.

A grid clustering technique was applied near the jet inlet and wall surfaces to enhance resolution in critical areas [64]. As will be shown below, a TKE ratio test was conducted [128,153], indicating that a grid size of 8,140,198 tetrahedral cells provides satisfactory accuracy. During these tests, careful attention was given to maintaining the location of the first grid point near the wall, even as the total number of grid points was varied. The summary of the hydraulic and geometric data is presented in Table 10. That data has been used for model validation, ensuring that the numerical simulations accurately reflect the physical conditions of the experiments.

Table 10. Summary of the Hydraulic and Geometric Data [132]

Variable	Symbol (unit)	Value
Confluence junction angle	α (-)	30°
Discharge ratio	R_Q^*(-)	0.15
Tributary discharge	Q_t (L/s)	0.3
Main channel upstream discharge	Q_m (L/s)	2
Main channel downstream discharge (Total discharge)	Q_d (L/s)	2.3
Water depth	D (m)	0.10
Jet Velocity	u_j (m/s)	0.06

To expand the experimental study and conduct further investigations through numerical simulations, various scenarios were explored, as summarized in Table 11. Flow depth in all scenarios was 0.10 m, but the jet and channel discharges varied. The effects of these scenarios were thoroughly analyzed, and their implications are discussed in the subsequent sections of this paper. Further investigation focused on the impact of a low-velocity discharge (Fr = 1) in confluence regions (R5,6,9, and 10), which could not be achieved in laboratory experiments due to limitations in physical models and instrumentation. While all previous experimental runs [132] involved jet-like, momentum-dominated flows in the confluences, this study aims to examine plume-like behavior for the first time. Furthermore, four runs (R7 to R10) were conducted to investigate the effect of the confluence flow ratio on the jet trajectory, to examine how varying flow conditions at the confluence influence the mixing and dispersion patterns of the discharged jet.

Table 11. Hydraulic conditions for numerical simulations.

	Q (L/h)	u_j (m/s)	u_{a_m} (m/s)	u_{a_b} (m/s)	u_r=u_a/u_j	Jet Density (kg/m^3)	Crossflow Density (kg/m^3)	g'_0	Fr
R1(main)	2.50	0.06	0.10	0.02	1.8	997	999	0.026	5.4
R2(trib)	2.50	0.06	0.10	0.02	0.36	997	999	0.026	5.4
R3(main)	1.00	0.02	0.10	0.02	4.5	997	999	0.026	2.0
R4(trib)	1.00	0.02	0.10	0.02	0.90	997	999	0.026	2.0

R5(main)	0.50	0.01	0.10	0.02	9.0	997	999	0.026	1.1
R6(trib)	0.50	0.01	0.10	0.02	1.8	997	999	0.026	1.1
R7(main)	2.50	0.06	0.10	0.20	1.8	997	999	0.026	5.4
R8(trib)	2.50	0.06	0.10	0.20	3.6	997	999	0.026	5.4
R9(main)	0.50	0.01	0.10	0.20	9.0	997	999	0.026	1.1
R10(trib)	0.50	0.01	0.10	0.20	18	997	999	0.026	1.1

Where, R#(main) indicates the effluent jet in the main channel, R#(trib) indicates effluent jet in the tributary channel, (Q) is the jet flow rate, ambient velocity (u_a) is the general ambient velocity in the experimental setup, main channel velocity (u_{a-m}) is the velocity in the main channel, tributary channel velocity (u_{a-b}) is the velocity in the tributary channel and velocity vatio (u_r) is the ratio of ambient velocity to jet velocity, Fr is the jet densimetric Froude number.

In the present study, the numerical model Case R1 represented the experimental test scenario used for model validation. This case followed the experimental conditions specified in Table 1 with a 30° channel confluence with a discharge ratio of R_Q=0.15, where $R_Q=Q_t/Q_m$, with Q_t and Q_m representing the discharges of the upstream tributary and main channels, respectively. The jet was released from the Jet-1 location in the main channel (see Figure 4) with a velocity (u_j) of 0.06 m/s. The jet properties for case R1 are shown in Table 11.

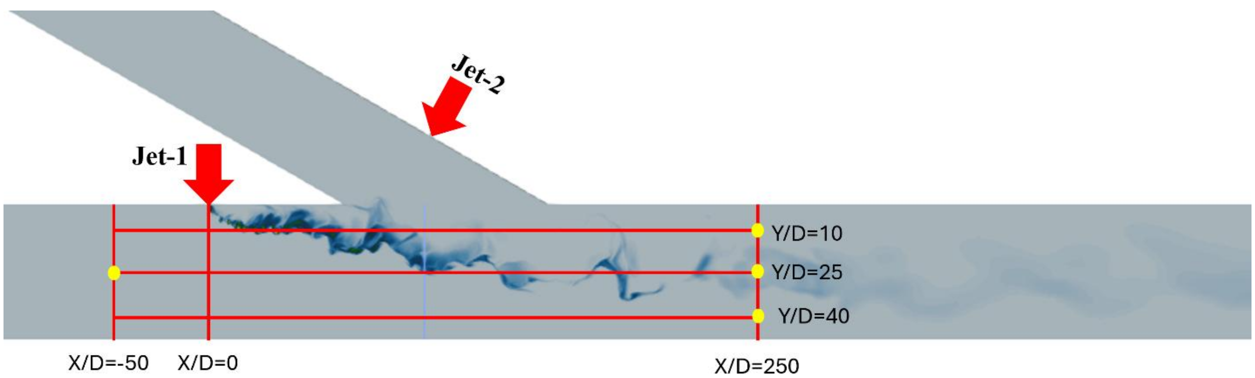

Figure 48. Measured sections, validation profiles for the simulation area and boundary conditions of the flume. Yellow circles mark the profiles that are used to compare the modeled and measured data.

5.7.2. Boundary Condition

To achieve fully developed turbulent flow, the jet inlet and channels are defined by the mapped inlet boundary condition as defined in [154]. The first inflow boundary corresponds to the jet exit, positioned at the water surface. The second and third inflow boundaries are for the main channel and tributary entrances. These profiles were established to match the experimentally determined velocity for both the jet and the crossflow. A no-slip condition was imposed at the nozzle wall, as well as at the channel walls and floor, while the water surface was treated with a slip condition.

Water discharge rates were prescribed at the inlets, and a zero-gradient condition was applied at the outlet. Additionally, a flow depth of 10 cm was maintained throughout each model run, consistent with the experimental runs.

5.7.3. Verification of Turbulent Kinetic Energy (TKE)

According to Pope (2004) [99] effective use of LES models requires that at least 80% of the TKE be resolved on the computational mesh. The resolved TKE is represented by the equation:

$$K_{res} = \frac{1}{2}(\overline{u'^2} + \overline{v'^2} + \overline{w'^2}) \quad (40)$$

where u', v', and w' denote the velocity fluctuations in the streamwise, lateral, and vertical directions, respectively, and the overbars signify time-averaging. In the simulations conducted, more than 80% of the cells in all cases meet this requirement, demonstrating that the mesh is adequately resolving the turbulent kinetic energy for the LES model (Figure 49). This indicates that the mesh quality is sufficient for accurately capturing the turbulence characteristics essential for effective LES modeling.

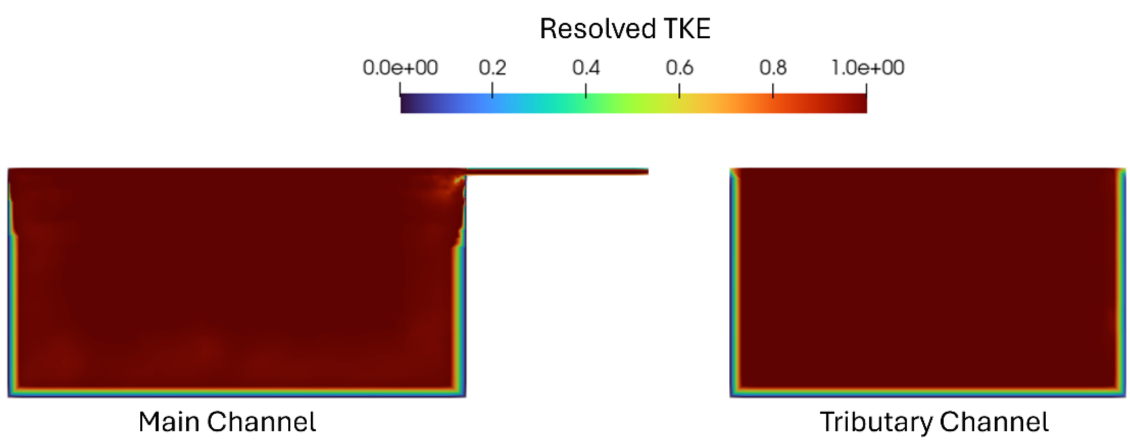

Figure 49. Proportion of TKE resolved on the mesh

5.8. Results and Discussion

5.8.1. Model Validation

Before demonstrating the capabilities of the current computational methodology, it is crucial to evaluate its accuracy in the present flow cases. In general, quantifying computational uncertainty is challenging for problems without exact solutions. However, an effective indicator of computational error is the comparison of the numerical results with available experimental data.

Figure 50A shows the velocity streamlines for Case R1, while Figure 50B presents the velocity stramlines for Case R7, demonstrating the key flow features in confluence regions. As shown, all six characteristic confluence features are evident in Figure 6B. The authors selected Case R7 due to its high confluence flow rate ratio, the largest among all the simulated cases. This particular scenario also led to the formation of a small separation zone, further emphasizing the influence of flow dynamics in confluence areas. In contrast, due to the lower velocity ratio in Figure 50A, no separation zone is observed.

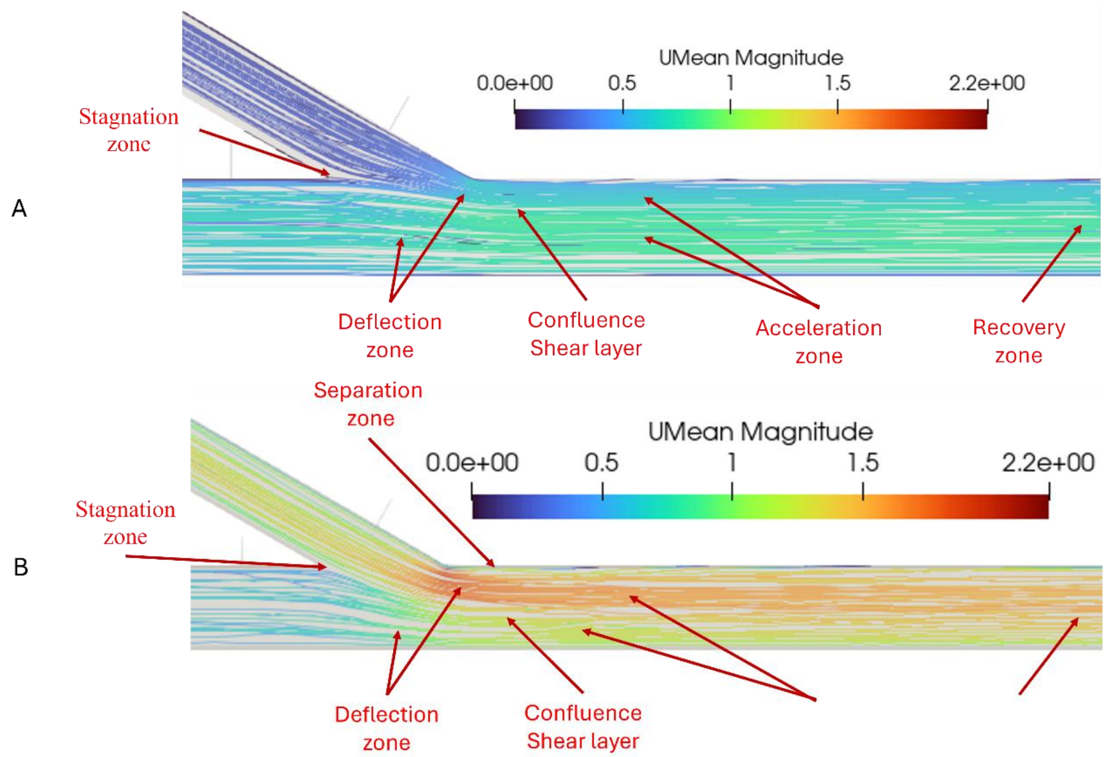

Figure 50. Streamlines of simulated time-averaged flow velocity (m/s) in confluence channel for caseR1 and R7.

Figure 51 presents for case R1 the computed and experimentally measured [132] time-averaged streamwise velocity profiles at four measurement locations within the symmetry plane: X/D = -50, Y/D = 25, and X/D = 250; Y/D = 10, 25, and 40. The velocities are normalized by the mean jet velocity. It is evident from the figure that the computed streamwise velocity profiles align well with the experimental data. The velocity distribution within the confluence is generally predictable. Overall, there is good agreement between the computed and measured velocity profiles in the confluence region.

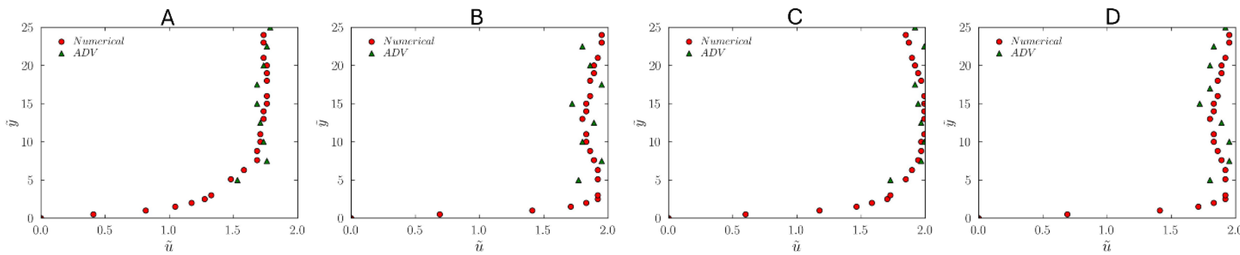

Figure 51. Measured and modeled streamwise velocities (m/s) for Case R1 at, A) X/D=-50, Y/D=25, and B) X/D=250, Y/D=10 C) X/D=250, Y/D=25 and D) X/D=250, Y/D=40 (Figure 48). The height of channel is ($\tilde{y} = \frac{Y}{D}$ and $\tilde{u} = \frac{ua}{uj}$). Experimental velocity measurements were obtained with a Nortek Vectrino Acoustic Doppler Velocimeter (ADV).

The differences between the predicted flow velocities and the experimental data appear to be minor. However, a detailed statistical analysis is necessary to quantify these discrepancies. To achieve this, the root mean square error (RMSE) was calculated to provide a more rigorous comparison between the model predictions and observed data (Table 12). Here, n represents the number of observation points, and U refers to the streamwise velocity.

$$RMSE = \sqrt{\frac{\sum(U_{experiment} - U_{Simulation})^2}{n}} \quad (23)$$

Table 12. RMSE of the simulated streamwise velocity vs. experimental data

X/D	Y/D	RMSE (%)
-50	25	2.4
250	10	5.4
250	25	3.7
250	40	5.6
Mean RMSE		4.27%

The average RMSE across the simulations was found to be 4.27%, indicating a reasonably good agreement between the model and experimental results.

The jet widening profiles at four locations along the symmetry plane of the main channel are shown in Figure 52. This figure illustrates the normalized concentration profiles across various cross-sections perpendicular to the jet's central trajectory. The experimental data were obtained using Laser Induced Fluorescence (LIF) [5]. The parameter "b_c" represents the distance from the jet centerline to the point where the concentration drops to $e^{-1}C_{max}$, with C_{max} indicating the peak tracer concentration along the centerline. Additionally, this figure shows a slightly wider profile for the numerical results, suggesting that part of the jet may not have been fully captured in the experiment.

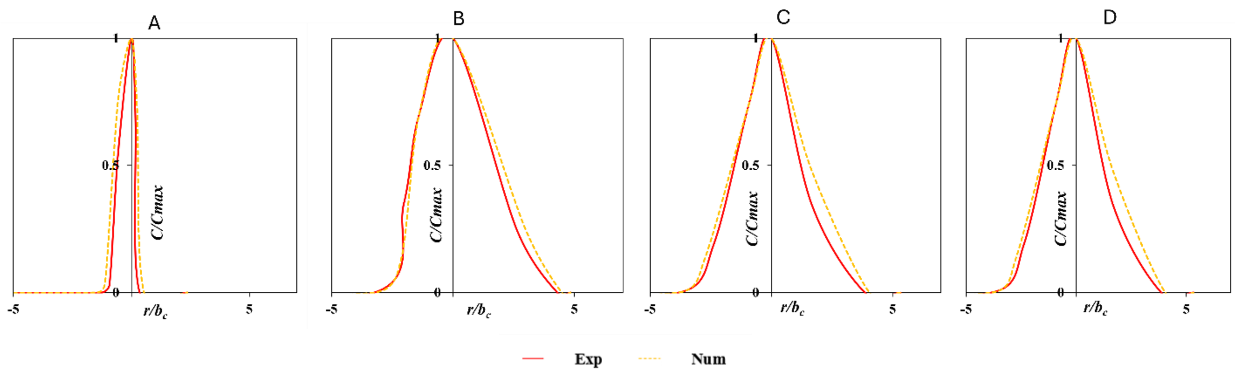

Figure 52. Experimental and numerical jet widening profiles at A) X/D=10, B) X/D=30, C) X/D=50, and D) X/D=80 for Case R1.

Another flow comparison is shown in Figure 53, where the experimental flow visualization [132] of the jet cross-section is compared with the predicted mean velocity profile at the symmetry plane for Case R1. As seen, the computed velocity profile closely matches the laboratory observations in terms of the overall size and structure of the jet.

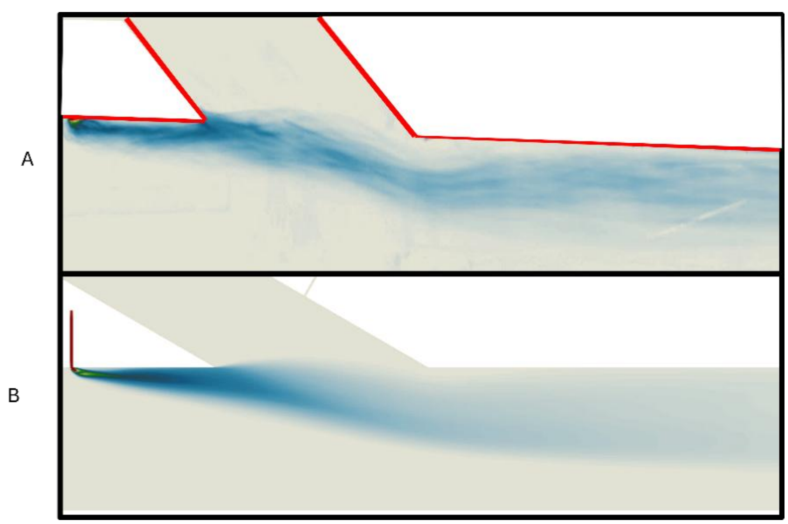

Figure 53. (A) Flow visualization from Behzad et al. [132], and (B) computed mean velocity filled contours (m/s) for Case R1.

Figure 54 presents an overlay of the numerical model's contours on the experimental results, illustrating the degree of alignment between the two. The comparison highlights how reasonable the computational predictions match the experimental observations, demonstrating the model's capability to accurately capture the key flow features.

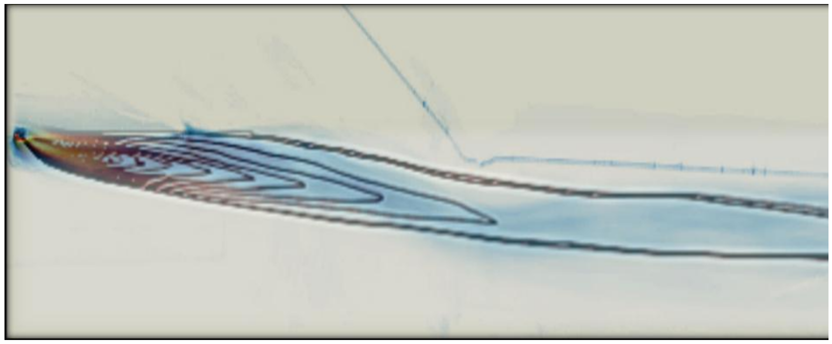

Figure 54. Overlay of numerical model contours on experimental results.

5.9.Model Results for Jet Concentration Field

5.9.1. Jet Flow Development

Figure 55 presents the contours of the mean velocity field for horizontal cross-sections at the nozzle elevation at the surface for three simulated flow cases. These velocity contours offer a clear depiction of flow development. Two of the three cases were under identical confluence hydraulic conditions, while Case C had a higher tributary flow thus a higher flow ratio. In the case of R1 (Figure 55A), a strong initial jet is observed, with the flow extending to the channel width. This diminishes as the jet velocity decreases (Case R3, Figure 55B). It is evident that the velocity ratio significantly influences jet flow development before the junction. Case R7 demonstrates how the confluence flow can alter the jet trajectory (Figure 55C). In all three cases, the jets are influenced by the confluence's shear layer near the junction, which pushes the flow further away from the inner bank.

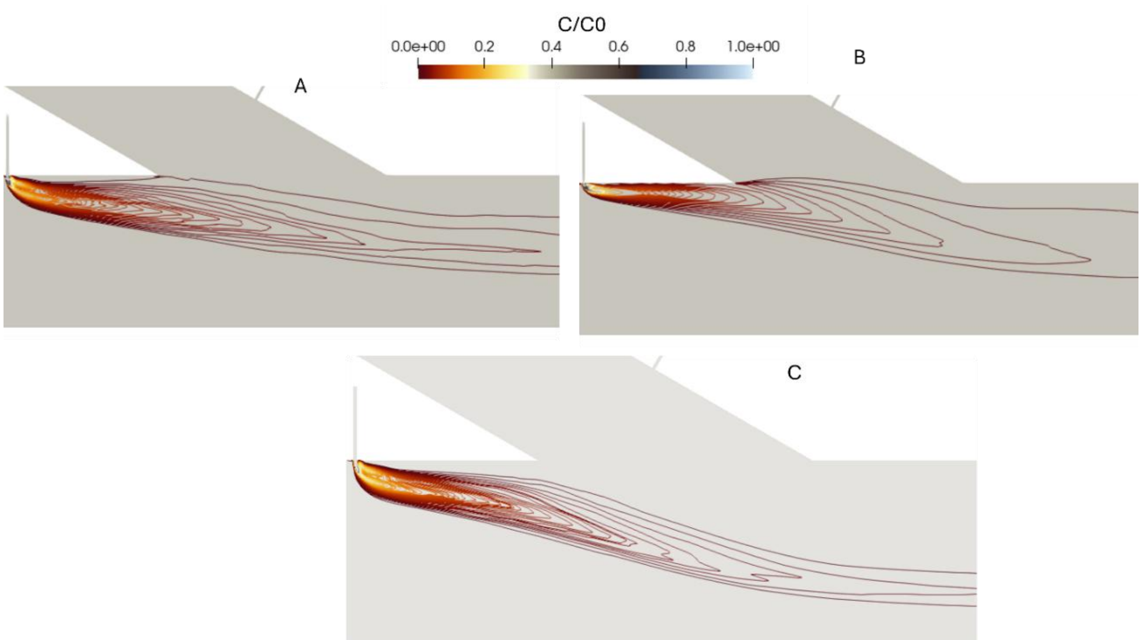

Figure 55. Flow development for (A) R1, (B) R3, and (C) R7; contour plots showing the concentration distribution at the surface.

5.9.2. Jet trajectory

The jet trajectory is defined as the path along which the concentration is highest [126]. This trajectory is determined by calculating the maximum concentration in ten cross-sectional planes perpendicular to the x-direction and then connecting these points, as shown in Figure 56 and Figure 57 for two different scenarios: jet discharge in the main channel and the tributary branch channel.

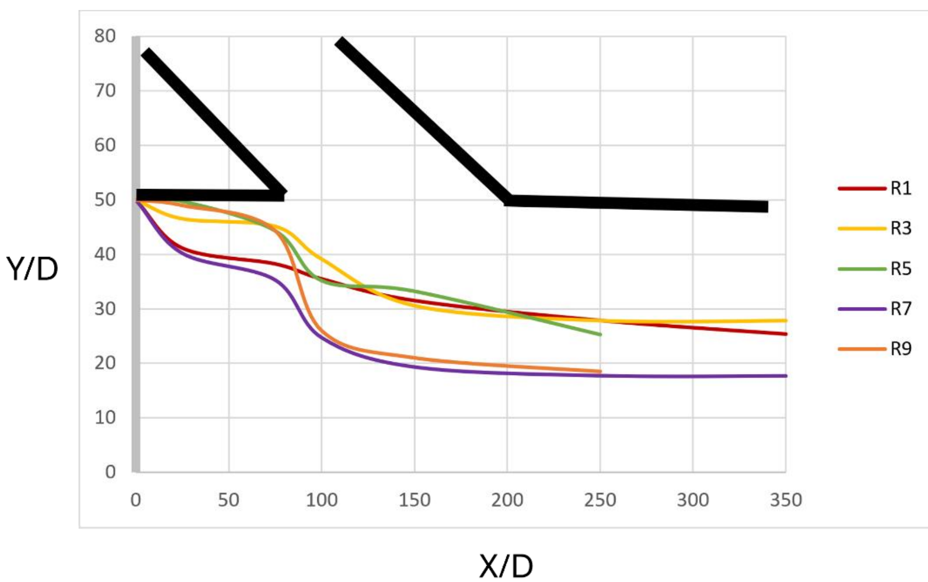

Figure 56. Jet trajectory for the cases with Jet-1.

Many researchers have demonstrated that the trajectory of a jet released in an open channel can be influenced by the velocity ratio between the jet and the crossflow [126]. When the jet velocity is low relative to the crossflow, the jet remains close to the point of release, and if the nozzle is located near the shoreline, the jet tends to follow the shoreline until it is fully diluted. As the velocity ratio increases, the jet spreads further into the channel or river width. However, as shown in Figure 56, the presence of a junction can alter this behavior. At the confluence, the jet trajectory becomes less dependent on the velocity ratio. Even for low-velocity jets (such as R5 & 9), while the initial jet behavior aligns with prior research, upon reaching the confluence, the jets are impacted by the confluence shear layer and are deflected towards the outer bank, following a nearly identical path regardless of the initial velocity. The key distinction is that lower-velocity jets dilute more quickly into the ambient water. This finding is crucial for outfall designers to predict jet behavior in various scenarios, ensuring the mitigation of pollutant impact and compliance with environmental regulations.

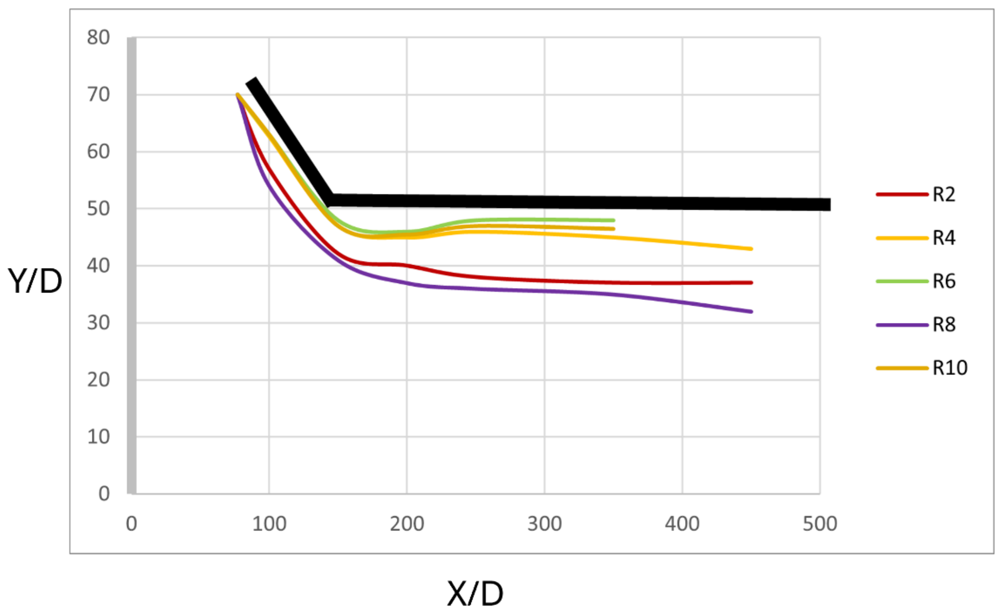

Figure 57. Jet trajectory for the cases with Jet-2.

Figure 57 demonstrates the jet trajectory when released into the tributary, highlighting that the jet moves along the inner bank, and its distribution is constrained by the confluence shear layer, limiting its spread across the channel width. Based on the results shown in Figure 56 and Figure 57, it is important for outfall designers to strategically position sensitive receptors, such as recreational areas. If these receptors are located near the inner bank, placing the jet outfall in the main channel could help restrict pollutants from reaching those areas. Conversely, if receptors are located near the outer bank, positioning the jet in the tributary may be more effective.

As shown in Figure 56 and Figure 57, the jet released in the confluence area initially behaves similarly to flow in simple channels before reaching the junction. However, upon reaching the junction, the jet's behavior becomes almost independent of its initial characteristics and is predominantly controlled by the confluence dynamics. As illustrated in these figures, jets with varying initial flow rates (whether jet-like or plume-like) follow the same trajectory after passing the junction. The primary difference is that the plume-like jet dilutes faster, reaching less than one percent of its initial concentration more quickly than the higher flow rate jets.

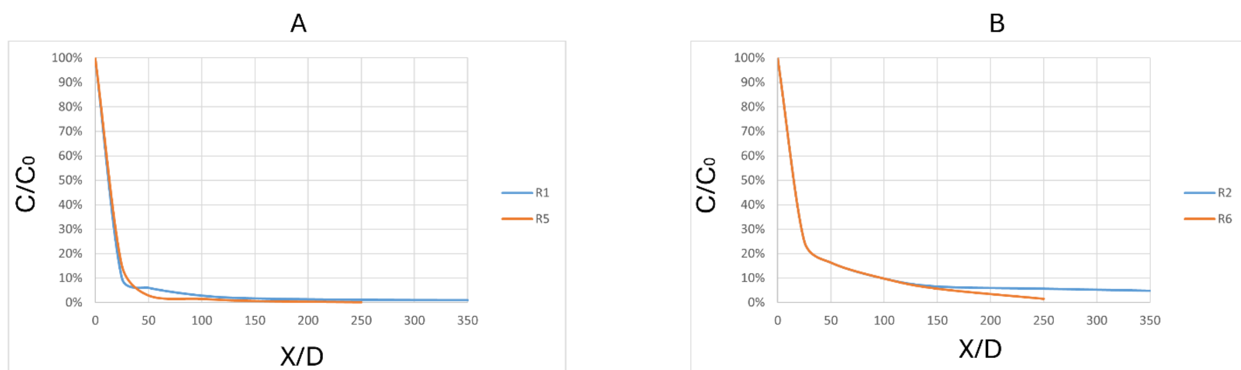

Figure 58. Concentration Distribution along X-Direction (A: R1&R5 and B: R2&R6)

In this study, dilution is defined as reaching less than 1% of the initial concentration (C_0). The concentration distribution along the X-direction, expressed as a percentage of the initial concentration (C_0), is shown in Figure 58A. In this figure, R1 and R5 are presented as representatives of high and low-velocity jets, respectively. Both jets follow a similar trajectory, but the dilution behavior differs: the high-velocity jet (R1) dilutes into the ambient water approximately 350D downstream, while the low-velocity jet (R5) achieves dilution closer to 250D. This demonstrates the influence of jet velocity on the rate and extent of mixing with the surrounding flow.

Figure 58B illustrates the concentration distribution along the X-direction for cases R2 and R6, which have the same flow rates as R1 and R5 but are released in the branch channel. The results show that the dilution of the jet in the tributary is slower compared to the main channel. This suggests that the flow conditions in the branch channel limit the mixing efficiency, causing the jet to remain concentrated for a longer distance downstream than in the main channel scenarios.

5.9.3. Cross-Section Visualization

Figure 59 presents the concentration distribution of the jet along a transverse (y–z) plane at section X/D=10 for case R7. Jets discharged into crossflows exhibit greater mixing potential compared to free jets, as noted in previous studies [155]. This enhanced mixing capability is largely attributed to the formation of counter-rotating vortex pairs (CVPs) as the jet diffuses downstream into the crossflow [52]. A key difference in jets with CVP structures is the presence of a vortex pair (one on each side of the symmetry plane) in vertical jets, as opposed to the single vortex typically observed in surface jets. It can be hypothesized that the water surface suppresses one of the vortices in a CVP, effectively creating a plane of symmetry for the flow structure [108].

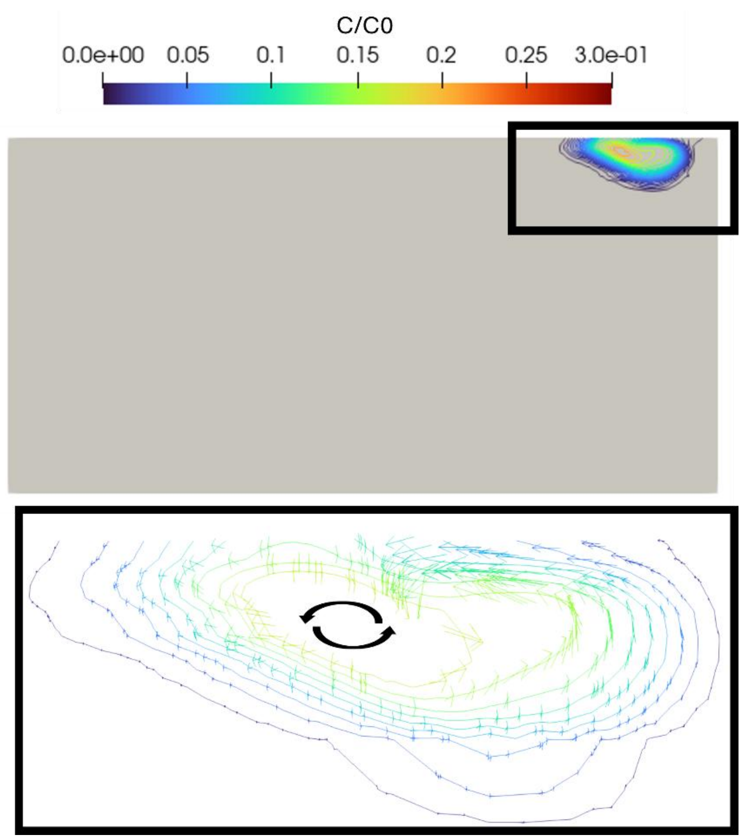

Figure 59. Concentration distribution contour across y-z plane at X/D=10 for R1 (top) and velocity vectors across y-z plane (bottom)

5.9.4. Streamlines Visualization

Figure 60 illustrates the streamline trajectories of the flow for cases R1 and R7. Both cases have the same jet flow rate, but R7 has a higher confluence flow ratio due to a larger tributary flow. The figure highlights how changes in confluence hydrodynamics affect the jet trajectory.

In case R1, with a lower confluence flow rate ratio, the jet experiences broader dispersion across the channel. As shown in the figure, the jet's width distribution is greater in this case, allowing for more extensive interaction with the surrounding crossflow. This results in a wider spread of the jet across the channel. On the other hand, in case R7, where the confluence flow rate ratio is higher, the stronger tributary flow pushes the confluence shear layer towards the outer wall, and this exerts greater control over the jet, leading to a more constrained trajectory and reduced lateral spread.

The comparison of these two cases underscores the importance of the confluence flow rate ratio in determining jet behavior. A higher ratio tends to limit the jet's dispersion and could impact the efficiency of mixing and pollutant dilution. For designers and engineers, understanding these dynamics is critical for optimizing outfall systems, especially in ensuring that effluents are adequately diluted while minimizing environmental impacts.

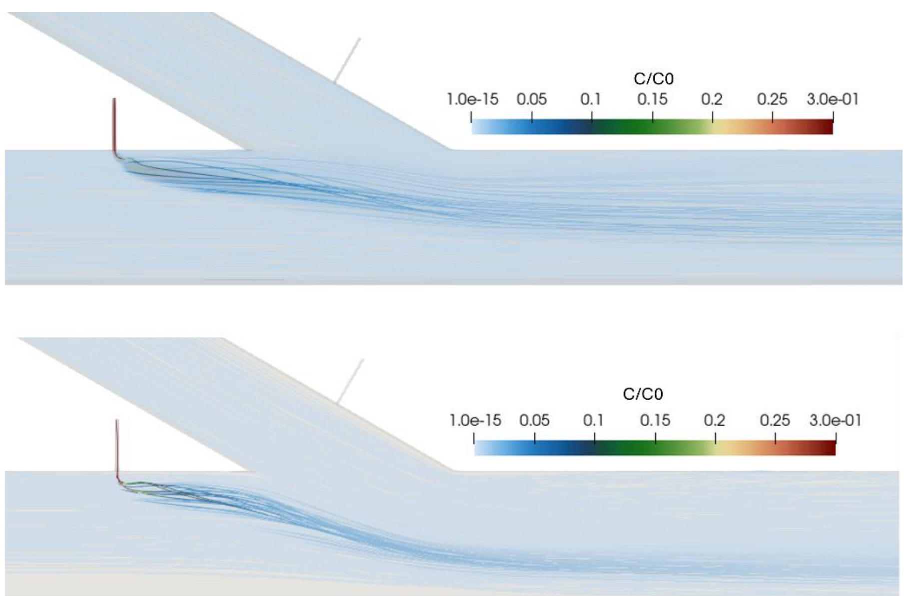

Figure 60. Streamlines Trajectories of the flow (top: R1 and below: R7)

5.9.5. Instantaneous Visualization

In Case R1, the behavior of the jet progresses through two distinct phases. Initially, the jet maintains a well-defined structure, driven by its momentum. However, as the jet approaches the confluence, it begins to disperse and interact with the surrounding flow (Figure 17). At this stage, clusters of tracer fluid start to break away from the main jet stream (highlighted within the green rectangle) as it encounters the confluence's shear layer, pushing the jet away from the inner bank. As highlighted in the green rectangle, only a small portion of the jet is able to penetrate the shear layer and move through the deflection region, entering the side of the tributary channel. This deviation significantly alters the jet's trajectory, improving its mixing efficiency with the surrounding flow.

This occurs due to the stable density gradient along the edge of the jet, where the lower-density jet fluid flows atop the denser ambient water. The resulting instability promotes enhanced mixing as the jet interacts with the denser environment.

The increased interaction of the jet with the ambient fluid facilitates dynamic exchanges between the jet's momentum and the varying velocities at the confluence. The presence of rotating tracer fluid bundles, marked by yellow rectangles, reveals active mixing and redistribution of fluid properties, resulting in a more complex and diversified flow pattern.

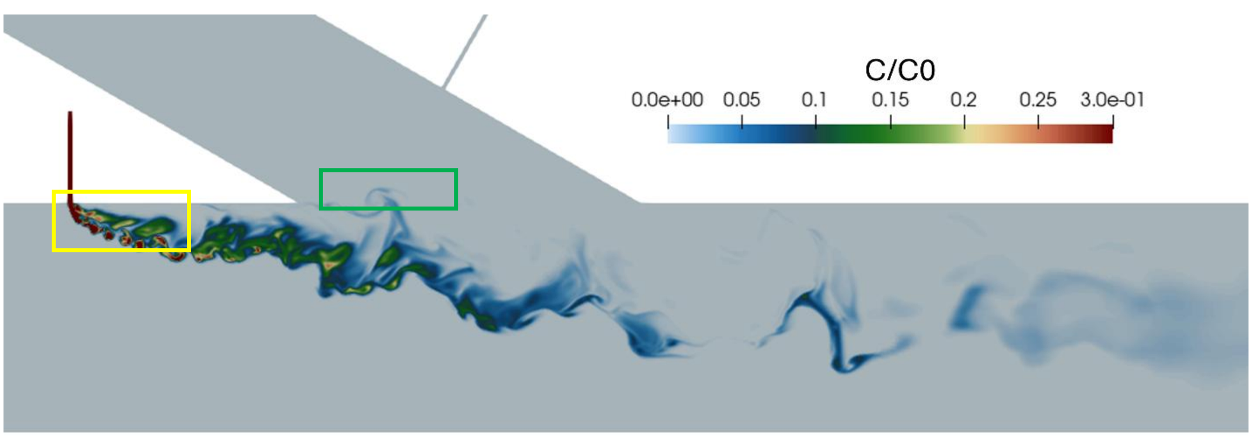

Figure 61. Instantaneous concentration flow fields for numerical case R1

In Case R2, where the jet is released into the tributary branch channel, the flow behavior is notably different from that in Case R1. Unlike the stronger dilution and dispersion observed in the main channel, the jet in Case R2 experiences reduced mixing efficiency. This is largely due to the confined nature of the branch channel and the absence of significant interaction with the main channel's confluence flow dynamics. The jet within the branch channel flow is constrained by the confluence shear layer to remain near the inner wall, thus the jet does not undergo the same level of deviation or deflection as in Case R1. Consequently, the jet maintains a more concentrated flow, resulting in a lower dilution rate. The reduced interaction with ambient water leads to less dynamic mixing, as the jet retains its momentum without significant dispersion. This results in a more localized flow pattern, with tracer fluid remaining closer to the jet trajectory and exhibiting fewer rotating tracer fluid bundles, indicating limited mixing.

Thus, in Case R2, the jet's lower dilution is primarily due to the restricted flow environment in the branch channel, which limits the jet's interaction with the ambient flow, reducing its overall mixing efficiency compared to Case R1 in the main channel.

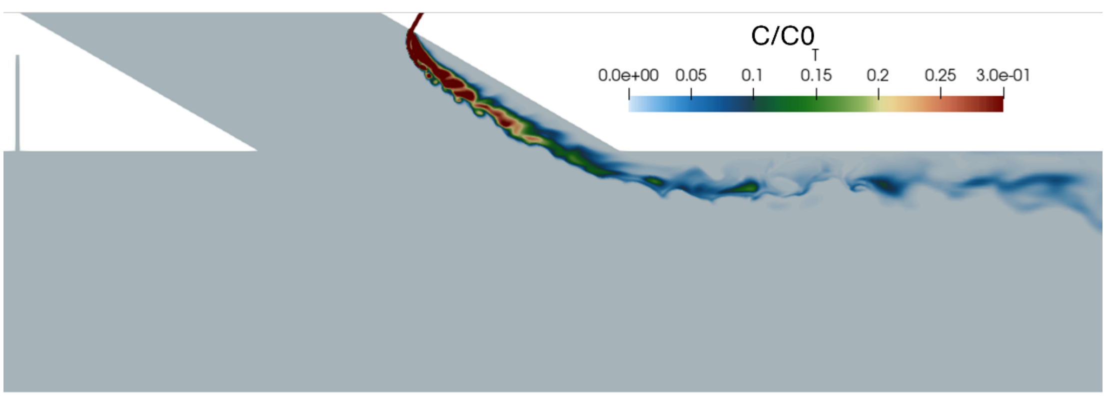

Figure 62. Instantaneous concentration flow fields for case R2

A comparison of Cases R1 and R2 highlights the significant impact of discharge locations on fluid dynamics within the confluence channels. In Case R1, the jet is effectively pushed away from the inner bank, facilitating early and efficient mixing because of the increased interaction with the surrounding fluid dynamics. This promotes the development of Kelvin-Helmholtz instabilities, which enhance mixing. In contrast, the positioning in Case R2 restricts the initial spread of the jet, resulting in a more confined flow pattern that only begins to disperse upon reaching the recovery zone.

5.9.6. Timed-averaged Visualization

Initially, the jet moves under the dominance of its momentum. As the jet progresses, it begins to bend along the width of the flume due to the influence of the crossflow current. Over time, the momentum force diminishes, eventually becoming equal to the buoyant force, at which point the jet starts to disperse. A comparison of the impact of discharge location on jet behavior can be summarized as follows:

- In Case R7, the jet's movement across the flume width was more pronounced compared to other discharge locations (R8). This is primarily attributed to the wider channel created by the confluence shear layer.
- Additionally, in Case R7, the jet exhibited the longest trajectory, allowing for extended interaction with the ambient flow, enhancing mixing and dispersion.

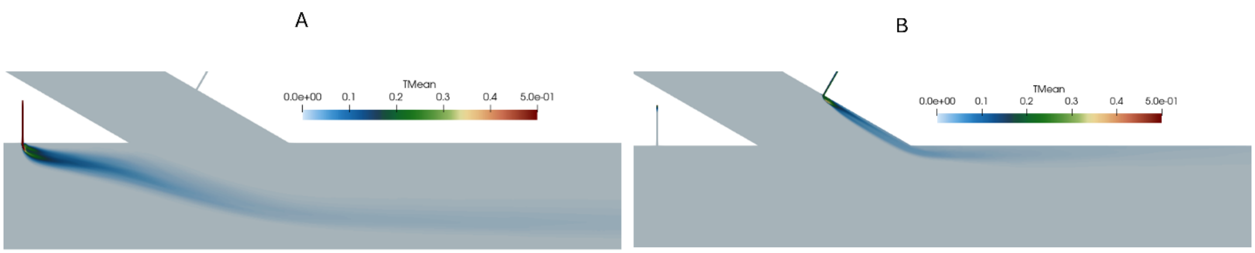

Figure 63. Time-averaged concentration filled contours (A) Jet in main channel (case R7) (B) Jet in tributary (case R8).

By comparing these two higher velocity ratio jets, a jet released in the main channel as a source of pollutants can dilute over a wider area and more rapidly under the same hydrodynamic conditions than a jet released in the tributary, thereby reducing the environmental impact.

6. Conclusion

In this numerical investigation, a comprehensive analysis of effluent discharge in confluence areas was conducted using the LES turbulent model. The study explored jet behavior under varying hydrodynamic conditions, focusing on pollutant distribution and jet trajectories within confluence regions. By extending previous experimental findings, this research provided new insights, particularly into low-velocity discharge scenarios (plume-like jets) that were unattainable in physical models due to instrument limitations. The results showed good agreement between experimental data and numerical models, with an average error of around 4%, confirming the accuracy and reliability of the simulations.

Key findings demonstrate that the confluence shear layer significantly impacts jet trajectory, influencing mixing efficiency and pollutant distribution. Jets released in the main channel exhibited longer trajectories and greater interaction with ambient flow, leading to higher dilution rates with both low and high discharge jet. Notably, low-velocity jets (plume-like) were found to be independent of jet velocity upon reaching the confluence, with their path deviating due to the shear layer when discharged in the main channel. In contrast, when released in the tributary, the jet's flow trajectory remained largely unchanged, highlighting the influence of the confluence dynamics.

This study underscores the importance of considering confluence hydrodynamics in the design of outfall systems. Numerical simulations provided critical insights into how variations in flow ratios and velocity affect jet behavior, particularly at confluence points. These findings offer valuable guidance for optimizing outfall placement and design to minimize environmental impacts and meet regulatory requirements.

7. Summary, Concluding Remarks, and Recommendations

7.1. Summary and Concluding Remarks

This study aimed to enhance the understanding of the mixing behavior of surface jets and propose location modifications to optimize their performance. A comprehensive review of the literature revealed a significant gap: the behavior of jets in confluence areas has not been investigated. To address this, the experimental component of this study focused on analyzing the concentration distributions within the mixing zone of surface jets in crossflows, specifically in confluence areas. Laser-Induced Fluorescence (LIF) was employed to measure the concentrations within the mixing zone. Additionally, numerical modeling was conducted using OpenFOAM to further explore and validate the findings.

Chapter 2:

This chapter offers an overview of the background and literature concerning surface jets, confluence flows, and related areas. It establishes the essential context needed to comprehend the research.

Chapter 3:

In this Chapter of the thesis, the complex fluid dynamics of open channel confluences were investigated, with a particular focus on the often-overlooked effects of deformed beds on flow behavior. Unlike many prior studies, which predominantly focused on flatbed configurations, this research employed an equilibrium degraded bed model in OpenFOAM to compare flow dynamics between flatbed and degraded bed conditions. Six turbulence models were utilized, including four RANS models (standard k–ε, realizable k–ε, k–ω SST, V2-f), LES, and DES, with both rigid lid and volume of fluid (VoF) methods. The LES model outperformed the others, achieving a normalized mean square error (NRMSE) of 3% under the VoF approach and 17% with the rigid lid method. The study revealed that bed morphology played an important role in shaping flow patterns, with the recirculation zone near the bed significantly reduced or absent in degraded bed scenarios, leading to changes in secondary flow structures. Additionally, vortical behavior in the confluence zone was influenced by both the bed configuration and channel geometry, as well as interactions between separated shear layers, affecting the rotation and distribution of circulation zones near the inner bank. These findings contribute to a deeper understanding of confluence flow dynamics and hold implications for hydraulic modeling and environmental management.

In chapter 4:

The flow characteristics of turbulent mixing regimes for buoyant surface jets in the confluence region were obtained using Laser-Induced Fluorescence (LIF) for the first time. The mean and turbulent flow characteristics extracted from these LIF measurements are valuable to the computational fluid dynamics (CFD) community because they can enhance the accuracy of numerical models for surface jets in crossflows, particularly in the context of jet dispersion systems. Measurements were conducted on horizontal planes relative to the surface jet axis at the discharge point. The key achievements of the experimental work in this study include the following.

- A series of experiments using the LIF technique was conducted, involving two different outfall locations in either the main channel or the tributary and two different jet velocities. The flow characteristics from these experiments were quantified using the geometric and dilution measurements obtained via LIF.
- The dilution results were assessed to characterize the influence of the confluence flow field on jet dynamics, with the goal of understanding scenarios that maximize mixing, thereby reducing environmental risks.

In chapter 5:

Numerical modeling simulations for ten cases of surface buoyant jets in crossflows in confluence regions were conducted using OpenFOAM. The concentration distribution was extracted from the numerical results and compared with the experimental results of chapter 4 (i.e., Behzad et al., 2024). Additionally, the numerical simulations were able to explore plume-like jet scenarios that could not be practically investigated in the laboratory due to physical model limitations. The following key observations were obtained from the numerical modeling of surface buoyant jets in crossflows:

- The numerical models successfully predicted the flow structures and jet trajectory within the mixing zone, closely aligning with the observations reported in the experimental study.

- The confluence shear layer significantly influences jet trajectories and mixing efficiency.
- Jets discharged in the main channel exhibit longer trajectories and greater interaction with ambient flow, leading to higher dilution rates for both low- and high-velocity jets.
- Low-velocity jets behave independently of jet velocity upon reaching the confluence, with their path altered by the shear layer.
- Jets released in the tributary maintain a more consistent trajectory, unaffected by confluence dynamics.

7.2. Limitations of the Current Study

- **Jet Location Constraints:**

Exploring alternative jet locations, such as positioning the jet along the outer bank or the opposite side of the tributary channel, was not feasible. The former was restricted due to the inability to drill holes in the tempered glass, while the latter was constrained by the limited reach of the laser sheet, which could not effectively capture the jet at that position.

- **Imaging Limitations:**

All captured images were restricted to horizontal planes. Acquiring images from vertical planes was not possible because aligning the camera parallel to the cross-sectional plane required submerging it in water. This would have necessitated the use of a waterproof camera, which was unavailable during the experiments.

- **Surface Reflection Challenges**

The laser reflections on the water surface posed significant challenges, rendering experimental measurements near the water surface impractical.

- **Jet Flow Rate Restriction**

It was not possible to reduce the jet flow rate below 1 liter per hour during the experiments. This limitation is likely attributed to the resistance within the injection tubing through which the jet was discharged.

- **Sources of Uncertainty and Errors:**

  Several factors contributed to uncertainty and potential errors in the study, including:

  - **Software Errors:** Potential inaccuracies in processing or analyzing data due to limitations in software algorithms.
  - **Background Light:** Variations in ambient lighting conditions that may have introduced noise or inconsistencies in captured images.
  - **Laser Location:** Slight misalignments in the laser sheet could have affected the accuracy of measurements.
  - **Flow Rate Fluctuations:** Variability in the jet flow rate could have influenced the consistency and repeatability of results.
  - **Error Propagation:** Small errors in initial measurements, such as flow rates or jet positioning, may have propagated during data processing, compounding their impact on the results

- **Turbulence Model Dependency (RANS):** RANS relies on turbulence models that may not accurately capture complex or transitional flows, limiting its predictive capabilities.
- **Computational Cost (LES):** LES requires fine grids and small time steps, making it computationally expensive, especially for high Reynolds number flows.
- **Near-Wall Modeling Challenges:** Both RANS (e.g., wall functions) and LES (e.g., wall-modeled LES) introduce uncertainties in flows with complex boundary layers or adverse pressure gradients.
- **Boundary and Initial Condition Sensitivity (LES):** LES results are highly sensitive to boundary and initial conditions, which can introduce nonphysical artifacts.

- **Grid Dependence and Numerical Errors:** The accuracy of both methods depends on grid resolution and numerical schemes, which can lead to errors or artificial dissipation.
- **Hybrid Approach Limitations:** In RANS-LES hybrids, transition zones between methods may introduce errors, and anisotropic turbulence is often poorly captured.

7.3. Recommendations for Future Studies

The following recommendations are proposed for future research on jets in confluence areas:

- **Expand to Negative Surface Jets**: This study focused on positive and neutral surface jets in confluence areas. Future research should consider investigating negative surface jets and compare the results with those obtained in the current study.
- **Explore Submerged Jets**: While this study examined surface jets, future studies could investigate submerged jets with different buoyancy characteristics to provide a broader understanding of jet behavior in confluence regions.
- **Vary Confluence Angles**: Due to physical limitations, this study was restricted to a 30-degree confluence angle. Future research should extend this investigation to include a range of confluence angles to understand the impact of angle variation on jet behavior.
- **PIV Experiments**: Future studies should conduct Particle Image Velocimetry (PIV) experiments to examine the flow characteristics of buoyant surface jets in confluence areas with varying junction angles. This would provide detailed velocity field data to complement the findings from LIF and numerical simulations.
- **Explore Different Numerical Models**: For the numerical section, researchers could explore different numerical modeling approaches, such as Detached Eddy Simulation (DES), to evaluate their performance in predicting the behavior of jets in confluence areas.
- **Address LIF Limitations:** Some inaccuracies in LIF results were observed outside the effluent region, possibly due to insufficient background image averaging. Future work could increase the number of background images used, for example, from 100 to 1000, to improve the accuracy and reliability of LIF measurements.

- **Effect of a Strong Tributary on Mixing:** Future research should explore the impact of a very strong tributary on the mixing and dilution dynamics of jets in confluence areas. Understanding the influence of high tributary flow rates can provide valuable data into how such conditions alter jet trajectories, mixing zones, and dilution efficiency.

References

1. Purnama, A. & Shao, D. Modeling brine discharge dispersion from two adjacent desalination outfalls in coastal waters. Desalination **362**, 68–73 (2015).
2. Alameddine, I. & El-Fadel, M. Brine discharge from desalination plants: a modeling approach to an optimized outfall design. Desalination **214**, 241–260 (2007).
3. Saeidihosseini, S. Numerical and Experimental Study of Multiport Diffusers with Non-Uniform Port Orientation. (Université d'Ottawa/University of Ottawa, 2024).
4. Lattemann, S. & Höpner, T. Environmental impact and impact assessment of seawater desalination. Desalination **220**, 1–15 (2008).
5. Poornima, E. H. et al. Impact of thermal discharge from a tropical coastal power plant on phytoplankton. J. Therm. Biol. **30**, 307–316 (2005).
6. Ocean Imaging. https://www.oceani.com/01img/Services/GeoSpatial/svcs_thermal_encinas.html.
7. Jones, G. R., Nash, J. D., Doneker, R. L. & Jirka, G. H. Buoyant surface discharges into water bodies. I: Flow classification and prediction methodology. J. Hydraul. Eng. **133**, 1010–1020 (2007).
8. Gharavi, A. Surface Discharges of Buoyant Jets in Crossflows. (Université d'Ottawa/University of Ottawa, 2022).
9. Mosley, M. P. An experimental study of channel confluences. J. Geol. **84**, 535–562 (1976).
10. Best, J. L. Sediment transport and bed morphology at river channel confluences. Sedimentology **35**, 481–498 (1988).
11. SB, W., Tamai, N. & Kawahara, Y. Bed topography, bed shear stress distribution and velocity field in a confluence. Proc. Hydraul. Eng. **34**, 307–312 (1990).
12. Leite Ribeiro, M., Schleiss, A. & Blanckaert, K. Experimental study on a widening tributary channel and its influence on the confluence morphology. River Flow 2010 961–968 (2010).
13. Liu, T., Li, C. & Fan, B. Experimental study on flow pattern and sediment transportation at a 90 open-channel confluence. Int. J. Sediment Res. **27**, 178–187 (2012).

14. Yuan, S., Tang, H., Xiao, Y., Qiu, X. & Xia, Y. Water flow and sediment transport at open-channel confluences: an experimental study. J. Hydraul. Res. **56**, 333–350 (2018).
15. Wang, X., Yan, X., Duan, H., Liu, X. & Huang, E. Experimental study on the influence of river flow confluences on the open channel stage–discharge relationship. Hydrol. Sci. J. **64**, 2025–2039 (2019).
16. Yu, Q., Yuan, S. & Rennie, C. D. Experiments on the morphodynamics of open channel confluences: Implications for the accumulation of contaminated sediments. J. Geophys. Res. Earth Surf. **125**, e2019JF005438 (2020).
17. Zhang, Z. & Lin, Y. An Experimental Study on the Influence of Drastically Varying Discharge Ratios on Bed Topography and Flow Structure at Urban Channel Confluences. Water **13**, 1147 (2021).
18. Balouchi, B., Shafai-Bejestan, M., Ruther, N. & Rahmanshahi, M. Experimental investigation of flow pattern over a fully developed bed at a 60° river confluence in large floods. Acta Geophys. **70**, 2283–2296 (2022).
19. Wang, J. et al. Experimental study on the mitigation effects of deflection walls on debris flow hazards at the confluence of tributary and main river. Bull. Eng. Geol. Environ. **81**, 354 (2022).
20. Sukhodolov, A. N. et al. Turbulent flow structure at a discordant river confluence: Asymmetric jet dynamics with implications for channel morphology. J. Geophys. Res. Earth Surf. **122**, 1278–1293 (2017).
21. Cheng, Z. & Constantinescu, G. Stratification effects on hydrodynamics and mixing at a river confluence with discordant bed. Environ. Fluid Mech. **20**, 843–872 (2020).
22. Cheng, Z. & Constantinescu, G. Stratification effects on flow hydrodynamics and mixing at a confluence with a highly discordant bed and a relatively low velocity ratio. Water Resour. Res. **54**, 4537–4562 (2018).
23. Horna-Munoz, D., Constantinescu, G., Rhoads, B., Lewis, Q. & Sukhodolov, A. Density effects at a concordant bed natural river confluence. Water Resour. Res. **56**, e2019WR026217 (2020).
24. Bradbrook, K. F., Lane, S. N. & Richards, K. S. Numerical simulation of three-dimensional, time-averaged flow structure at river channel confluences. Water Resour. Res. **36**, 2731–2746 (2000).

25. Jiang, C., Constantinescu, G., Yuan, S. & Tang, H. Flow hydrodynamics, density contrast effects and mixing at the confluence between the Yangtze River and the Poyang Lake channel. Environ. Fluid Mech. 1–29 (2022).
26. Ashmore, P. E., Ferguson, R. I., Prestegaard, K. L., Ashworth, P. J. & Paola, C. Secondary flow in anabranch confluences of a braided, gravel-bed stream. Earth Surf. Process. Landf. **17**, 299–311 (1992).
27. Biron, P., Roy, A., Best, J. L. & Boyer, C. J. Bed morphology and sedimentology at the confluence of unequal depth channels. Geomorphology **8**, 115–129 (1993).
28. Rhoads, B. L. & Kenworthy, S. T. Flow structure at an asymmetrical stream confluence. Geomorphology **11**, 273–293 (1995).
29. Rhoads, B. L. Mean structure of transport-effective flows at an asymmetrical confluence when the main stream is dominant. Coherent Flow Struct. Open Channels 491–517 (1996).
30. Rhoads, B. L. & Kenworthy, S. T. Time-averaged flow structure in the central region of a stream confluence. Earth Surf. Process. Landf. J. Br. Geomorphol. Group **23**, 171–191 (1998).
31. De Serres, B., Roy, A. G., Biron, P. M. & Best, J. L. Three-dimensional structure of flow at a confluence of river channels with discordant beds. Geomorphology **26**, 313–335 (1999).
32. Rhoads, B. L. & Sukhodolov, A. N. Field investigation of three-dimensional flow structure at stream confluences: 1. Thermal mixing and time-averaged velocities. Water Resour. Res. **37**, 2393–2410 (2001).
33. Sukhodolov, A. N. & Rhoads, B. L. Field investigation of three-dimensional flow structure at stream confluences: 2. Turbulence. Water Resour. Res. **37**, 2411–2424 (2001).
34. Rhoads, B. L. & Sukhodolov, A. N. Spatial and temporal structure of shear layer turbulence at a stream confluence. Water Resour. Res. **40**, (2004).
35. Rhoads, B. L. & Sukhodolov, A. N. Lateral momentum flux and the spatial evolution of flow within a confluence mixing interface. Water Resour. Res. **44**, (2008).

36. Rhoads, B. L., Riley, J. D. & Mayer, D. R. Response of bed morphology and bed material texture to hydrological conditions at an asymmetrical stream confluence. Geomorphology **109**, 161–173 (2009).

37. Constantinescu, G., Miyawaki, S., Rhoads, B., Sukhodolov, A. & Kirkil, G. Structure of turbulent flow at a river confluence with momentum and velocity ratios close to 1: Insight provided by an eddy-resolving numerical simulation. Water Resour. Res. **47**, (2011).

38. Yuan, S. et al. Phosphorus contamination of the surface sediment at a river confluence. J. Hydrol. **573**, 568–580 (2019).

39. Lewis, Q., Rhoads, B., Sukhodolov, A. & Constantinescu, G. Advective lateral transport of streamwise momentum governs mixing at Small River confluences. Water Resour. Res. **56**, e2019WR026817 (2020).

40. Yuan, S. et al. Hydrodynamics, sediment transport and morphological features at the confluence between the Yangtze River and the Poyang Lake. Water Resour. Res. **57**, e2020WR028284 (2021).

41. Best, J. L. Flow dynamics at river channel confluences: Implications for sediment transport and bed morphology. (1987).

42. Nouri, M., Ilkhanipour, R. & Azimi, A. H. Effects of Secondary Current on the Local Erosion Induced by Circular Turbulent Wall Jets in Cross Flow. J. Eng. Mech. **149**, 04023001 (2023).

43. Ayoub, G. M. Dispersion of buoyant jets in a flowing ambient fluid. (1971).

44. Lee, J. H. & Cheung, V. Generalized Lagrangian model for buoyant jets in current. J. Environ. Eng. **116**, 1085–1106 (1990).

45. Keffer, J. F. & Baines, W. D. The round turbulent jet in a cross-wind. J. Fluid Mech. **15**, 481–496 (1963).

46. Pratte, B. D. & Baines, W. D. Profiles of the round turbulent jet in a cross flow. J. Hydraul. Div. **93**, 53–64 (1967).

47. Meyer, K. E., Pedersen, J. M. & Ozcan, O. A turbulent jet in crossflow analysed with proper orthogonal decomposition. J. Fluid Mech. **583**, 3–1 (2007).

48. Iyer, P. S. & Mahesh, K. A numerical study of shear layer characteristics of low-speed transverse jets. J. Fluid Mech. **790**, 275–307 (2016).

49. Smith, S. H. & Mungal, M. G. Mixing, structure and scaling of the jet in crossflow. J. Fluid Mech. **357**, 83–122 (1998).

50. Williams, J. Wood; MN," Aerodynamic Interference Effects with Jet-Lift V/STOL Aircraft under Static and Forward-Speed Conditions,". (1966).

51. Gharavi, A., Mohammadian, A., Nistor, I., Peña, E. & Anta, J. Experimental study of surface buoyant jets in crossflow. Environ. Fluid Mech. **20**, 1007–1030 (2020).

52. Cortelezzi, L. & Karagozian, A. R. On the formation of the counter-rotating vortex pair in transverse jets. J. Fluid Mech. **446**, 347–373 (2001).

53. Cutler, P. R. E. On the Structure and Mixing of a Jet in Crossflow. (University of Adelaide, Department of Mechanical Engineering, 2002).

54. Fric, T. F. & Roshko, A. Vortical structure in the wake of a transverse jet. J. Fluid Mech. **279**, 1–47 (1994).

55. Kheirkhah Gildeh, H., Mohammadian, A., Nistor, I. & Qiblawey, H. Numerical Modeling of Turbulent Buoyant Wall Jets in Stationary Ambient Water. J. Hydraul. Eng. **140**, 04014012 (2014).

56. Angelidis, P. B. A numerical model for the mixing of an inclined submerged heated plane water jet in calm fluid. Int. J. Heat Mass Transf. **45**, 2567–2575 (2002).

57. Ou, R. Numerical Modeling of Horizontal Buoyant Jet Entering Shallow Water with a Crossflow. (Université d'Ottawa/University of Ottawa, 2020).

58. Dunn, W. E., Policastro, A. J. & Paddock, R. A. Surface Thermal Plumes: Evaluation of Mathematical Models for the near and Complete Field. vol. 1 (Argonne National Laboratory, 1975).

59. McGuirk, J. J. & Rodi, W. Mathematical modelling of three-dimensional heated surface jets. J. Fluid Mech. **95**, 609–633 (1979).

60. Jirka, G. H., Stolzenbach, K. D. & Adams, E. E. Buoyant surface jets. J. Hydraul. Div. **107**, 1467–1487 (1981).

61. Taherian, M. & Mohammadian, A. Buoyant jets in cross-flows: review, developments, and applications. J. Mar. Sci. Eng. **9**, 61 (2021).

62. Gungor, E. & Roberts, P. J. W. Experimental Studies on Vertical Dense Jets in a Flowing Current. J. Hydraul. Eng. **135**, 935–948 (2009).

63. Chu, V. H. & Jirka, G. H. Surface buoyant jets. Encyclopedia of fluid mechanic. (1986).

64. Behzad, E., Mohammadian, A., Rennie, C. D. & Yu, Q. Numerical Simulation of Confluence Flow in a Degraded Bed. Water 20734441 **16**, (2024).

65. Yuan, S., Xu, L., Tang, H., Xiao, Y. & Gualtieri, C. The dynamics of river confluences and their effects on the ecology of aquatic environment: A review. J. Hydrodyn. 1–14 (2022).

66. Sukhodolov, A. N. & Sukhodolova, T. A. Dynamics of flow at concordant gravel bed river confluences: Effects of junction angle and momentum flux ratio. J. Geophys. Res. Earth Surf. **124**, 588–615 (2019).

67. Bilal, A., Xie, Q. & Zhai, Y. Flow, Sediment, and Morpho-Dynamics of River Confluence in Tidal and Non-Tidal Environments. J. Mar. Sci. Eng. **8**, 591 (2020).

68. Huang, J., Weber, L. J. & Lai, Y. G. Three-dimensional numerical study of flows in open-channel junctions. J. Hydraul. Eng. **128**, 268–280 (2002).

69. Shumate, E. D. Experimental description of flow at an open-channel junction. (1998).

70. Shakibainia, A., Tabatabai, M. R. M. & Zarrati, A. R. Three-dimensional numerical study of flow structure in channel confluences. Can. J. Civ. Eng. **37**, 772–781 (2010).

71. Song, C. G., Seo, I. W. & Kim, Y. D. Analysis of secondary current effect in the modeling of shallow flow in open channels. Adv. Water Resour. **41**, 29–48 (2012).

72. Shaheed, R., Mohammadian, A. & Kheirkhah Gildeh, H. A comparison of standard k–ε and realizable k–ε turbulence models in curved and confluent channels. Environ. Fluid Mech. **19**, 543–568 (2019).

73. Tang, H., Zhang, H. & Yuan, S. Hydrodynamics and contaminant transport on a degraded bed at a 90-degree channel confluence. Environ. Fluid Mech. **18**, 443–463 (2018).

74. Penna, N. et al. Effect of the junction angle on turbulent flow at a hydraulic confluence. Water **10**, 469 (2018).

75. Schindfessel, L., Creëlle, S. & De Mulder, T. How different cross-sectional shapes influence the separation zone of an open-channel confluence. J. Hydraul. Eng. **143**, 04017036 (2017).

76. Le, T. B. et al. Large-eddy simulation of the Mississippi River under base-flow condition: hydrodynamics of a natural diffluence-confluence region. J. Hydraul. Res. **57**, 836–851 (2019).

77. Ramos, P. X., Schindfessel, L., Pêgo, J. P. & Mulder, T. D. Large-Eddy Simulations of T-shaped open-channel confluences with different downstream channel widths. (2019).

78. Yuan, S. et al. Turbulent flow structure at a 90-degree open channel confluence: Accounting for the distortion of the shear layer. J. Hydro-Environ. Res. **12**, 130–147 (2016).

79. Herrera-Granados, O. Numerical analysis of flow behavior in a rectangular channel with submerged weirs. Water **13**, 1396 (2021).

80. Duguay, J., Biron, P. & Buffin-Bélanger, T. Large-scale turbulent mixing at a mesoscale confluence assessed through drone imagery and eddy-resolved modelling. Earth Surf. Process. Landf. **47**, 345–363 (2022).

81. Stockstill, R. L. Lateral inflow in supercritical flow. (2007).

82. Ramos, P. X., Schindfessel, L., Pêgo, J. P. & De Mulder, T. Flat vs. curved rigid-lid LES computations of an open-channel confluence. J. Hydroinformatics **21**, 318–334 (2019).

83. Ramos, P. X., Schindfessel, L., Pêgo, J. P. & De Mulder, T. Influence of bed elevation discordance on flow patterns and head losses in an open-channel confluence. Water Sci. Eng. **12**, 235–243 (2019).

84. Jin, T., Cunha Ramos, P., Schindfessel, L. & De Mulder, T. Numerical study of the flow and passive scalar transport in an open-channel confluence with a flat and a degraded fixed bed. in River Flow 2020, 10th Conference on Fluvial Hydraulics 1324–1332 (CRC Press, Taylor and Francis Group, 2020).

85. Yan, X.-F. et al. Numerical assessments of bed morphological evolution in mountain river confluences under effects of hydro-morphological factors. Hydrol. Process. **36**, e14488 (2022).

86. Launder, B. E. & Spalding, D. B. The numerical computation of turbulent flows. in Numerical prediction of flow, heat transfer, turbulence and combustion 96–116 (Elsevier, 1983).

87. Bradbrook, K. F., Biron, P. M., Lane, S. N., Richards, K. S. & Roy, A. G. Investigation of controls on secondary circulation in a simple confluence geometry using a three-dimensional numerical model. Hydrol. Process. **12**, 1371–1396 (1998).

88. Shaheed, R., Yan, X. & Mohammadian, A. Review and comparison of numerical simulations of secondary flow in river confluences. Water **13**, 1917 (2021).

89. Weerakoon, S. B. Three-dimensional calculation of flow in river onfluences using boundary fitted coordinates. J Hydrosci. Hydraul. Eng. **7**, 51–62 (1989).

90. Constantinescu, G., Miyawaki, S., Rhoads, B. & Sukhodolov, A. Numerical analysis of the effect of momentum ratio on the dynamics and sediment-entrainment capacity of coherent flow structures at a stream confluence. J. Geophys. Res. Earth Surf. **117**, (2012).

91. Wilcox, D. C. Reynolds Averaging. Turbul. Model. CFD Third Ed. DCW Ind. Inc Cañada Calif. 34–38 (2006).

92. Saffman, P. G. & Wilcox, D. C. Turbulence-model predictions for turbulent boundary layers. AIAA J. **12**, 541–546 (1974).

93. Schumann, U. Subgrid scale model for finite difference simulations of turbulent flows in plane channels and annuli. J. Comput. Phys. **18**, 376–404 (1975).

94. Schindfessel, L., Creëlle, S. & De Mulder, T. Flow patterns in an open channel confluence with increasingly dominant tributary inflow. Water **7**, 4724–4751 (2015).

95. Heyrani, M., Mohammadian, A., Nistor, I. & Dursun, O. F. Numerical Modeling of Venturi Flume. Hydrology **8**, 27 (2021).

96. Li, X. & Zhao, J. Dam-break of mixtures consisting of non-Newtonian liquids and granular particles. Powder Technol. **338**, 493–505 (2018).

97. Morden, J. A., Hemida, H. & Baker, Chris. J. Comparison of RANS and Detached Eddy Simulation Results to Wind-Tunnel Data for the Surface Pressures Upon a Class 43 High-Speed Train. J. Fluids Eng. **137**, (2015).

98. Constantinescu, G., Chapelet, M. & Squires, K. Turbulence modeling applied to flow over a sphere. AIAA J. **41**, 1733–1742 (2003).

99. Pope, S. B. Ten questions concerning the large-eddy simulation of turbulent flows. New J. Phys. **6**, 35 (2004).

100. Dinh Thanh, M., Kimura, I., Shimizu, Y. & Hosoda, T. Depth-averaged 2D models with effects of secondary currents for computation of flow at a channel confluence. River Flow 2010 137–144 (2010).

101. Constantinescu, G., Miyawaki, S., Rhoads, B. & Sukhodolov, A. Numerical evaluation of the effects of planform geometry and inflow conditions on flow, turbulence structure, and bed shear velocity at a stream confluence with a concordant bed. J. Geophys. Res. Earth Surf. **119**, 2079–2097 (2014).

102. Wang, Z., Shao, D. & Westerhoff, P. Wastewater discharge impact on drinking water sources along the Yangtze River (China). Sci. Total Environ. **599**, 1399–1407 (2017).

103. Farhadian, M., Haddad, O. B., Seifollahi-Aghmiuni, S. & Loáiciga, H. A. Assimilative capacity and flow dilution for water quality protection in rivers. J. Hazard. Toxic Radioact. Waste **19**, 04014027 (2015).

104. Schreiner, H. K., Rennie, C. D. & Mohammadian, A. Trajectory of a jet in crossflow in a channel bend. Environ. Fluid Mech. **18**, 1301–1319 (2018).

105. Malcangio, D. & Mossa, M. A laboratory investigation into the influence of a rigid vegetation on the evolution of a round turbulent jet discharged within a cross flow. J. Environ. Manage. **173**, 105–120 (2016).

106. Cuthbertson, A. J. & Davies, P. A. Deposition from particle-laden, round, turbulent, horizontal, buoyant jets in stationary and coflowing receiving fluids. J. Hydraul. Eng. **134**, 390–402 (2008).

107. Stolzenbach, K. D. & Harleman, D. R. An Analytical and Experimental Investigation of Surface Discharges of Heated Water. vol. 16130 (Environmental Protection Agency, Water Quality Office, 1971).

108. Gharavi, A., Mohammadian, A., Nistor, I., Peña, E. & Anta, J. Experimental study of surface buoyant jets in crossflow. Environ. Fluid Mech. **20**, 1007–1030 (2020).

109. Anwar, H. O. Flow of surface buoyant jet in cross flow. J. Hydraul. Eng. **113**, 892–904 (1987).

110. Gawad, S. T. A., McCorquodale, J. A. & Gerges, H. Near-field mixing at an outfall. Can. J. Civ. Eng. **23**, 63–75 (1996).

111. Weerakoon, S. B. Flow structure and bed topography in river confluences. (東京大学, 1990).

112. Gualtieri, C., Ianniruberto, M. & Filizola, N. On the mixing of rivers with a difference in density: The case of the Negro/Solimões confluence, Brazil. J. Hydrol. **578**, 124029 (2019).

113. Li, K. et al. A field study of near-junction-apex flow at a large river confluence and its response to the effects of floodplain flow. J. Hydrol. **610**, 127983 (2022).

114. Moradi, G., Vermeulen, B., Rennie, C. D., Cardot, R. & Lane, S. N. Evaluation of aDcp processing options for secondary flow identification at river junctions. Earth Surf. Process. Landf. **44**, 2903–2921 (2019).

115. Gualtieri, C., Abdi, R., Ianniruberto, M., Filizola, N. & Endreny, T. A. A 3D analysis of spatial habitat metrics about the confluence of Negro and Solimões rivers, Brazil. Ecohydrology **13**, e2166 (2020).

116. Liu, X. et al. Distribution and release of perfluorinated compounds (PFCs) in water-sediment systems: the effect of confluence channels. Sci. Total Environ. **775**, 145720 (2021).

117. Martone, I., Gualtieri, C. & Endreny, T. Characterization of hyporheic exchange drivers and patterns within a low-gradient, first-order, river confluence during low and high flow. Water **12**, 649 (2020).

118. Yuan, S. et al. Fish community traits near a large confluence: Implications for its nodal effects in the river ecosystem. J. Hydrol. **626**, 130335 (2023).

119. Biron, P. M., Ramamurthy, A. S. & Han, S. Three-dimensional numerical modeling of mixing at river confluences. J. Hydraul. Eng. **130**, 243–253 (2004).

120. Constantinescu, G., Miyawaki, S., Rhoads, B. & Sukhodolov, A. Influence of planform geometry and momentum ratio on thermal mixing at a stream confluence with a concordant bed. Environ. Fluid Mech. **16**, 845–873 (2016).

121. Xiao, Y., Xia, Y., Yuan, S. & Tang, H. Distribution of phosphorus in bed sediment at confluences responding to hydrodynamics. in Proceedings of the Institution of Civil Engineers-Water Management vol. 172 149–162 (Thomas Telford Ltd, 2019).

122. Yuan, S. et al. Spatial variability of phosphorus adsorption in surface sediment at channel confluences: Field and laboratory experimental evidence. J. Hydro-Environ. Res. **18**, 25–36 (2018).

123. Parsons, D. R. et al. Large river channel confluences. River Conflu. Tribut. Fluv. Netw. 73–91 (2008).

124. Shakibainia, A., Tabatabai, M. R. M. & Zarrati, A. R. Three-dimensional numerical study of flow structure in channel confluences. Can. J. Civ. Eng. **37**, 772–781 (2010).

125. Hosseini, S. S., Taherian, M., Mohammadian, A., Ferrari, S. & Roberts, P. J. Mixing behavior of multiport diffusers with non-uniform port orientation. Desalination **567**, 116962 (2023).

126. Taherian, M., Saeidi Hosseini, S. A. R., Mohammadian, A., Ferrari, S. & Roberts, P. J. Laboratory Study on Inclined Desalination Discharges in Perpendicular Cross-Flow. Available SSRN 4638903.

127. Besalduch, L. A., Badas, M. G., Ferrari, S. & Querzoli, G. On the near field behavior of inclined negatively buoyant jets. in EPJ Web of Conferences vol. 67 02007 (EDP Sciences, 2014).

128. Eleshaky, M. E. On the Dynamics of Environmental Pollution: Simulation of the Near Field of a Jet in Crossflow. Energy Environ. **19**, 263–280 (2008).

129. Gupta, J. & Saha, A. K. Characteristics of the jet shear layer of a round elevated jet in crossflow. Exp. Therm. Fluid Sci. **158**, 111269 (2024).

130. Zhang, H. Experimental and Numerical Studies of Two-and Three-Phase Jets in Crossflow. (2024).

131. Godasiaei, S. H. & Kamali, H. Water jet angle prediction in supersonic crossflows: Euler–Lagrange and machine learning approaches. Eur. Phys. J. Plus **139**, 251 (2024).

132. Behzad, E., Rennie, C. D., Mohammadian, A. & Taherian, M. Experimental Investigation of Positively Buoyant Surface Jet in Confluence Regions. (2024).

133. Andreopoulos, J. & Rodi, W. Experimental investigation of jets in a crossflow. J. Fluid Mech. **138**, 93–127 (1984).

134. Meftah, M. B., De Serio, F., Malcangio, D., Mossa, M. & Petrillo, A. F. Experimental study of a vertical jet in a vegetated crossflow. J. Environ. Manage. **164**, 19–31 (2015).

135. Pathak, M., Dewan, A. & Dass, A. K. Computational prediction of a slightly heated turbulent rectangular jet discharged into a narrow channel crossflow using two different turbulence models. Int. J. Heat Mass Transf. **49**, 3914–3928 (2006).

136. Kumar, R. & Mukhopadhyay, S. Liquid Jet in Cross Flow Modeling Under Different Weber Numbers. in ICTEA: International Conference on Thermal Engineering vol. 1 (2024).

137. Pratte, B. D. & Baines, W. D. Profiles of the round turbulent jet in a cross flow. J. Hydraul. Div. **93**, 53–64 (1967).

138. Dunn, W. E., Policastro, A. J. & Paddock, R. A. Water Resources Research Program. Surface thermal plumes: evaluation of mathematical models for the near and complete field. (1975).

139. McGuirk, J. J. & Rodi, W. A depth-averaged mathematical model for the near field of side discharges into open-channel flow. J. Fluid Mech. **86**, 761–781 (1978).

140. Weber, L. J., Schumate, E. D. & Mawer, N. Experiments on flow at a 90 open-channel junction. J. Hydraul. Eng. **127**, 340–350 (2001).

141. Biswal, S. K., Mohapatra, P. K. & Muralidhar, K. Flow separation at an open channel confluence. ISH J. Hydraul. Eng. **16**, 89–98 (2010).

142. Yuan, S. et al. Large Wood Transport and Accumulation Near the Separation Zone of a Channel Confluence. Water Resour. Res. **60**, e2023WR034790 (2024).

143. Liu, X. et al. The effect of emergent vegetation on flow, bedload transport, and bed morphology in a diffluence-confluence unit on a meandering channel. J. Hydrol. **638**, 131488 (2024).

144. Wang, D., Cheng, X., Cao, Z. & Deng, J. Three-dimensional flow structure in a confluence-bifurcation unit. Eng. Appl. Comput. Fluid Mech. **18**, 2349076 (2024).

145. Roy, A. & Bergeron, N. Flow and particle paths at a natural river confluence with coarse bed material. Geomorphology **3**, 99–112 (1990).

146. Sharifipour, M., Bonakdari, H., Zaji, A. H. & Shamshirband, S. Numerical investigation of flow field and flowmeter accuracy in open-channel junctions. Eng. Appl. Comput. Fluid Mech. **9**, 280–290 (2015).

147. Pope, S. B. Turbulent Flows. Higher Education from Cambridge University Press https://www.cambridge.org/highereducation/books/turbulent-flows/C58EFF59AF9B81AE6CFAC9ED16486B3A doi:10.1017/CBO9780511840531.

148. Nicoud, F. & Ducros, F. [No title found]. Flow Turbul. Combust. **62**, 183–200 (1999).

149. Sagaut, P. Large-Eddy Simulations of Turbulence. By MARCEL LESIEUR, OLIVIER MÉTAIS & PIERRE COMTE. Cambridge University Press, 2005. 248 pp. ISBN 0521 78124 8.\pounds 35.00. J. Fluid Mech. **555**, 474–475 (2006).

150. Imanian, H. & Mohammadian, A. Numerical simulation of flow over ogee crested spillways under high hydraulic head ratio. Eng. Appl. Comput. Fluid Mech. **13**, 983–1000 (2019).

151. Jacobsen, N. G., Fuhrman, D. R. & Fredsøe, J. A wave generation toolbox for the open-source CFD library: OpenFoam®. Int. J. Numer. Methods Fluids **70**, 1073–1088 (2012).

152. Luo, C., Mohammadian, A., Nistor, I. & Imanian, H. Experimental and numerical study of the gated and ungated ogee spillway. Flow Meas. Instrum. **97**, 102561 (2024).

153. Pirzadeh, S. Viscous unstructured three-dimensional grids by the advancing-layers method. in 32nd Aerospace Sciences Meeting and Exhibit (American Institute of Aeronautics and Astronautics, Reno,NV,U.S.A., 1994). doi:10.2514/6.1994-417.

154. Goodarzi, D. Comment on “Amiri, NS, Abessi, O., & Roberts, PJ (2024). Venturi nozzles for desalination brine discharges. Desalination, 573, 117193.” Desalination 118105 (2024).

155. Coussement, A., Gicquel, O. & Degrez, G. Large eddy simulation of a pulsed jet in cross-flow. J. Fluid Mech. **695**, 1–34 (2012).

156. Government of Canada, P. S. and P. C. Information archivée dans le Web. https://publications.gc.ca/site/archivee-archived.html?url=https://publications.gc.ca/collections/collection_2019/eccc/En14-102-2019-eng.pdf.

157. Government of Canada, P. S. and P. C. Information archivée dans le Web. https://publications.gc.ca/site/archivee-archived.html?url=https://publications.gc.ca/collections/collection_2021/eccc/En11-19-2017-eng.pdf.

Appendix A: Thermal Water Discharge Regulations

Note: This appendix is based on the guidance document **Environmental Effects Assessment of Freshwater Thermal Discharge** from Environment and Climate Change Canada, February 2019[156].

Introduction

Thermal water discharge refers to the release of heated water from industrial or energy production facilities into natural water bodies. While such discharges are essential for facility operations, they can adversely impact aquatic ecosystems by altering water temperatures, disrupting aquatic life, and degrading water quality. To mitigate these effects, robust regulatory frameworks have been established globally and locally, emphasizing site-specific environmental assessments, mitigation strategies, and ongoing monitoring.

This appendix provides a comprehensive overview of thermal water discharge regulations, incorporating international, national, and provincial standards. It also discusses mitigation strategies, monitoring requirements, and case studies that illustrate the practical application of these regulations.

General Principles and International Guidelines

The regulation of thermal discharges is rooted in several overarching principles aimed at minimizing environmental harm. Key guidelines include:

Avoiding Adverse Effects on Aquatic Life: Maintaining temperatures within thresholds that protect species diversity and ecological balance.

Site-Specific Assessments: Tailoring limits to the unique ecological conditions of each site.

Mitigating Habitat Alterations: Preventing disruptions to thermal stratification, spawning grounds, and migratory pathways.

Internationally, the **International Joint Commission (IJC)** governs thermal discharges in the Great Lakes, stipulating that temperature changes must not impair the water's use or ecological health.

National Regulations in Canada

Under Canada's Fisheries Act (Subsection 36[3]), the deposit of deleterious substances, including thermal effluents, into water frequented by fish is prohibited unless specifically authorized. Thermal discharges are considered deleterious if they result in physical, chemical, or biological harm to aquatic habitats.

The Canadian Water Quality Guidelines (CWQG), developed by the Canadian Council of Ministers of the Environment (CCME), provide thresholds for maximum weekly average temperatures (MWAT) to protect aquatic life:

- Warm Seasons: MWAT is derived from adding a fraction of the upper lethal temperature range to the species' optimal temperature.
- Cold Seasons: MWAT ensures survival during sudden temperature declines.

Provincial Guidelines

Thermal discharge regulations vary across Canadian provinces, reflecting regional ecological and industrial conditions. For example:

Ontario: The Provincial Water Quality Objective (PWQO) limits temperature increases at mixing zones to a maximum of 10°C above natural ambient levels, with an upper limit of 30°C.

British Columbia: Specific guidelines for species like Bull Trout and Dolly Varden require maximum daily temperatures to remain below 15°C.

Alberta and Saskatchewan: Both provinces adopt CWQG criteria but impose additional conditions on mixing zone dimensions and allowable effluent volumes.

Case Studies

Several Canadian facilities illustrate the application of thermal discharge regulations:

Brighton Beach Power Station (Ontario): Its permit limits effluent temperatures to 34°C with a maximum 10°C temperature rise between intake and outfall. Benthic macroinvertebrate studies are conducted to assess environmental impacts.

Portlands Energy Centre (Ontario): Discharge is limited to 30°C, with additional monitoring of nearshore habitats and public beach areas to ensure compliance.

Bruce A Nuclear Restart Project (Ontario): This facility operates under stringent temperature rise limits (11.1°C in summer and 13°C in winter), with specialized monitoring for gas bubble disease and fish spawning.

Mitigation Strategies

Effective mitigation strategies are integral to thermal discharge management. These include:

Adoption of Alternative Cooling Systems: Utilizing closed-loop designs to minimize environmental impacts.

Discharge Redesign: Modifying outfalls to enhance mixing and dispersion.

Operational Adjustments: Scheduling thermal discharges during periods of higher water flow to dilute heat more effectively.

Monitoring and Compliance

Continuous monitoring ensures regulatory compliance and environmental protection. Key measures include:

Temperature Monitoring: Real-time sensors at intake and outfall points.

Biological Surveys: Assessing benthic communities and fish populations.

Incident Reporting: Prompt reporting of exceedances and corrective actions.

Challenges and Recommendations

Despite robust regulations, challenges persist in ensuring comprehensive compliance and addressing emerging threats such as climate change. Recommendations include:

- Enhancing predictive modeling for thermal plumes.
- Expanding collaborative research to refine species-specific temperature thresholds.
- Strengthening enforcement mechanisms and penalties for non-compliance.

Conclusion

Thermal water discharge regulations are essential for balancing industrial needs with ecological sustainability. Through rigorous guidelines, site-specific assessments, and proactive mitigation strategies, these frameworks strive to protect aquatic ecosystems from the adverse impacts of heated effluents. Continued innovation and adherence to best practices will be critical for addressing future challenges.

Appendix B: Wastewater Discharge Regulations and Ontario's Role

Note: This appendix is based on the guidance document **the Wastewater Systems Effluent Regulations (WSER),** from Environment and Climate Change Canada, 2017[157].

The Wastewater Systems Effluent Regulations (WSER), enacted under the Fisheries Act in 2012, provide a harmonized framework for managing wastewater discharges into Canada's surface waters, including rivers. These regulations establish national standards to protect aquatic ecosystems and human health while accommodating regional variations in treatment infrastructure. Ontario, as Canada's most populous province, plays a pivotal role in implementing these regulations.

Overview of the WSER

Scope of the Regulations

The WSER applies to wastewater systems that:

- Discharge into surface waters, including rivers, lakes, and oceans.
- Treat an average daily influent volume of 100 m^3 or more, typically serving populations of 250 or greater.

Certain areas, such as Nunavut, the Northwest Territories, and parts of Quebec and Newfoundland and Labrador, are exempt due to remoteness and extreme climatic conditions. Equivalency agreements with Yukon and Quebec further customize compliance standards while aligning with WSER objectives.

Effluent Discharge Standards

To minimize the environmental impact of wastewater discharges into rivers, the WSER mandates compliance with the following limits:

- Carbonaceous Biochemical Oxygen Demand (CBOD): ≤ 25 mg/L.
- Suspended Solids (SS): ≤ 25 mg/L.
- Total Residual Chlorine: ≤ 0.02 mg/L.
- Un-ionized Ammonia: ≤ 1.25 mg/L (as nitrogen, at 15°C ± 1°C).

Effluent must also pass acute lethality tests, ensuring that 100% concentrations do not harm more than 50% of aquatic test species, such as rainbow trout, within 96 hours.

Ontario's Role in Wastewater Management

Effluent Volumes and Compliance

In 2017, Ontario discharged 2.06 billion m^3 of effluent, accounting for 36% of the national total.

- 99% of this effluent met WSER standards, showcasing the province's strong infrastructure and regulatory compliance.
- Ontario reported no untreated discharges and only 14 million m^3 of undertreated effluent.

Treatment Infrastructure in Ontario

Ontario relies heavily on mechanical treatment systems, which account for 66% of its facilities. These advanced systems include:

- Activated sludge processes
- Membrane bioreactors
- Rotating biological contactors

Lagoon systems are used primarily in rural areas, while no untreated systems were reported.

Key Wastewater Systems in Ontario

Ontario hosts some of the largest wastewater treatment plants in Canada, which are critical for managing urban effluent.

Facility Name	Location	Effluent Volume (million m³)
Ashbridges Bay Treatment Plant	Toronto	241
Robert O. Pickard Environmental Centre	Ottawa	172
Humber Treatment Plant	Toronto	120
Woodward Avenue Treatment Plant	Hamilton	126

Combined Sewer Overflows (CSOs)

Ontario reported 41 systems with combined sewer overflow (CSO) points, representing 23% of all Canadian CSO systems.

- CSO events occur mainly in older urban centers like Toronto and Hamilton during heavy rainfall or snowmelt.
- Efforts are underway to modernize these systems, reducing overflow discharges into rivers.

Authorizations for Non-Compliant Discharges

The WSER provides mechanisms to accommodate systems that may temporarily exceed effluent limits:

- Transitional Authorizations (TAs): Allow systems until 2020, 2030, or 2040 to comply based on risk.
- Temporary Bypass Authorizations (TBAs): Permit bypassing of treatment during maintenance or emergencies.

- Temporary Authorization to Deposit Un-ionized Ammonia: Granted for safe discharges under specific conditions.

Environmental Impact

Ontario's efforts under the WSER have significantly reduced harmful discharges into rivers. Key impacts include:

- Improved Oxygen Levels: Lower CBOD reduces oxygen depletion in rivers, protecting aquatic life.
- Reduced Sedimentation: Lower SS levels improve water clarity and habitat quality.
- Minimized Toxicity: Acute lethality standards ensure effluent safety for fish and other organisms.

Despite these successes, Ontario continues to face challenges, including managing urban growth, addressing CSO impacts, and upgrading aging infrastructure to improve climate resilience.

Conclusion

Ontario's wastewater systems play a critical role in Canada's compliance with the WSER. The province's investment in mechanical treatment and strong regulatory adherence has set a benchmark for effective wastewater management. Continued efforts to modernize systems and mitigate combined sewer overflows will further enhance the protection of Ontario's rivers and aquatic ecosystems.

Appendix C: Verification of Fully Developed Flow Using ADV Measurements

Introduction

To ensure accurate assessments of flow dynamics within the flume, it is critical to confirm that the incoming flow remains unaffected by disturbances such as the entrance structure or gate mechanisms. Fully developed flow is characterized by a stable velocity profile and the absence of significant eddies or turbulence that could compromise measurement accuracy. This appendix describes the process of using Acoustic Doppler Velocimetry (ADV) (Figure 64) to verify flow conditions upstream and downstream of the flume entrance. A stabilizing plate was also introduced to ensure steady-state flow and eliminate unwanted eddies.

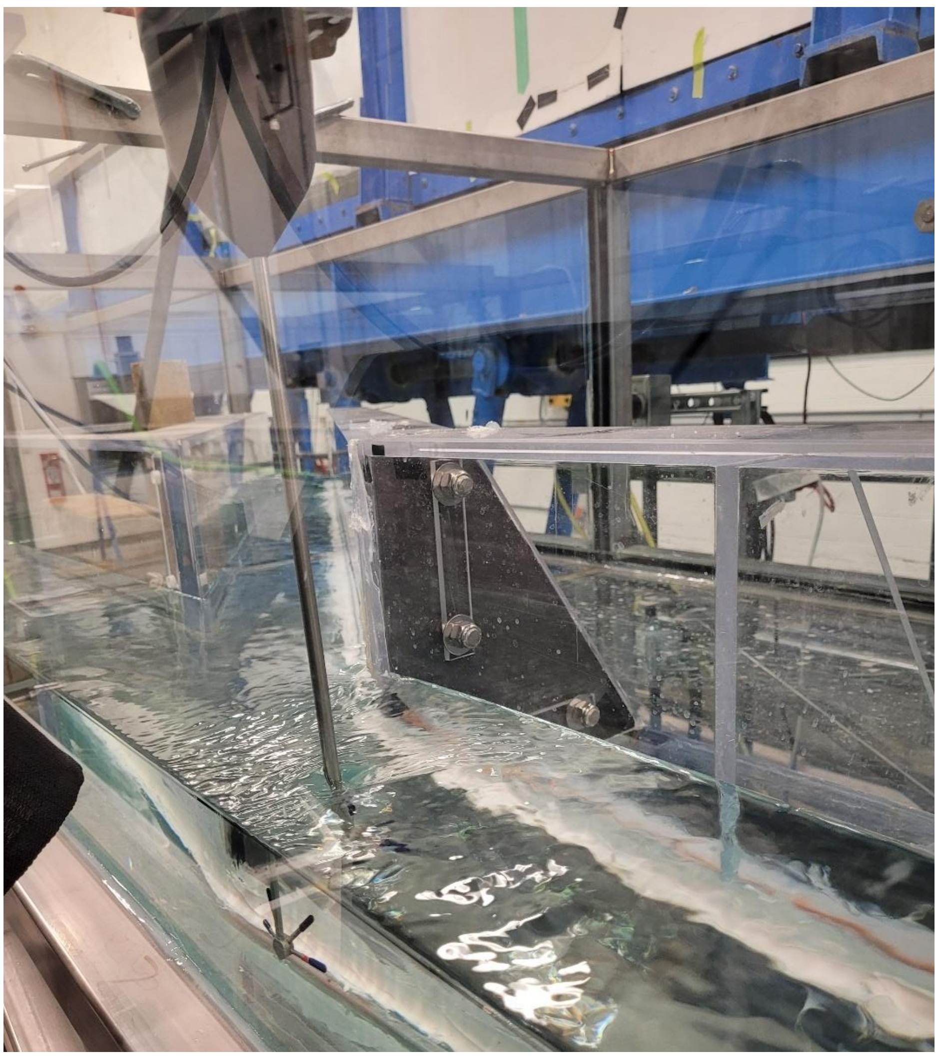

Figure 64. Acoustic Doppler Velocimetry (ADV) to verify flow conditions

Methodology

Equipment Used:

An Acoustic Doppler Velocimeter (ADV) was employed to measure three-dimensional flow velocities. This instrument provides high-resolution data by emitting high-frequency sound waves and analyzing the Doppler shift caused by the motion of water particles.

Flow Stabilization Measures:

To achieve steady-state conditions:

A stabilizing plate with several perforated points was installed at the gate (Figure 65). This design distributed flow evenly and dampened large-scale turbulence or eddies introduced by the entrance or gate operations.

The flume's geometry was adjusted to minimize flow disturbances, at the measurement locations.

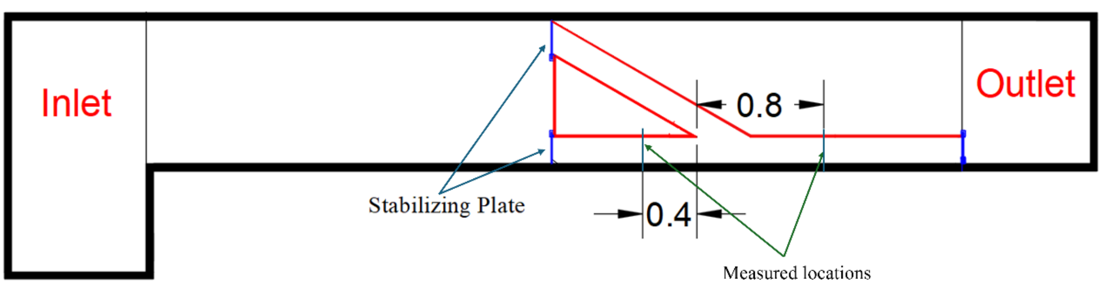

Figure 65. Schematic shape of the flume

Measurement Locations:

Upstream Points: Measurements were taken at three positions downstream of the stabilizing plates and 40cm before the junction, sufficiently far from the flume entrances to minimize entrance effects.

Downstream Points: Measurements were conducted at three points downstream of the stabilizing plate and 80cm the junction, extending beyond the flume to evaluate the restoration of fully developed flow conditions.

Measurement Procedure:

Calibration: The ADV was calibrated prior to deployment to ensure precise velocity readings.

Data Collection:

The ADV probe was submerged at predetermined depths and lateral positions at each measurement location.

Velocity components in the X, Y, and Z directions were recorded at 25 Hz for 5 minutes per point.

Post-Processing:

Raw velocity data were cleaned to remove noise and spurious signals.

Time-averaged velocity profiles were analyzed to determine flow uniformity and stability.

Results

Upstream Flow Conditions:

Flow was steady with uniform profiles across all measurement points, confirming the effectiveness of the stabilizing plate. Additionally, the LES model utilized a fully developed flow profile at the inlet boundary, and the experimental data at the upstream position A within the main channel matched the LES model results at the same location (see Figure 51). This suggests that the flow was fully developed in the experimental channel.

Downstream Flow Conditions:

Initial downstream measurements showed minor turbulence close to the stabilizing plate, as expected.

At 70 cm downstream of the plate, the velocity profiles became uniform, with negligible lateral and vertical velocity fluctuations, indicating the restoration of steady-state flow.

Discussion

The ADV measurements confirmed that the flow upstream of the stabilizing plate was unaffected by entrance effects, providing a reliable baseline for experimental evaluations. Downstream profiles demonstrated that the stabilizing plate effectively dampened unwanted eddies, promoting a fully developed flow within a short distance.

The use of a perforated stabilizing plate proved critical in ensuring consistent flow conditions, particularly for experiments requiring highly controlled environments.

Conclusion

The combined use of ADV measurements and a stabilizing plate ensured the establishment of fully developed flow conditions upstream and downstream of the flume. These measures mitigated entrance and gate effects, facilitating precise and reliable evaluations of flow dynamics for further experimentation.

Additional Remarks on Scaling:

- The flow rate was selected to ensure it maintained similarity between the experimental model and real-world conditions. The primary criteria for choosing the flow rate were based on dimensionless parameters such as the Froude number and Reynolds number, which govern the dynamics of jet mixing and buoyancy in water. By keeping these parameters within realistic ranges, the flow rate was adjusted to replicate conditions commonly observed in actual discharge scenarios. Practical limitations, such as the capacity of the experimental setup and equipment (e.g., pump and tubing), also influenced the final choice of flow rate.
- The scaling approach was guided by geometric, kinematic, and dynamic similarity principles. Geometric similarity ensured that the experimental setup accurately represented the dimensions of the real-world system. Kinematic similarity was achieved by scaling velocity and flow rate to ensure that flow patterns and mixing behaviors were comparable. Dynamic similarity, particularly Froude and Reynolds number scaling, ensured the correct balance between inertial, gravitational, and viscous forces. The chosen scaling ratio ensured that the experimental results could be extrapolated to prototype scenarios with minimized distortion due to scale effects.
- Scale effects are an inherent limitation in physical modeling. Although scaling ensures similarity, certain phenomena, such as turbulence structures and small-scale mixing, may not perfectly translate between model and prototype due to Reynolds number mismatch. In this study, the potential scale effects were mitigated by carefully choosing flow rates and monitoring key parameters. However, it is acknowledged that fine-scale details of mixing

and diffusion may vary, and numerical simulations or field studies could further refine the understanding of these effects.